A study of the abrasive waterjet micro-machining process for quartz crystals and impact erosion by high velocity micro-particles

Author:
Qi, Huan

Publication Date:
2014

DOI:
https://doi.org/10.26190/unsworks/2634

A Study of the Abrasive Waterjet Micro-machining Process for Quartz Crystals and Impact Erosion by High Velocity Micro-particles

by

Huan QI

B.E. (Mech. Eng.)

A thesis submitted to

The University of New South Wales

in fulfilment of the requirements for the degree of

Doctor of Philosophy

School of Mechanical and Manufacturing Engineering

The University of New South Wales

August 2014

THE UNIVERSITY OF NEW SOUTH WALES

Thesis/Dissertation Sheet

Surname or Family name: QI

First name: Huan

Other name/s:

Abbreviation for degree as given in the University calendar: PhD

School: Mechanical and Manufacturing Engineering

Faculty: Engineering

Title: A study of the abrasive waterjet micro-machining process for quartz crystals and impact erosion by high velocity micro-particles

Abstract

A comprehensive literature review on the development of abrasive waterjet (AWJ) machining technology and the understanding of particle impact erosion has been conducted. It has revealed that this technology possesses distinct advantages in performing micro-machining tasks over many other technologies, but further effort is required to enhance its cutting performance and understand the associated impact erosion process.

An experimental study using a pre-mixing AWJ, or abrasive slurry jet, to produce micro-channels on a quartz crystal has been undertaken to understand the machining process and performance, and the effect of process parameters. It shows that an increase in water pressure, particle concentration, abrasive particle size or jet impact angle, or a decrease in nozzle traverse speed is recommended to increase channel depth and material removal rate. By properly controlling the machining process, large wavy patterns can be minimised on the channel bottom surface. When a micro-particle impacts a quartz crystal, three types of impressions have been identified, namely craters, scratches and micro-dents, of which craters caused by brittle conchoidal fractures significantly contribute to material removal. Mathematical models for predicting the channelling performance have been developed.

A computational model for representing the impact process by a high velocity micro-particle on a quartz crystal has been developed using a discrete element method. It shows that micro-cracks on the target are initiated by high shear stresses and then median and lateral cracks are formed by both tensile and shear stresses. Material removal is mainly due to the propagation and intersection of micro-cracks which consume most of particle energy. A smaller impact angle with a lower particle velocity yields less subsurface damage to the target.

The single particle impact model has been extended to study multiple impact process incorporating a particle flow model. It shows that residual cracks can degrade the strength of substrate and facilitate material removal in subsequent impacts. A relatively large overlapping condition between successive particle impacts is more efficient in material removal in the second impact under both normal and oblique impact angles. A small jet impact angle with a fast nozzle traverse is recommended to minimise the subsurface damage.

Originality Statement

'I hereby declare that this submission is my own work and to the best of my knowledge it contains no materials previously published or written by another person, or substantial proportions of material which have been accepted for the award of any other degree or diploma at UNSW or any other educational institution, except where due acknowledgement is made in the thesis. Any contribution made to the research by others, with whom I have worked at UNSW or elsewhere, is explicitly acknowledged in the thesis. I also declare that the intellectual content of this thesis is the product of my own work, except to the extent that assistance from others in the project's design and conception or in style, presentation and linguistic expression is acknowledged.'

Signed ....Huan Qi........................

Date........31/10/2014........................

Copyright Statement

'I hereby grant the University of New South Wales or its agents the right to archive and to make available my thesis or dissertation in whole or part in the University libraries in all forms of media, now or here after known, subject to the provisions of the Copyright Act 1968. I retain all proprietary rights, such as patent rights. I also retain the right to use in future works (such as articles or books) all or part of this thesis or dissertation.

I also authorise University Microfilms to use the 350 word abstract of my thesis in Dissertation Abstract International (this is applicable to doctoral theses only).

I have either used no substantial portions of copyright material in my thesis or I have obtained permission to use copyright material; where permission has not been granted I have applied/will apply for a partial restriction of the digital copy of my thesis or dissertation.'

Signed ......Huan Qi......

Date......31/10/2014......

Authenticity Statement

'I certify that the Library deposit digital copy is a direct equivalent of the final officially approved version of my thesis. No emendation of content has occurred and if there are any minor variations in formatting, they are the result of the conversion to digital format.'

Signed ....Huan Li..

Date........31/10/2014..

Abstract

A comprehensive literature review on the development of abrasive waterjet (AWJ) machining technology and the understanding of particle impact erosion has been conducted. It has revealed that the AWJ machining technology possesses distinct advantages in performing micro-machining tasks over many other technologies, but further effort is required to enhance its cutting performance and understand the associated impact erosion process and mechanisms.

An experimental investigation into the micro-channelling process on a quartz crystal has been conducted using a pre-mixing AWJ, or abrasive slurry jet. Plausible trends of the various machining performance measures, namely the material removal rate, channel depth, channel top width, channel wall inclination angle and channel bottom surface roughness, with respect to the major process parameters has been found. It shows that an increase in water pressure, particle concentration, abrasive particle size or jet impact angle, or a decrease in nozzle traverse speed is recommended to increase the channel depth and material removal rate. By properly controlling the machining process, large wavy patterns can be minimised and are hardly discernible on the channel bottom surface. When a micro-particle impacts a quartz crystal, three types of impressions have been identified, namely craters, scratches and micro-dents, of which the craters caused by brittle conchoidal fractures significantly contribute to material removal.

Mathematical models for predicting the channelling performance have then been developed and experimentally verified.

A computational model for representing the impact process by a high velocity micro-particle on a quartz crystal has been developed using a discrete element method. This model has been verified numerically and experimentally. A simulation study using the model has shown that micro-cracks on the target are initiated by high shear stresses and then both median and lateral cracks are formed on which the effect of tensile stresses is more than that of shear stresses. Material removal is mainly due to the propagation and intersection of micro-cracks which consume most of particle energy. A smaller impact angle with a lower particle velocity yields less subsurface damage remaining on the target.

The computational model for a single particle impact has then been extended to study the multiple impact process, in which the particle flow is arranged in a layer by layer pattern. It has been shown that the residual cracks left in the preceding impact can degrade the strength of the target material and facilitate material removal in subsequent impacts. It has further been found that a relatively large overlapping condition between successive particle impacts is more efficient in material removal in the second impact for both normal and oblique impact angles, but a total overlap does not yield the maximum material removal. A small jet impact angle with a fast nozzle traverse within the range considered in this study is recommended to minimise the subsurface damage induced by particle impacts.

Keywords: Abrasive waterjet; Abrasive slurry jet; Micro-machining; Micro-channel; Quartz crystal; Discrete element; Particle impact; Impact erosion; Subsurface damage.

Acknowledgements

Foremost, I would like to express my sincerest gratitude to my supervisor, Professor Jun Wang, for his valuable advice, remarkable support and incredible patience throughout this project. My gratitude extends to my co-supervisor, Associate Professor Philip Mathew, for his constructive advice from time to time. My thanks also go to Dr Huaizhong Li and Dr Jingming Fan for their useful suggestions in this project, and they were always available and happy to offer assistance and encouragements. The completion of this project would not have been possible without their guidance. Their passion for research will be something I take with me throughout my career.

I gratefully acknowledge receiving useful suggestions from Professor Shuren Wang (Visiting Fellow in the School of Mining Engineering, the University of New South Wales) in developing computational models. My thanks also go to the laboratory staff for their assistance with my experimental work. Also, I would like to thank my colleagues, Dr King Lun Pang, Dr Viboon Tangwarodomnukun, Dr Weiyi Li, Dr Qi Wu and Mr Hao Zhu, for the valuable discussions and stimulating research environment that we shared during my study.

Special acknowledgements are extended to the China Scholarship Council (CSC) for a financial support under the CSC Full Doctoral program, and to the University of New

South Wales for a Tuition Fee Scholarship.

I would like to express my deepest appreciation to my parents and my brother, for their unconditional love and encouragement that have given me the strength to go on with my work amidst most difficult times and complete the thesis. Finally, I wish to dedicate this thesis to my grandmother, who passed away last year.

Table of contents

List of figures

List of tables

Nomenclature

a_i, b, b_i, B_i, c, c_i, C_i, $C^{'}$, d_i, k_b, k_i, k_j, K_1, $K^{'}$	constants
a	crack length (m)
A	area of the parallel bond cross-section (m^2)
b_C	jet boundary width in the initial region (m)
b_m	jet boundary width in the main region (m)
B	solid specimen width in single-edge notch bending test (m)
C_f	coefficient of friction on kerf wall
C_j	impact angle factor
C_k	characteristic velocity (m/s)
C_l	characteristic factor
C_v	orifice efficiency
C_p	abrasvie particle concentration (% by mass)
C_y	compressibility coefficient
d_g	average material grain diameter (m)
d_j	jet diameter (m)
d_{jx}	major axis of the ellipse (m)
d_{jz}	minor axis of the ellipse (m)
d_p	particle diameter (m)
D	nozzle inner diameter (m)
E_0	kinetic energy of particle before impact (J)
E_1	kinetic energy of particle after impact (J)
E_c	Young's modulus of the spherical elements (Pa)
$\bar{E}_c$	Young's modulus of the parallel bond (Pa)
E_{con}	consumed energy in impact process (J)
E_m	target material elastic modulus (Pa)
f	frequency of the laser wave (Hz)

f_n	oscillation frequency (Hz)
f_s	effective stress wave energy function
F	water squeeze film factor
$\bar{F}_i^n$	normal direction force in parallel bond (N)
$\bar{F}^n$	scalar value of $\bar{F}_i^n$ (N)
$\bar{F}_i^s$	shear direction force in parallel bond (N)
$\bar{F}^s$	scalar value of $\bar{F}_i^s$ (N)
F_l	a quasi-static load (N)
F_x	particle horizontal force (N)
F_y	particle vertical force (N)
g_i	particle impact angle factor
h	channel depth (m)
h_c	depth of cut due to cutting wear (m)
h_d	depth of cut due to deformation wear (m)
H_m	target material hardness (Pa)
I	moment of inertia of parallel bond cross-section (N·m)
J	polar moment of inertia of parallel bond cross-section (N·m)
k_n/k_s	ratio of normal to shear stiffness of the spherical elements
$\bar{k}_n/\ \bar{k}_s$	ratio of normal to shear stiffness of the parallel bond
K_{Ic}	target material fracture toughness (Pa·m$^{0.5}$)
l	distance between the two successive impacting particles in a plane parallel to the target surface (m)
L	nozzle travelling distance (m)
L_1	actual machining length (m)
L'_j	length of the jet plume in the simulation model (m)
m_a	abrasive mass flow rate (kg/s)
m_L	mass of the impacting particles during the nozzle travelling over a distance, L
m_p	average mass of a single abrasive particle (kg)
m_{pl}	mass of impacting particles in per unit length of cutting (kg/m)
m_w	water mass flow rate (kg/s)
$\bar{M}_i^n$	normal direction moments in parallel bond (N·m)
$\bar{M}^n$	scalar value of $\bar{M}_i^n$ (N·m)
$\bar{M}_i^s$	shear direction moments in parallel bond (N·m)
$\bar{M}^s$	scalar value of $\bar{M}_i^s$ (N·m)
n_p	number of particles per unit time

n_{pt}	number of impacting particles during the nozzle travelling over a distance, L
P	water pressure (Pa)
P_1	jet dynamic pressure at the nozzle exit (Pa)
P_a	air pressure (Pa)
P_d	jet dynamic pressure in the initial region (Pa)
P_m	jet centreline dynamic pressure (Pa)
r_p	particle radius (m)
R_a	channel bottom surface roughness (m)
R_f	particle roundness factor
R_{min}	minimum spherical element size in radius (m)
R_{max}	maximum spherical element size in radius (m)
R_y	ratio of particle vertical force to horizontal force
$\bar{R}$	parallel bond radius (m)
S	standoff distance (m)
S_c	channel cross-sectional area (m^2)
T_t	total time required by all the impacting particles to hit the target surface during the nozzle travelling over a distance, L, in simulation model (s)
u	nozzle traverse speed (m/s)
U_k	kinetic energy of the impacting particle (J)
v_{ap}	average particle impact velocity from nozzle exit to the target surface along the axial direction of the jet (m/s)
v_e	elastic collision critical velocity (m/s)
v_i	particle velocity considering water squeeze film effect (m/s)
v_j	jet velocity at nozzle exit (m/s)
v_m	Poisson's ratio
v_o	particle velocity at nozzle exit (m/s)
v_p	particle impact velocity (m/s)
V_s	volume of material removed by a particle (m^3)
V_{sd}	volume of material removed by a particle due to cutting wear (m^3)
V_{sc}	volume of material removed by a particle due to deformation wear (m^3)
w	jet width in the main region (m)
w_e	effective jet width in the main region (m)
w_m	minimum kerf width (m)
w_t	top channel width (m)
W	solid specimen height in single-edge notch bending test (m)

X	distance from nozzle exit (m)
X_C	length of jet initial region (m)
y_c	particle contact depth (m)
y_t	particle impingement depth (m)
Y	radial distance from the jet centreline (m)
Y_C	radial distance from the jet centreline in the initial region (m)
α_0	critical impact angle at which the tangential component of particle velocity becomes zero when the particle leaves the surface
α_l	interaction angle between the optical beams (°)
α_p	particle impact angle (°)
ε_c	cutting wear factor (Pa)
ε_p	particle impact efficiency factor
κ	momentum transfer coefficient
ρ	density of the spherical elements (kg/m^3)
ρ_f	working fluid density (kg/m^3)
ρ_p	particle density (kg/m^3)
ρ_s	slurry density (kg/m^3)
θ	channel wall inclination angle (°)
θ_A	jet expansion angle of pure air jet flow (°)
θ_n	oscillation angle (°)
θ_p	jet expansion angle of a particle flow (°)
θ_R	average resultant particle impact angle in simulation model (°)
$\bar{\sigma}_c$	shear strength of the parallel bond (Pa)
σ_{cs}	target material compressive strength (Pa)
σ_m	target material flow stress (Pa)
σ_{max}	maximum tensile stress (Pa)
$\bar{\sigma}_n$	tensile strength of the parallel bond (MPa)
λ	wavelength of the laser beam (m)
$\bar{\lambda}$	radius multiplier of the parallel bond
μ	particle friction factor in parallel bond model
φ	impact distance ratio
ψ	ratio of particle contact depth to impingement depth
τ_{max}	maximum shear stress (Pa)
γ	discharge coefficient

Chapter 1

Introduction

Micro devices are fundamental elements of high-density, high-integrity systems, such as micro-electro-mechanical system (MEMS) and micro-reactors. Micro-machining is normally required for the fabrication of the micro-features on these devices [1]. Due to the small sizes, complex details and high demands for surface quality, traditional machining techniques, such as turning, milling and drilling, are unable to meet the demands of these micro-machining tasks [2]. Current non-traditional machining techniques also exhibit limitations in micro-machining these small structures. For instance, laser machining often results in a severe heat affected zone (HAZ) around cut features, electrical discharge machining (EDM) applies for only electrically conductive materials and chemical etching is associated with a low erosion rate in addition to its environment impact. The increasing trend towards miniaturisation increases the demand for micro-machining technologies that can efficiently and accurately produce complicated micro-features on a variety of exotic materials.

As a non-traditional machining technology, the abrasive waterjet (AWJ) machining technology has been proven to be able to efficiently machine a wide range of materials, especially difficult-to-machine materials, without or with minimum thermal or mechanical damages induced by the process [3, 4]. Significant efforts have been made in the last decades to explore its applications and associated science; as a result, the process performance of this technology is relatively well understood. A reduction in scale of this technology, such as using a smaller nozzle, lower water pressure, and smaller abrasive particles seems to be an attractive avenue to be explored for meeting the pressing needs of industry in the fabrication of micro-features. It has been demonstrated in previous studies that the principle of the AWJ machining technology can be used to perform micro-machining [5-8]. Some preliminary studies have been carried out to reveal the material removal or kerf formation mechanisms involved in the relatively low pressure abrasive AWJ micro-machining process [7, 8], but further effort is required to understand the micro-machining process and the associated impact erosion in order to further develop this micro-machining technology.

In view of current understanding, the work presented in this thesis aims to provide an insight into the AWJ micro-machining process. Specifically, the objectives of this research are to:

- Conduct an experimental investigation into the abrasive slurry jet (ASJ) micro-channelling process on a quartz crystal to explore the surface quality and characteristics of the micro-channels created and analyse the effect of process parameters on the major micro-channelling performance measures, such as channel bottom surface roughness, channel depth, top channel width, channel wall inclination angle and material removal rate (MRR);
- Conduct an experimental investigation into the erosion process by the impact of high velocity individual micro-particles on a quartz crystal;

- Develop predictive models for the major micro-channelling performance measures and assess, both qualitatively and quantitatively, the plausibility and predictive abilities of the models;
- Develop a computational model for representing the impact process by a high velocity micro-particle on a brittle specimen, quartz crystal, and use the model to understand the impact erosive process and mechanisms by single micro-particle; and
- Develop a computational model for simulating the impact process by high velocity multiple micro-particles on a brittle specimen, quartz crystal, and use the model to understand the material removal process and the effect of particle impacting conditions and process parameters on material removal.

This thesis is organised into seven chapters. Following this introductory chapter, a comprehensive literature review on the development of AWJ machining technology and the understanding of particle impact erosion is presented in Chapter 2. This will highlight the necessity of the work performed in this thesis. Chapter 3 involves an experimental investigation into the micro-channelling process on a quartz crystal using an ASJ and an experimental study of the erosion process by the impact of individual micro-particles. The work presented in Chapter 4 is the development of the predictive models for the micro-channelling performance based on the theoretical understanding of the process and using the experimental data from Chapter 3. Chapter 5 details the development of a discrete element (DE) model for representing the impact process by a single micro-particle on a quartz crystal. It also entails numerical and experimental verifications of the developed model, and a computational study of the single impact event. Chapter 6 contains the work to extend the DE model developed for a single impact to multiple impacts incorporating a particle flow model, and to use the extended model to understand the multiple impact process and material removal mechanisms. Finally, in Chapter 7 the major findings and conclusions of the study are presented, and suggestions for future studies derived immediately from this work are also provided.

Chapter 2

Literature Review

2.1 Introduction

In this chapter, a comprehensive literature review on the development of AWJ machining and the current understanding of particle impact erosion will be conducted. It will first look into various micro-machining technologies, and their applications, strengths and limitations in performing micro-machining tasks. Then, the basic AWJ technology and related research will be discussed to provide an understanding of the AWJ machining process and the associated science. This is followed by a review on the development of AWJ in micro-machining applications. Analytical, experimental and numerical methods for studying particle impact erosions will be presented and discussed, where an emphasis will be made on the numerical models used for studying the impact erosion of brittle materials. Finally, the scope and motivation of the current research project will be discussed.

2.2 Micro-machining technologies

Micro-machining refers to the creation of micro-scale features on a component. The increasing demand for MEMS, micro-reactors and micro-medical components, etc.

drives a fast-growing market in micro-machining technologies [1]. In general, there are two classes of technologies which are usually employed by industry to perform micro-machining tasks, namely traditional and non-traditional machining technologies [2].

2.2.1 Traditional machining technologies

Traditional machining processes, such as turning, milling and drilling, have gone through continuous improvements in the development of machine tools and machining technologies. Material removal involved in these technologies usually refers to chips detaching from the workpiece by the interaction between a sharp and well-defined cutting tool and the work material [9]. Because of this, these technologies have the advantage of being able to cut a wide variety of materials as they are not limited by the reflectivity or electro conductivity of the target materials [10].

Traditional machining technologies can also be applied to the micro-machining process by appropriately selecting the machine tool, cutting tool and cutting conditions. However, in the case of modifying a large machine tool for micro-machining, it is important to emphasise that there is a limit to which a traditional machine tool can be scaled down. Beyond certain dimensions, the factors that can be ignored in traditional machining may play an important role in the quality of the miniaturised parts to be made. Moreover, the fabrication of micro-scale cutting tools for different types of operations is another important issue that should be addressed before traditional machining can be applied to micro-machining. On the one hand, the finest resolution of the machined feature cannot be smaller than the smallest dimension of the cutting tool itself [10], so that the ability to produce precision cutting tools is crucial to the application of these technologies. On the other hand, micro-scale cutting tools suffer from a greater incidence of tool breakage than macro-scale cutting tools, because the allowable threshold for wear and load before failure is narrowed for micro-scale cutting tools due to their small size, and consequently frequent tool breakage increases the manufacturing cost [11, 12].

Due to the increasing demand for feature size reduction, feature complexity increase, damage-free fabrication and the processing of advanced materials, traditional machining technologies are unable to meet the demand of these micro-machining tasks. Therefore, non-traditional micro-machining technologies have been developed and are increasingly used.

2.2.2 Non-traditional machining technologies

Many non-traditional machining technologies are available, which can machine advanced, but difficult-to-machine, materials in various engineering fields economically and efficiently to a high accuracy and precision. These technologies are advanced in the sense that they utilise other forms of energy rather than mechanical energy, and the common types of energy currently being employed by non-traditional machining technologies are thermal energy, electrical energy and chemical energy, as detailed below.

Laser machining is a beam-based processing technology, and its widespread use is due to its versatility, precision and efficiency [10, 13]. Laser machining operates based on directing a beam of laser on to the target, the thermal energy deposited by the laser beam onto the material surface melts or vaporizes the heated zone, which leads to material removal. Laser machining is highly versatile, as it requires no special tools for different machining operations, and can cut a variety of materials to different geometries. Since the laser beam does not come into physical contact with the workpiece, it enables greater accuracy to manipulate the beam for higher precision machining. Moreover, the ability of material removal in laser machines relies heavily on the wavelength of the laser beam generated. Recent developments in laser beam generation technology have enabled the generation of more powerful laser beams at smaller wavelengths that allow a higher machining efficiency and finer feature size at the same time [14]. However, the application of laser machining technology is usually limited by the existence of a HAZ [15]. As such, a secondary machining process is often required to remove these thermal defects, which increase the total production time and cost. In some applications, the removal of the HAZ may not be feasible as it will generate a feature size that is too large. Laser machining also has several inherent disadvantages, such as high energy consumption, high initial setup cost and an inability to cut through reflective materials, which prevent its utilisation in some specific applications [5].

Electrical discharge machining is a process by which material removal is caused by electrical energy. A pulse discharge occurs in a small gap between the workpiece and the electrode and removes the unwanted material from the target through melting and vaporising. The electrode and the workpiece must have electrical conductivity in order to generate the spark. Since EDM process does not make direct contact between the electrode and target material, it could minimise mechanical damages. Currently, EDM is also used to perform micro-machining tasks [16-20]. Due to the nature of the machining process, the limitations of EDM are that only electrically conductive materials can be machined and that the tool electrodes have to be replaced regularly due to wear, particularly in the case of processing difficult-to-machine materials [18, 19]. Furthermore, EDM is associated with low MRR and low surface quality which may involve thermal damages from the process [20].

Chemical etching is a material removal process that uses reactive etchants to remove unwanted part from the workpiece [21]. The desired part features are usually achieved by masking the area where no machining is required, so that it can produce complex components with very fine details and high surface quality without thermal defects [22]. Thus, this technology is commonly employed to perform micro-machining tasks where the cutting surface quality is important and where the material to be machined is highly susceptible to the adverse effects of laser machining or EDM. The major disadvantage of this technology is the low machining rate due to the long-time chemical reactions between the solutions and the target materials and it is not environmentally friendly.

2.2.2 Summary

In this section, commonly used traditional and non-traditional machining technologies were reviewed. It has been shown that traditional machining technologies are incapable of meeting the demand of micro-machining tasks, while each non-traditional machining technology has its own limitations. Therefore, an alternative micro-machining technology is highly desirable to meet the increasing demand from the industry.

2.3 Abrasive waterjet machining technology

AWJ machining is a process in which a high velocity of abrasive waterjet is used to remove material by means of impact erosion [4]. Due to the high velocity of impacting particles generated by the high pressure water, AWJ machining is capable of cutting virtually any material, particularly difficult-to-machine materials, such as pre-hardened steels, titanium alloys, ceramics, glasses and quartz crystals, where other machining technologies are often not technically or economically feasible [3].

The distinct advantages of AWJ cutting as compared to other machining technologies include minimum mechanical damages and heat effects in areas of the material adjacent to the cutting zone and its relatively high MRR. During the machining process a small amount of heat is generated due to the fraction between the abrasive particles and workpiece as well as the plastic deformation of the workpiece, which is instantaneously carried away from the cutting zone by the water, so HAZ is negligible. This is especially useful for the cutting of heat sensitive materials, for example, polymers [23].

Over the last few decades, considerable research and development effort has been made to develop AWJ machining technology and understand its associated science. These are considered below.

2.3.1 Abrasive waterjet machining systems

As shown in Fig. 2.1, a typical AWJ machining system consists of a high-pressure water pump system, an abrasive particles feeding system, a water jetting system, a position controlling system, which moves the nozzle along the predetermined path, and other supporting accessories. A key parameter of an AWJ machining system is the capacity of the pump pressure, as a higher pump pressure results in higher abrasive velocities and consequently higher cutting ability. In the commercial AWJ systems, this is typical at ultrahigh pressure of around 400 MPa to 600 MPa [24].

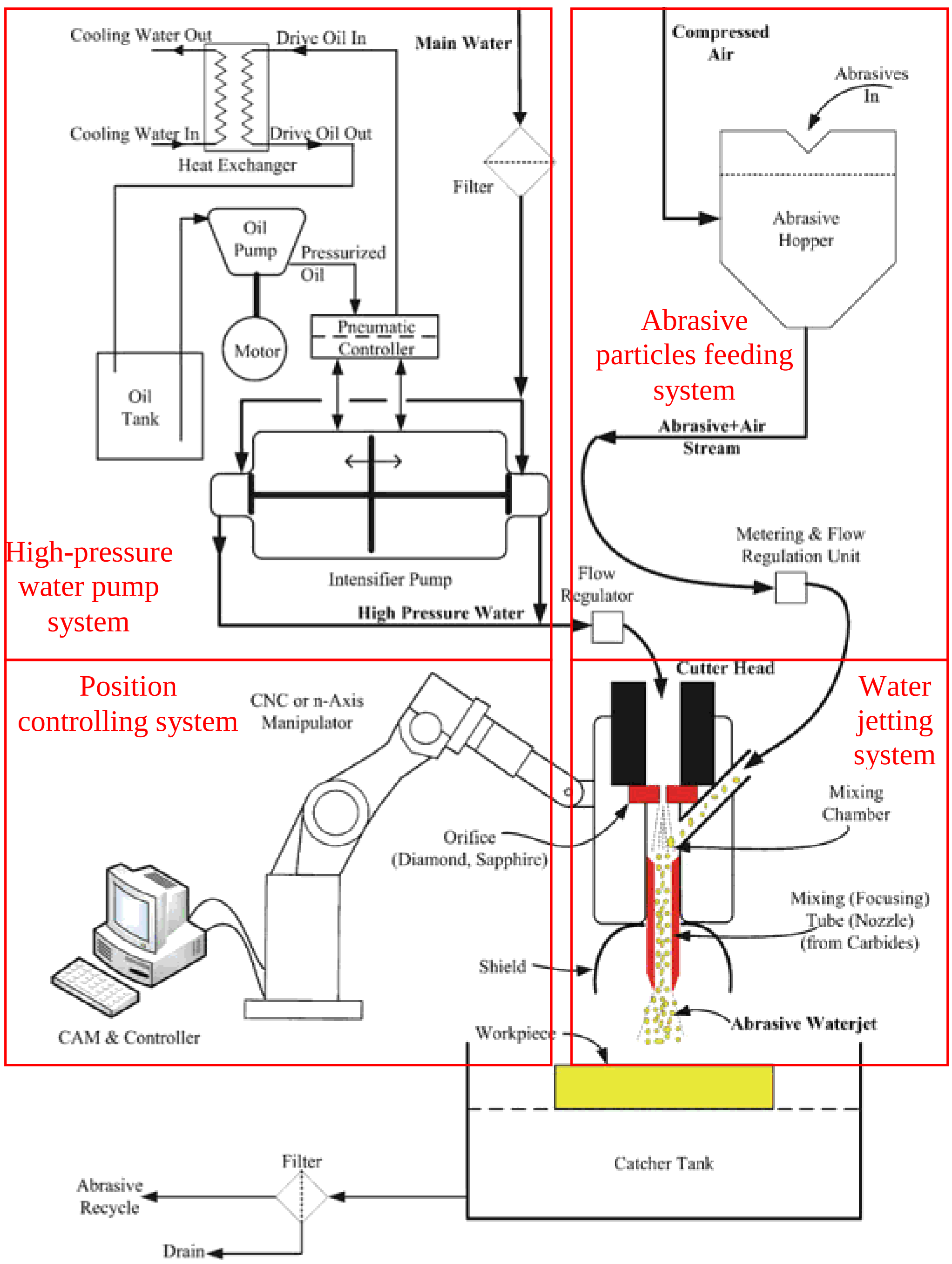

Fig. 2.1. Schematic of an AWJ machining system [25].

In the AWJ machining process, material removal is mainly caused by intensive interaction between the abrasive particles and the workpiece, while the main purpose of the carrying fluid is to accelerate the abrasive particles. Thus, according to the different ways of combining carrying fluid and abrasive particles, AWJ systems can be divided into two classes: entrainment system and abrasive slurry jet system.

In the entrainment system as shown in Fig. 2.1, the high pressurised water passes through an orifice and forms a high velocity waterjet, which is then mixed with the abrasive particles in a mixing chamber whereby the particles are entrained into the mixing chamber through a separate inlet due to the vacuum created by the high velocity waterjet. The abrasive particles are accelerated in the focusing tube by the waterjet and then exit the nozzle as an abrasive waterjet to perform cutting applications. Since the water jetting system and abrasive particles feeding system are kept separate and are only mixed at the final stage in the mixing chamber, wear on the system components, especially the orifice, is low. This design also makes maintenance and repair simpler. The limitation of the entrainment system is that it has very low efficiency in transferring the energy from the waterjet to the abrasive particles. Further, this method also has a water pressure limitation, since the entrainment process relies on the vacuum created by the high velocity waterjet, and therefore this process becomes ineffective if the water pressure falls below 100 MPa [4].

In an ASJ system as shown in Fig. 2.2, abrasive particles are premixed with a suspending liquid to form slurry. The slurry is then pumped and expelled through a nozzle to form a high velocity ASJ which can be used for cutting purposes [26]. By using appropriate additives, the abrasive particles and water can be mixed thoroughly in this system, so that it enables high efficiency in transferring energy from the water stream to the abrasive particles. Three different methods for generating an ASJ have been reported [27]. The simple direct pump method involves pressurising the premixed suspension through the water pump, and the pressurised suspension then passes through a nozzle to create an ASJ, as shown in Fig. 2.2(a). The main limitation of this method is that the abrasive particles are added prior to the water pump which causes severe wear throughout the system. To improve the operational life of the components, an isolation method was developed as shown in Fig. 2.2(b). The main part of this system is an abrasive storage vessel with an isolator inside, which is used to separate the premixed suspension from the incoming water. The high pressure water from the pump is used to move the isolator to push the premixed suspension through a nozzle to form an ASJ. In the bypass ASJ system, as illustrated in Fig. 2.2(c), the water stream, delivered by the pump, is divided into a main water stream and a so-called bypass stream. The bypass stream is used to feed the abrasive particles out of the vessel into the plain water stream in a special mixing unit. The resulting suspension is pumped through a flexible hose towards the nozzle. A restriction valve is used to control the water flow rate in the bypass line and hereby to regulate the abrasive loading ratio of the jet. In this system, the amount of abrasives could be controlled, but is not as easy as the direct pumping system due to the particle concentration change in the vessel [5].

Hashish [26] has analysed and evaluated these two types of AWJ systems, and found that the high pressure entrainment system is more effective in material removal than the low pressure ASJ system in the use of hydraulic power and abrasive consumption, while the ASJ system is more efficient than the entrainment system in terms of transferring energy from the water stream to abrasive particles. In addition, the ASJ system offers new capabilities that cannot be achieved by the entrainment system in terms of using a relatively low water pressure, a small jet diameter, a high particle concentration and a compact nozzle design, which allow the ASJ system to perform micro-machining tasks.

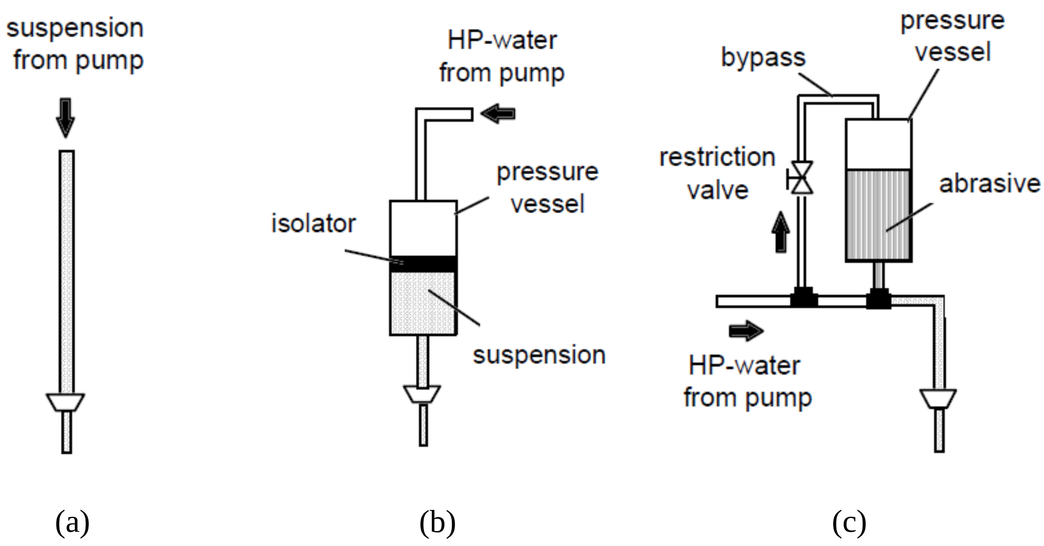

Fig. 2.2. Schematic of different ASJ system designs: (a) simple direct pumping method, (b) isolation direct pumping method, and (c) bypass method [27].

2.3.2 Jet characteristics

As the cutting ability of AWJ essentially depends on the amount of kinetic energy carried by the abrasive particles that are accelerated by the waterjet carrying them, it is necessary to understand the jet characteristics in order to understand the way in which particles impact the workpiece. Analytical, numerical and experimental methods for studying jet characteristics are presented and discussed in this section.

2.3.2.1 Analytical methods

(i) Characteristics of pure waterjets

The characteristics of a pure waterjet have been investigated by Yanagida [28] and Hashish and duPlessis [29] in depth. It has been found that a waterjet which is generated by forcing pressurised water through a nozzle is divided into three regions, i.e., the potential core region, the transitional region and the main region, as illustrated in Fig. 2.3, where the initial region is a combination of the core region and transitional region.

These regions are characterised by their dynamic pressures. In the core region the dynamic pressure is constant; in the transitional region the dynamic pressure diminishes slightly; and in the main region the dynamic pressure drops sharply. Hence, the distribution of dynamic pressure in the waterjet was typically the main topic of study.

The mathematical models for predicting the distribution of dynamic pressure in the waterjet along the axial and radial directions have been reported [29]. In the axial direction, the dynamic pressure in the initial region is expressed as

$$P_m = P_1, (X < X_C) \tag{2.1}$$

and in the main region it becomes

$$\frac{P_m}{P_1} = \frac{X_C}{X}, (X > X_C) \tag{2.2}$$

where X is the distance from the nozzle exit, P_m is the centreline dynamic pressure at X, P_1 is the dynamic pressure at the nozzle exit and X_C is the length of jet initial region, as depicted in Fig. 2.3.

In the radial direction, the dynamic pressure (P_d) in the initial region is given by

$$\frac{P_d}{P_m} = (1 - \xi_C^{1.5})^2, (\xi_C = Y - \frac{Y_C}{b_C}) \tag{2.3}$$

and in the main region it becomes

$$\frac{P_d}{P_m} = (1-\xi^{1.5})^2, (\xi = \frac{Y}{b_m}) \tag{2.4}$$

where ξ and ξ_C are non-dimensional radial positions, Y is the radial distance from the jet centreline, Y_C is the radial distance from the jet centreline in the initial region, b_C is the jet boundary width (jet radius minus the core radius) at X_C in the jet initial region, and b_m is the jet radius at X in the main region, as depicted in Fig. 2.3.

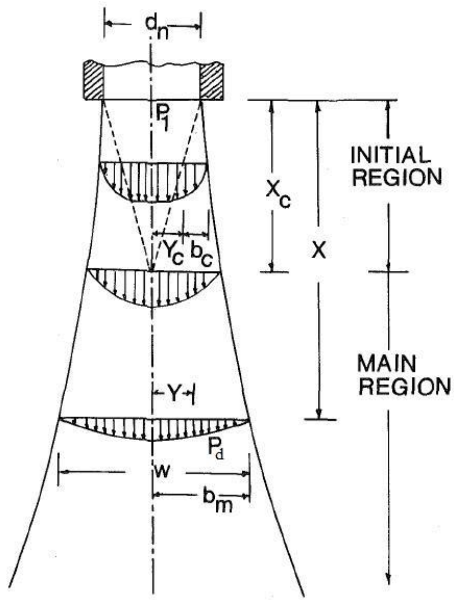

Fig. 2.3. Waterjet structure [29].

The jet width or diameter after the jet exits the nozzle (see Fig. 2.4) is another factor of concern, which could determine the kerf width in AWJ cutting [30]. It has been found that the jet spreads linearly in the initial region and is proportional to the square root of distance from nozzle, while the jet in the main region has a greater spread and its width, w, is given by

$$\frac{w}{D\sqrt{R}} = 0.335\sqrt{\frac{X}{X_C}} \tag{2.5}$$

where D is the nozzle diameter, X is the distance from the nozzle exit, X_C is the length of the jet initial region and R is the ratio of X_C to D. Typically published values of R are from 30 to 100 [28].

Further, in the main region of a jet, the effective jet diameter (w_e) (see Fig. 2.4), which is defined as the width within which the dynamic pressure satisfies the condition $\sigma_{cs}<2P_d$, can be derived from Eqs. (2.4) and (2.5), and is given by

$$\frac{w_e}{D\sqrt{R}} = 0.335\sqrt{\frac{X}{X_C}}\left[1-\sqrt{\frac{\sigma_{cs}}{2P_1}\frac{X}{X_C}}\right]^{2/3} \tag{2.6}$$

where σ_{cs} is the compressive strength of the target material.

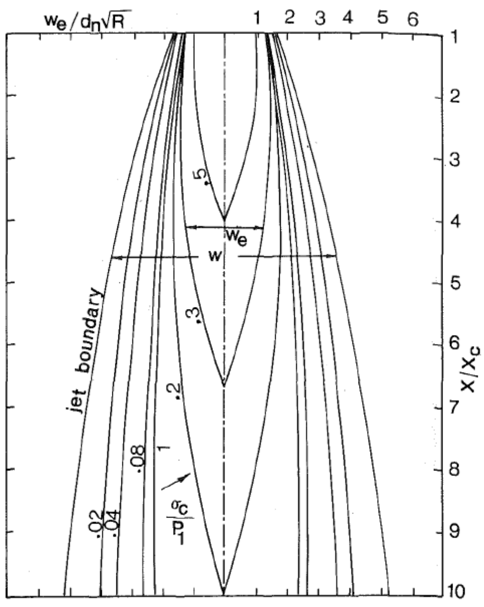

Fig. 2.4. Waterjet spreading profile [29].

(ii) Characteristics of abrasive waterjets

The understanding of the characteristics of an AWJ with added abrasive particles into a waterjet is significant for the study of the AWJ cutting process as the material removal from the workpiece mainly depends on the velocity and trajectory of the abrasive particles in the waterjet. In an AWJ, the abrasive particles are accelerated by the waterjet and so the velocity of the particles can be derived from the velocity of the waterjet. This is discussed separately for ASJ systems and entrainment systems.

In an ASJ system, the particles are premixed with the water before an ASJ is formed, and hence the velocity of the particles can be approximated to be the same as the waterjet when they exit the nozzle by neglecting slip between the water and the abrasive particles. The velocity of the abrasive particles (v_o) and the waterjet (v_j) at the nozzle exit can thus be calculated using Bernoulli's equation, i.e.

$$v_o = v_j = \gamma \sqrt{\frac{2P}{\rho_s}} \tag{2.7}$$

where P is the water pressure, ρ_s is the mixed slurry density, and γ is a coefficient of discharge that characterises the momentum loss due to wall friction, fluid flow disturbances and compressibility of water which is equal to 0.83-0.93 [4].

In an entrainment system, the particles are added after the formation of a high velocity waterjet and the acceleration is caused by the transfer of momentum from the waterjet to the particle. This process follows the law of momentum conservation, i.e.

$$v_o = \kappa \left(\frac{m_w}{m_w + m_a} \right) v_j \tag{2.8}$$

where m_w and m_a are the water mass flow rate and abrasive mass flow rate, respectively, v_j is the velocity of the waterjet at the nozzle exit which can be calculated using Eq. (2.7), and κ is the momentum-transfer coefficient obtained experimentally, which is typically in the range of 0.73 and 0.94 [4].

The models discussed above are only used to calculate the velocity of the abrasive particles at the nozzle exit and cannot be employed to determine the velocity of the particles in the jet stream which flow out of the nozzle. Some investigations have also been carried out to develop mathematical models for predicting the velocity of the particle at any location of the jet, but these models which were developed using analytical approaches are too complicated for practical applications [31, 32].

2.3.2.2 Numerical methods

Computational fluid dynamics (CFD) simulation is a numerical method for studying the characteristics of an AWJ. A practical model for predicting the particle velocity in a jet stream from the nozzle exit has been developed based on the analysis of the CFD simulation results [33-36]. It has been found that the velocity of a particle in the jet centre is characterised by decay of the axial velocity at a predictable rate, while at a given cross-section downstream from the nozzle exit, the particle velocity exhibited a top-hat profile across the diameter of the jet. With the above understanding of particle behaviours, the velocity of a particle at any given point (*X, Y)* within the jet stream can be found from

$$v_p = v_o \left(\frac{d_p}{0.1D} \right)^{C_1} \left[1.118 \left(\frac{X}{D} + 5.567 \right)^{-0.065} \right] \left[\left(1 - 2\frac{Y}{D} \right)^{B_1} + 2B_2 \left(\frac{Y}{D} \right) \right] \tag{2.9}$$

in which B_1, B_2, and C_1 are respectively given by

$$B_1 = 1 - \frac{1}{7/6 + 0.9371(X/D)^{0.4447}} \tag{2.10}$$

$$B_2 = 1 - \frac{1}{1 + 0.4906(X/D)^{0.6421}} \tag{2.11}$$

$$C_1 = \left(0.3128 - \frac{Y}{D} \right)^3 \tag{2.12}$$

where v_o is determined from Eq. (2.8), d_p is the particle diameter, D is the nozzle diameter, and B_1, B_2 and C_1 are dimensionless factors related to the location of the particle within the waterjet stream. Eq. (2.9) provides a simple and practical model to predict the velocity of the particle at any location of the jet stream from the nozzle exit, and has already been employed to determine the particle velocity in modelling the particle impact process relevant to AWJ cutting [37, 38].

2.3.2.3 Experimental approaches

Since an AWJ is relatively small in size, moves fast and contains a large number of small abrasive particles, it is hard to measure jet characteristics using traditional techniques. Some non-invasive techniques, such as a laser-based method, have been successfully applied to the measurement of the particle velocity and particle distribution in an AWJ, as discussed below.

Chen and Geskin [39] used a laser transit anemometer (LTA) to measure the particle velocity in an AWJ. The LTA has a lens system to split a single incoming laser beam into two beams of equal intensity, and focuses the beams in a small region at two closely-spaced focal points. A particle passing through the focal point of either of these split beams generates a scattering light that is detected and converted into a voltage signal. Particle velocity is calculated by dividing a known distance between the focal point by the time difference between the two successive signals detected by the photomultiplier. In this experiment, the particle velocity measured by LTA achieved 85% of the theoretical velocity calculated by Bernoulli's equation.

Another laser-based technique, which is often referred to as laser doppler velocimetry (LDV), has already been used in measuring the particle velocity in an AWJ [40, 41]. In this system (see Fig. 2.5), a polarised laser beam is split into two parallel beams by a partial mirror. These two beams pass through a converging lens, and then intersect at the focal point of the lens that is in the AWJ. The interference between these two beams allows the calculation of the average abrasive particle velocity, which is given by

$$v_p = \frac{f\lambda}{2\sin(\alpha_l/2)} \tag{2.13}$$

where λ is the wavelength of the laser beam, α_l is the interaction angle between the optical beams (see Fig. 2.5), and f is the frequency of the laser wave.

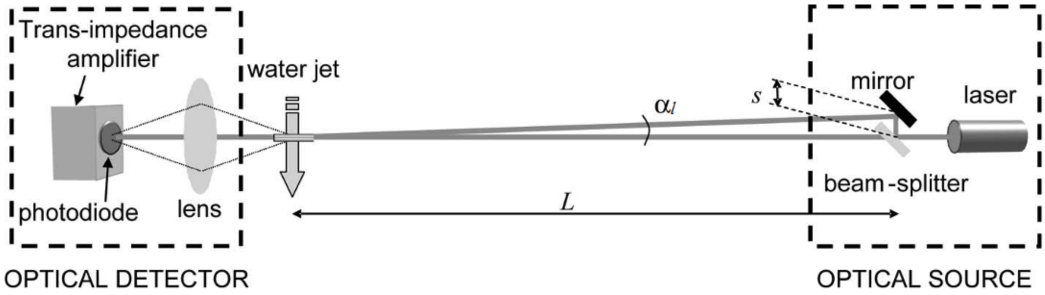

Fig. 2.5. Schematic representation of an LDV measurement system [40].

Particle image velocimetry (PIV) is another non-intrusive optical technique for a fast acquisition of a flow field. In a PIV system, a laser generates a thin light sheet inside the flow, and images of fine particles lying in the light sheet are recorded on a digital camera. The displacement of the particle images is measured in the plane of the image and used to determine the displacement of the particles in the flow. Velocity is just the displacement divided by the time between the laser pulses [42]. This method has been successfully employed by Li et al. [43] and Fan et al. [44] to measure the velocity of micro-particles within a micro-abrasive jet, where the experimental setup is shown in Fig. 2.6. The main difference between PIV and LDV is that PIV produces two dimensional vector fields, while LDV can only measure the velocity at a point.

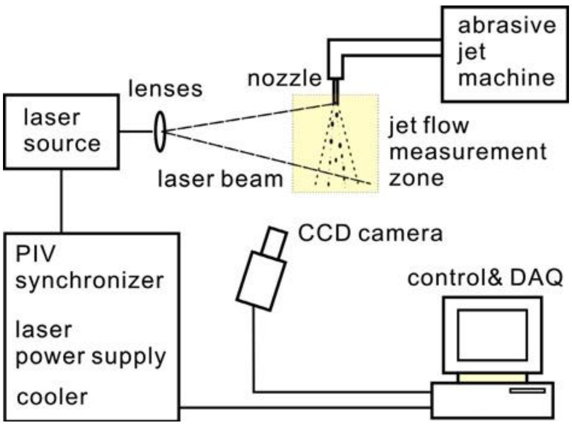

Fig. 2.6. Schematic diagram of a generalised PIV setup for measuring the particle velocities in a micro-abrasive jet [44].

In summary, LTA, LDV and PIV are considered as advanced, efficient and accurate techniques in experimentally measuring the characteristics of an AWJ. Nevertheless, numerical approaches appear to be more versatile to obtain jet characteristics that experimental methods cannot or have difficulty in achieving.

2.3.3 Kerf formation process and characteristics

In AWJ cutting, the combined effect of impacting particles results in target material removal to form a kerf on the target. It is therefore important to understand the kerf formation process and kerf characteristics in order to assess the AWJ cutting ability and effectively optimise the cutting performance. In this section, previous studies on the kerf formation process in the jet penetration direction and in the nozzle traverse direction are discussed, followed by a review of the kerf characteristics.

2.3.3.1 Kerf formation process

(i) Kerf formation process in jet penetration direction

Hashish [45, 46] reported his findings in kerf formation process in the jet penetration direction. He carried out a visualisation study on the AWJ cutting process to capture the cutting path from a film of the cutting process by tracing the interface between the jet and the target material frame by frame. It has been found that the cutting process consists of two zones, namely the cutting wear zone and deformation wear zone, as shown in Fig. 2.7. In the cutting wear zone, material removal is primarily caused by the micro-cutting due to shallow angles of attack [47]. This is a steady process where the material removal rate is the same as the material-displacement rate. In the deformation wear zone, the material removal is dominated by deformation wear due to large angles of attack [48], which is an unsteady penetration process. The penetration energy of the

AWJ decreases with increasing impact angle down to the deformation wear zone, and eventually creates a step in the target material, as shown in Fig. 2.7.

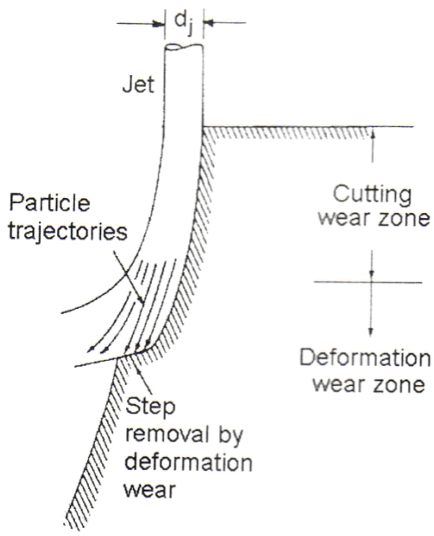

Fig. 2.7. Schematic representation of cutting wear zone and deformation wear zone [45].

By analysing the kerf profile in AWJ cutting of polycrystalline ceramics, Zeng and Kim [49] proposed a direct-secondary impact zone model to describe the kerf formation process as illustrated in Fig. 2.8. Unlike Hashish's model [45], they believed that the whole cutting process was related to the impact by particles at glancing angles, regardless of the type of target material. The first stage is called direct impact zone, in which the abrasive particles continuously and directly impact the cutting front at shallow angles. As the jet moves forward into the material, the area below the direct impact zone and behind the abrasive jet is exposed to secondary and tertiary impacts from abrasive particles that deflect from the direct impact zone, resulting in the formation of steps. In the secondary zone, the cutting process is unstable and there is a sudden change in curvature at the cutting front since the deflected particles travel in a non-uniform direction and carry a different amount of energy.

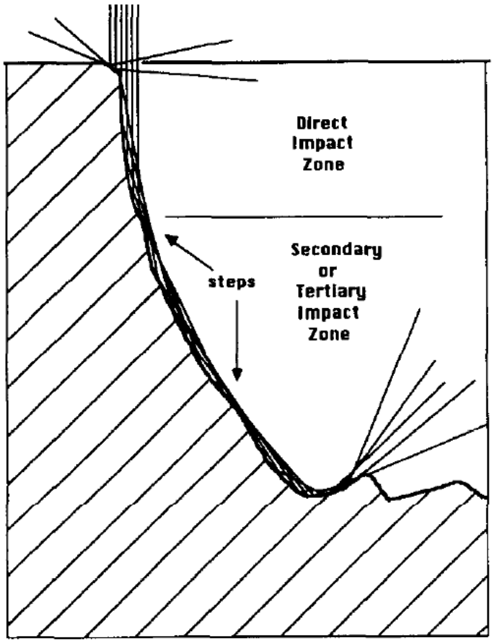

Fig. 2.8. Schematic representation of direct-secondary impact zone [49].

(ii) Kerf formation process in the nozzle traverse direction

According to a visualisation study on AWJ cutting of some transparent materials, such as glass and lexan, three traversal cutting stages in the kerf formation process have been identified [46], namely an entry stage, a developed stage and an exit stage, as shown in Fig. 2.9. In the entry stage, different cutting mechanisms develop until the maximum depth of cut is reached. During this period, cutting is accomplished primarily by erosion at shallow angles of attack. Then, with the increase of the depth of cut, the erosion by large angles of attack dominates the penetration process. The penetration process is fully developed when the cut reaches the maximum depth. This is followed by the developed cutting stage, which is a cyclic and steady cutting process that continues until the jet reaches the end of the material. The exit cutting stage, in which the cutting process comes to an end, is associated with a jet sideward deflection that results in an uncut triangle.

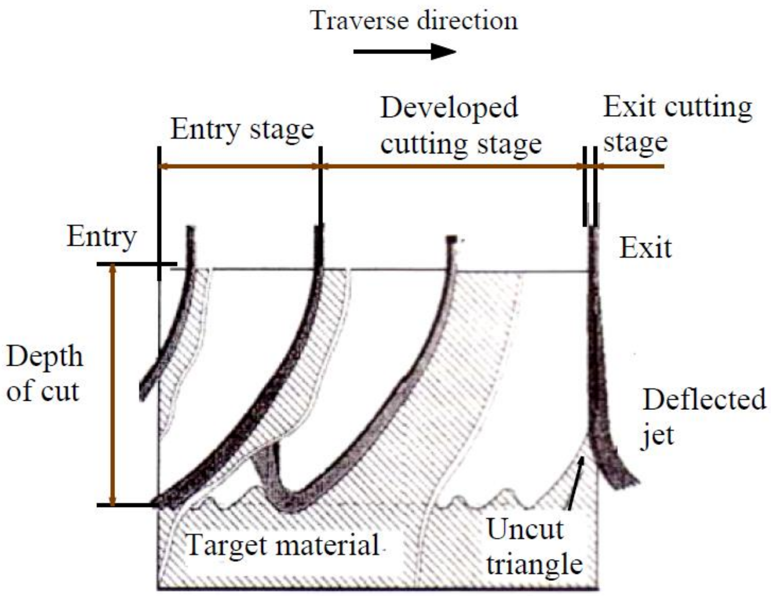

Fig. 2.9. Traversal cutting stages [46].

2.3.3.2 Kerf characteristics

There are two types of kerf produced by AWJ cutting, namely through cut and non through cut, as shown in Fig. 2.10. In both cases, it has a wider entry and its width decreases as the jet cuts into the materials, which results in a kerf taper. This is due to the AWJ losing energy as it cuts into the material. At the top edges of the kerf a small round corner may be generated due to plastic deformation caused by the jet bombardment. The surfaces produced by an AWJ consists of two distinctly different zones as shown in Fig. 2.10(a), the upper smooth zone that is characterised by surface roughness, and the lower striation zone where the surface is characterised by waviness [50, 51]. When the AWJ is unable to cut through the target material, a large pocket is normally formed at the bottom of the kerf, as shown in Fig. 2.10(b). It is because in a non through cut, there is nowhere for the abrasives to go, and they rebound to cause secondary cutting so as to create a large pocket at the lower part of the kerf [52].

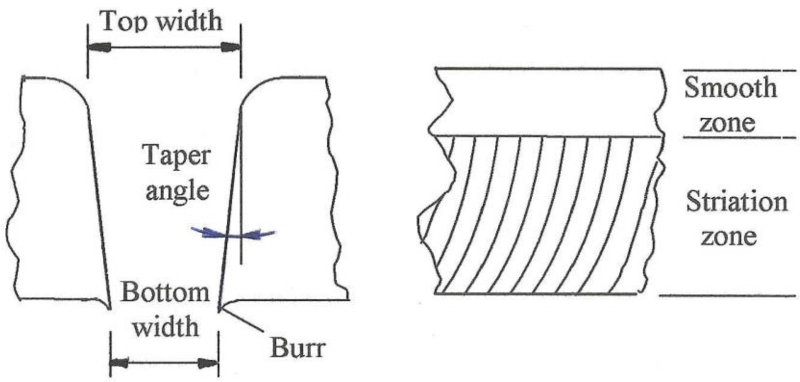

(a)

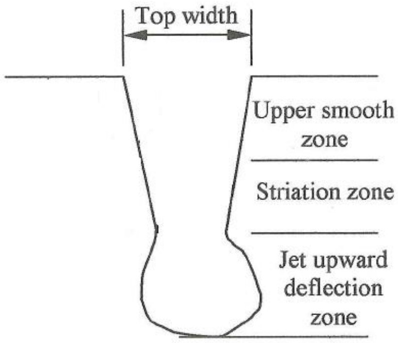

(b)

Fig. 2.10. A schematic of (a) a through cut kerf, and (b) a non through cut kerf [51].

2.3.4 Mathematical cutting models

The increasing applications of AWJ cutting make the modelling of its cutting performance necessary in order to effectively and efficiently control the process. In this section, the mathematical models for predicting the AWJ cutting performance measures, such as the depth of cut and kerf geometrical features, are reviewed.

2.3.4.1 Models for depth of cut

Most of the predictive models reported for the AWJ cutting process attempt to estimate the depth of cut under certain process conditions. These predictive models have been developed according to several different methods, including erosion theories [53, 54], fracture mechanics [55], energy conservation [56, 57] and dimensional analysis [36, 58-61]. These are considered below.

(i) Models based on erosion theories

According to erosion theories [47, 48], the material removal in AWJ cutting of ductile materials can be divided into two zones, namely cutting wear zone and deformation wear zone. As such, a mathematical model for predicting the depth of cut was developed by summing up the depth of cut in the cutting wear zone (h_c) and the deformation wear zone (h_d), i.e.

$$h_c = \frac{C_j d_j}{2.5}\left(\frac{14 m_a}{\pi \rho_p u d_j^2}\right)^{0.4}\left(\frac{v_p}{C_k}\right) \tag{2.14}$$

$$h_d = \frac{1}{\dfrac{\pi d_j \sigma_m u}{2 C_j m_a (v_p - v_e)^2} + \dfrac{C_f}{d_j}\dfrac{v_p}{(v_p - v_e)}} \tag{2.15}$$

where m_a is the abrasive mass flow rate, v_p is the particle impact velocity, u is the nozzle traverse speed, σ_m is the target material flow stress, d_j is the jet diameter, ρ_p is the particle density, v_e is the threshold particle velocity to removal material, C_f is the coefficient of friction on kerf wall, C_j is a constant depending on the particle impact angle, and C_k is the characteristic velocity determined by the following equation:

$$C_k = \sqrt{\frac{3\sigma_m R_f^{0.6}}{\rho_p}} \tag{2.16}$$

where R_f is the particle roundness factor (the ratio of the radius of curvature of the corner to the radius of the maximum inscribed circle in the plane of measurement).

A major assumption made in the above model is that kerf width remains constant over the entire depth of cut, while the kerf walls generally have a taper angle, such that this assumption compromises the accuracy of the model. Then, a more comprehensive model for predicting the depth of cut in AWJ cutting of ductile materials was developed by Paul et al. [62], where the variation of kerf width along the kerf wall was considered, namely

$$h_c = \frac{28 m_a C_j}{2.5\pi\rho_p u w_t \left(1 + w_m / w_t\right)} \left(\frac{v_p}{C_k}\right)^{2.5} \alpha_p^2 \tag{2.17}$$

$$h_d = \frac{C_l - h_c\left(C_l k_i k_j - 1\right)}{1 + C_l k_i k_j - C_l k_i^2 k_j^2 h_c} - h_c \tag{2.18}$$

where w_t is the top width of the kerf, w_m is the minimum kerf width, α_p is the particle impact angle, k_i is a function of the drag coefficient and the jet diameter, k_j is a function of the abrasive velocity and the threshold velocity for material removal, and C_l is the characteristics factor and given by

$$C_l = \frac{\left(1 - C_j\right) m_a \left(v_p - v_e\right)^2}{2\sigma_m w_m u} \tag{2.19}$$

For brittle materials, Zeng and Kim [54] developed a model to predict the depth of cut based on their work on brittle erosion mechanisms. It assumes that the material removal is caused by the combined effect of plastic deformation and intergranular cracking, and the total amount of material removal is regarded as the accumulation of material removed by individual particles. Thus, the model for predicting the depth of cut is given by

$$h = \left(\frac{\kappa C_v C_y}{1 + C_p} \right)^2 \frac{\varepsilon_p m_a P}{\rho_f D u} \left(\frac{2 f_s v_m d_p \sigma_m \alpha_p^2}{3 \gamma_g E_m} + \frac{\alpha_p}{\sigma_m} \right) \tag{2.20}$$

where κ is the momentum-transfer efficiency, C_v is the orifice efficiency, C_y is the compressibility coefficient, C_p is the abrasive particle concentration, ε_p is the particle impact efficiency factor, m_a is the abrasive mass flow rate, P is water pressure, ρ_f is the fluid density, D is the nozzle inner diameter, u is the nozzle traverse speed, f_s is the effective stress wave energy function, v_m is the Poisson's ratio of the target material, d_p is abrasive particle diameter, σ_m is flow stress of target material, α_p is the particle impact angle, γ_g is the grain fracture energy and E_m is the elastic modulus of the target material.

These models seem to have been comprehensively developed by considering many variables, such as the properties of both the abrasive particle and target material and the major process parameters in relation to the AWJ cutting process, but they are rather complicated in their expression and require a number of coefficients to be determined before they can be used.

(ii) Models based on fracture mechanics

Generally, the erosion of brittle materials involves fractures which are related to the formation and propagation of cracks, and the fracture toughness of the work material is usually considered as a measure of resistance to the propagation of cracks. Two depth of cut models were developed by El-Domiaty and Abdel-Rahman [55] based on two erosion models. The first model was developed under the assumption that the formation of cracks and surface chipping were caused by plastic deformation [63], while the second model was based on the assumption that the size of lateral cracks was proportional to the size of radial cracks, and the depth of the lateral cracks was proportional to the maximum particle penetration [64]. The two models for predicting the depth of cut in AWJ cutting of brittle materials in [55] are given by

$$h = C_2 g_1 \left(\frac{1}{ud_j} \right) \left(m_a v_p^{19/6} r_p^{2/3} \rho_p^{7/12} K_{Ic}^{-4/3} H_m^{-1/4} \right) \tag{2.21}$$

$$h = C_3 g_2 \left(\frac{1}{ud_j} \right) \left(m_a v_p^{22/9} r_p^{2/3} \rho_p^{2/9} K_{Ic}^{-4/3} H_m^{1/9} \right) \tag{2.22}$$

where C_2 and C_3 are constants, g_1 and g_2 are particle impact angle factors, u is the nozzle traverse speed, d_j is the jet diameter, m_a is the abrasive mass flow rate, v_p is the particle impact velocity, r_p is the particle radius, ρ_p is particle density, K_{Ic} is the fracture toughness of the target material, and H_m is the hardness of the target material. In comparison to the predictive models developed from the erosion theories, these models require less coefficients to be determined.

(iii) Models based on energy conservation

The energy conservation approach involves the assumption that the amount of material removal is proportional to the amount of kinetic energy carried by the abrasive particles. Based on this assumption, Chen et al. [56] developed a model to predict the total depth of cut in AWJ cutting of 87% alumina ceramics, which is given by

$$h = 0.9\left(\frac{m_a P}{u^{0.78}}\right) \tag{2.23}$$

where m_a is the abrasive mass flow rate, P is the water pressure and u is the nozzle traverse speed.

Wang [23] also used a similar approach to develop a predictive model for the depth of cut in AWJ cutting of a polymer matrix composite, which is expressed as

$$h = 130.92\frac{m_a^{0.407} P}{d_j u^{0.637} \rho_f} \tag{2.24}$$

where d_j is the jet diameter and ρ_f is the density of the working fluid. The model prediction has shown to be in good agreement with the corresponding experimental data for the depth of cut under specific conditions.

(iv) Models based on dimensional analysis

To consider all the variables in the AWJ cutting process is either impossible or will result in many unknown factors in the predictive models, making these models too complicated or unrealistic to be used in practice. Dimensional analysis [65] is a viable and powerful analytical technique widely used to develop predictive models by relating a large number of independent variables to the physical process outcomes, such as the relationship between the depth of cut and process parameters in the AWJ cutting process [36, 58-61]. In this technique, it is first necessary to investigate and identify the factors which play an important role in the machining process. These factors are then grouped into a series of dimensionless terms to form the general analytical model, and each dimensionless term represents a physical aspect of the process. Regression analysis of experimental data is finally performed to determine coefficients for the equation. In this way, the mathematical model developed avoids superfluousness and provides an accurate representation of the relationship between the independent variables and the physical process outcomes. Although this approach relies on the use of experimental data to obtain the coefficients in the final equations, it can relate the physical quantities to much more influential variables than those obtained from the analytical or empirical approaches.

Wang [58] used the dimensional analysis approach to determine specific unknown factors within an analytical model, and developed a predictive model for the depth of cut in AWJ cutting of alumina ceramics, which is given by

$$h = 1.974 \times 10^{-6} \frac{m_a P^{1.186} d_p^{0.156}}{\rho_f D u^{1.169} S^{0.12}} \tag{2.25}$$

where m_a is the abrasive mass flow rate, P is water pressure, d_p is the particle diameter, ρ_f is the density of working fluid, D is the nozzle inner diameter, u is the nozzle traverse speed and S is the nozzle standoff distance. In the same study, a combination of analytical and dimensional analysis approaches was used to develop a model for predicting the depth of cut with the aid of nozzle oscillation, which can be expressed as

$$h = 1.45 \times 10^{-5} \frac{m_a P^{1.604} d_p^{0.289} \theta_n^{0.229} f_n^{0.169}}{\rho_f D u^{1.169} S^{0.12}} \tag{2.26}$$

where θ_n is the oscillation angle and f_n is the oscillation frequency. Both of the models discussed above were verified experimentally and were shown to provide accurate predictions for the depth of cut.

2.3.4.2 Models for kerf characteristics

It has been reported in the literature that predictive models for the kerf geometrical features (e.g. kerf width and kerf taper angle) were usually developed using regression analysis due to the lack of understanding of the complex kerf formation mechanisms [23, 66-69].

A regression analysis was employed by Wang and Wong [68] to develop predictive models for the kerf geometrical features in AWJ cutting of metallic coated sheet steels. The process parameters, i.e. water pressure, standoff distance, nozzle traverse speed and abrasive mass flow rate, were taken into account. This procedure was conducted using an SPSS package at a confidence interval of 95%. The resulting models are given by

$$\begin{aligned} w_t = &\left(4.33S + 1.14uS - 0.01785uP + 4.33SP - 0.3216P^2\right)\times 10^{-4} \\ &-1.554 + 0.019P \end{aligned} \tag{2.27}$$

$$\begin{aligned} \theta = \tan^{-1}[-&\left(0.0789uP + 3.887m_aS + 1.906uS - 1.363P^2 + 0.02016u^2\right)\times 10^{-5} \\ &+ 0.008P - 0.212m_a - 1.067] \end{aligned} \tag{2.28}$$

where w_t is the top kerf width, θ is the kerf taper angle as defined in Fig. 2.10(a), m_a is the abrasive mass flow rate, u is the nozzle traverse speed, S is the standoff distance and P is the water pressure.

In addition, the dimensional analysis approach was employed by Shanmugam and Masood [60] to develop a predictive model for the kerf taper angle in AWJ cutting of layered composites, which is given by

$$\theta = 0.25\left(\frac{S}{d_j}\right)^{0.451}\left(\frac{E_m d_j^2}{u m_a}\right)^{-1.23}\left(\frac{P}{\rho_f}\frac{m_a^2}{d_j^4 E_m^2}\right)^{-0.84} \tag{2.29}$$

where E_m is the elastic modulus of the target material, ρ_f is the fluid density and d_j is the jet diameter.

2.3.5 Abrasive waterjet micro-machining

From the investigations into the capabilities of the AWJ machining technology, it has been found that the many advantages offered by this technology are desired by the micro-machining industry, and a reduction in scale of current AWJ machining system appears to be an attractive avenue to explore. Thus, the development of the AWJ technology for micro-machining is reviewed in this section.

2.3.5.1 Micro-abrasive waterjet systems

As discussed in Section 2.3.1, AWJ systems can be divided into two classes, the entrainment system and the ASJ system. Since the entrainment system relies on the vacuum created by the high velocity waterjet, it is incapable of effectively combining the abrasive particles with the water stream if the water pressure falls below 100 MPa [4]. By contrast, the ASJ system offers some capabilities that cannot be achieved by the entrainment system in terms of using a relatively low water pressure, a small jet diameter, a high particle concentration and a compact nozzle design, which allow the

ASJ system to perform micro-machining tasks. Thus, the micro-abrasive waterjet systems are normally constructed as an ASJ system.

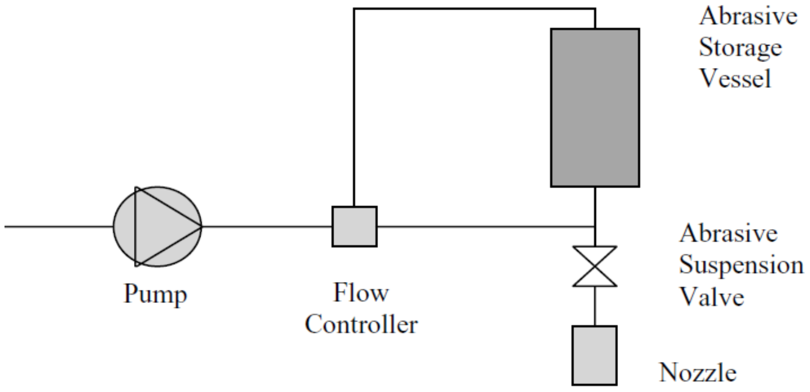

Fig. 2.11. Schematic representation of an ASJ system using a bypass method [5].

Miller [5] has successfully constructed an ASJ system using a bypass method as shown in Fig. 2.11. It consisted of a pump, a flow controller, an abrasive storage vessel, an abrasive suspension valve and a nozzle. The pump was used to increase the pressure of the water in the reservoir, and the pressurised water from a pumping unit was then fed into a flow controller, where the flow controller had a number of functions as described below. When the abrasive storage vessel was turned off, the flow controller directed all of the water from the pump towards the cutting nozzle. When the abrasive storage vessel was turned on, the flow controller directed part of the water flow from the pump to the top of the abrasive storage vessel to push the abrasive mixture out of the vessel to be diluted by water that bypassed the storage vessel. The percentage of water flowing to the storage vessel depends on the abrasive concentration in the storage vessel and the desired abrasive concentration at the nozzle. Further, a suspension valve was placed before the cutting nozzle to completely control the on/off of the abrasive suspension through the nozzle, which allowed the cutting head to move to a new position without depressurising the system. This is essential to minimise cutting cycle times and energy waste. In order to meet this demand, the valve should be able to open and close reliably in abrasive suspension.

A similar bypass design, as shown in Fig. 2.12, was employed by Nguyen et al. [70] and Wang et al. [7] to construct an ASJ system for micro-machining. In this system, the water pressure is controlled by an air-driven pump with an accumulator to stabilise the pressure. Then, the pressurised water is split into two branches, one to provide the hydraulic pressure to a slurry storage tank and the other to a mixing chamber. In this way, the particle concentration ejected through a nozzle could be controlled via the two valves that adjust the water flow rates between the two pipe branches. The accumulation of high density slurry at the bottom of the conically shaped tank allows a constant flow of particles.

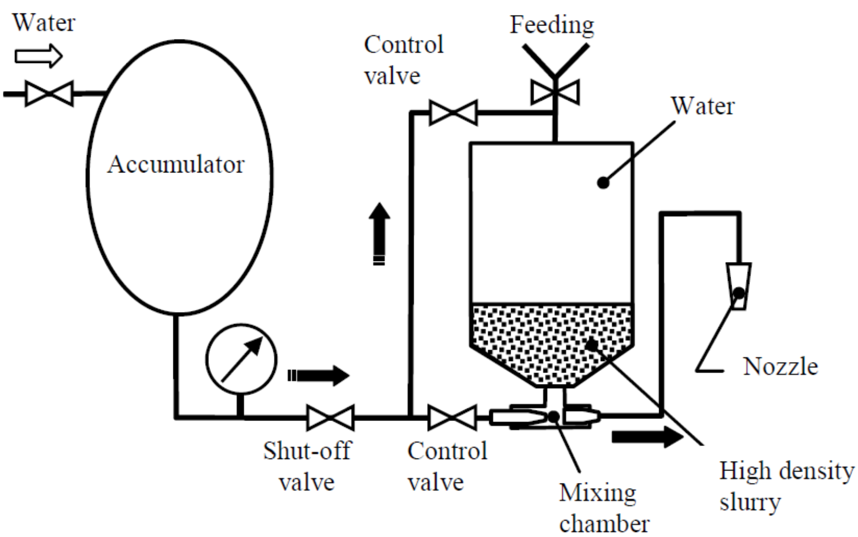

Fig. 2.12. Schematic representation of an ASJ system used for micro-machining [70].

Another ASJ system has been developed by Pang et al. [8] for micro-machining, as shown in Fig. 2.13. In this system, the pressurised water was delivered into a high pressure chamber where it squeezes a bladder containing premixed slurry and forces the slurry to flow into a nozzle and forms an ASJ. The bladder was made of a soft material for isolating the slurry from the incoming water. The pressure chamber was mounted on a shaker vibrating at about 1 Hz to allow the abrasives to be uniformly distributed within the slurry mixture inside the bladder.

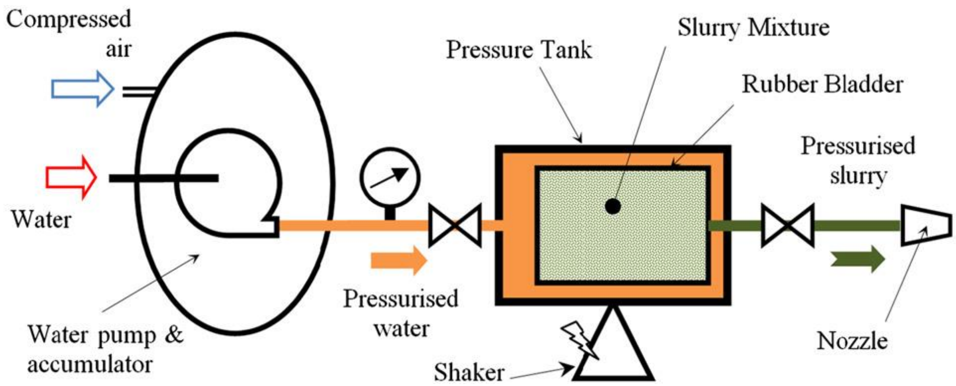

Fig. 2.13. Schematic representation of an ASJ system used for micro-machining [8].

Most recently, an ASJ system was developed by Nouraei et al. [71] using a direct pumping method as shown in Fig. 2.14. It consisted of an open-reservoir slurry mixing tank, a positive displacement slurry pump together with a pulsation damper and a sapphire orifice.

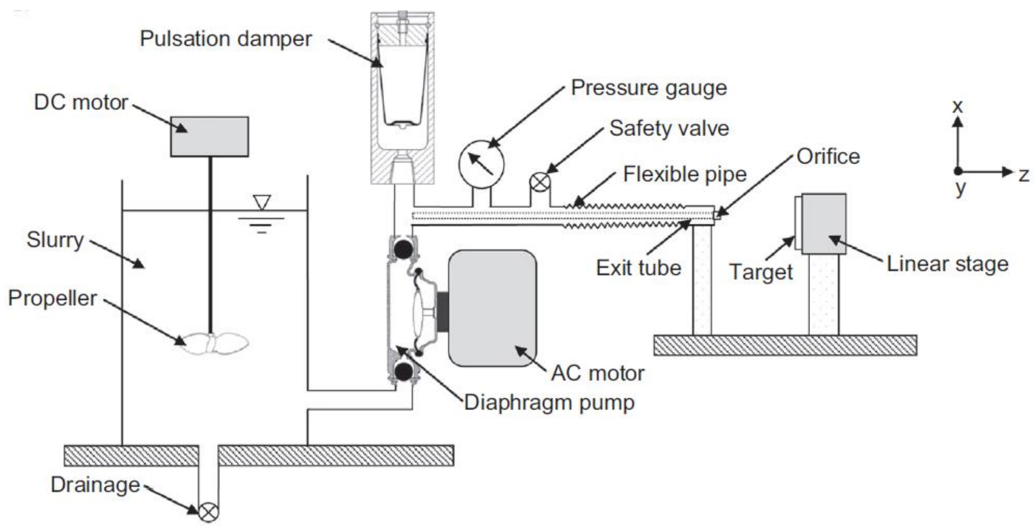

Fig. 2.14. Schematic representation of an ASJ system using direct pumping method [71].

2.3.5.2 Capabilities of current systems

Miller [5] successfully demonstrated the capability of an ASJ for micro-machining. He was able to drill micro-holes down to the mean diameters of 85 μm on stainless steel plates with a thickness of 50 μm. The diameter of the hole was about 1.5 times the diameter of the nozzle. In profiling tests, by mounting the nozzle on a precision manipulator arm, fine features were machined on metals, polymers, glasses and composites. However, these studies were limited only to demonstrate the creation of micro-features on different materials.

In order to examine the micro-machining process and the associated science in ASJ micro-machining, some studies have been conducted. An experimental investigation has been carried out by Nguyen et al. [72] to study the effect of liquid properties on the stability of an ASJ by adding polymeric additives to the fluid as a means to enhance the machining performance. It has been shown that a jet becomes more stable with the addition of polymeric additives, mainly attributed to the increase of liquid viscosity. Nguyen et al. [70] and Wang et al. [7] have then employed the ASJ machining system shown in Fig. 2.12 to drill micro-holes on glasses to understand the associated material removal mechanisms. It has shown that a lower pressure ASJ is a viable micro-machining technology for brittle materials. The fluid diversion characteristics when a jet impacts a material surface play a dominant role in the creation of the W-shaped micro-hole features. The direct impact of the jet plays a minor role in material removal, while the viscous flow induced ductile-mode erosion along the target surface is the primary material removal process. This understanding of micro-hole formation mechanisms has formed an essential scientific basis for the development and application of ASJ micro-machining technology. Later, another ASJ machining system shown in Fig. 2.13 was employed to machine micro-channels on glasses in order to understand micro-channel formation mechanisms, and develop predictive models to effectively control and optimise the machining process [8, 73, 74]. It revealed that the ASJ machining of micro-channels differ greatly from those of the ultrahigh pressure AWJ machining process, most notably the contribution of secondary material removal which is significantly influenced by the properties of the viscous flow of the slurry after initially impacting the material. It has been found that the depth of cut can be effectively controlled in ASJ micro-channelling based on the predictive model for the channel depth. However, it has been shown from this study that the bottom surface of micro-channels suffer from severe waviness, which was believed to be caused by the jet deflection during the nozzle traverse motion and water pressure fluctuation [8, 74]. Further effort is required to look into this phenomenon to increase the cutting quality in ASJ micro-machining.

A similar study of the ASJ machining of micro-holes and micro-channels on glasses was conducted using the ASJ machining system shown in Fig. 2.14 [71, 75, 76]. It was able to produce micro-channels with low waviness on the bottom surface, since a pulsation damper was used to eliminate the substantial vibration and stabilise the pump pressure. The mathematical model for predicting the profile of the machined micro-channel was also developed using a surface evolution method similar to [77, 78]. Further, they studied the effect of dilute polymer solution added in the working fluid on the characteristics of micro-channels machined on glasses. It was found that with an increase in the concentration of polymer solution, the top channel width and channel depth decreased but the centreline roughness increased. It was believed to be attributed to the fact that the elasticity and viscosity of the slurry jet increased with an increase in the concentration of polymer solution, which in turn resulted in a reduction in the spread of the jet and a decrease in the impact velocity of the abrasive particles. The limitation of this ASJ machining system is the severe wear in pump components, which means that valve components have to be replaced frequently.

2.3.6 Summary

A large amount of research and development efforts have been devoted to the development of the AWJ machining technology and exploring its associated science. It has been shown that AWJ machining technology has many distinct advantages over other technologies, such as no HAZ, high cutting efficiency, high flexibility and the ability to cut almost any material, particularly difficult-to-machine materials. Thus, using an AWJ for micro-machining becomes an attractive avenue for development. The current micro-abrasive waterjet systems normally use the ASJ system principle. Some studies have been conducted to reveal the material removal mechanisms involved in the lower pressure ASJ micro-machining process, and associated models have been developed to predict the major machining performance measures. Nevertheless, some limitations have also been identified in the current ASJ systems and micro-machining processes, and further effort is needed to develop this promising micro-machining technology.

2.4 Particle impact erosion

Since AWJ micro-machining is a process by which material removal is made by the successive impacts of high velocity micro-particles, it is necessary to understand the material response subject to the high velocity micro-particle impacts, which may differ from the impacts by large particles or at low impact velocity. In this section, common approaches to investigating the particle impact process will be presented, which include analytical models in early studies, experimental investigations and the recently widely used numerical approaches. The limitations and strengths of each method are discussed, and the need for further studies of impact erosion by high velocity micro-particles is highlighted.

2.4.1 Analytical methods

Analytical modelling for particle impact erosions was extensively used in the last century, in which experiments were also used to determine the coefficients in the developed models. In general, four modes of physical interactions between abrasive particles and the target surface have been identified, namely micro-ploughing, micro-cutting, micro-fatigue and micro-cracking (see Fig. 2.15) [79]. In the ideal case, micro-ploughing does not result in any detachment of material from the target surface due to a single pass of individual particles, while material removal can occur owing to the action of many abrasive particles or the repeated action of a single particle. Material may be ploughed aside repeatedly by passing particles and may break off by low cycle fatigue, i.e., micro-fatigue. Micro-cutting causes material removal in chips equal to the volume of the wear grooves, while micro-cracking occurs when highly concentrated stresses are imposed on the target surface by abrasive particles, particularly on the surface of brittle materials, in which material removal from the target surface takes place through the formation and propagation of cracks. Micro-ploughing and micro-cutting dominate the erosion of ductile materials, while micro-cracking plays a major role in the erosion of brittle materials.

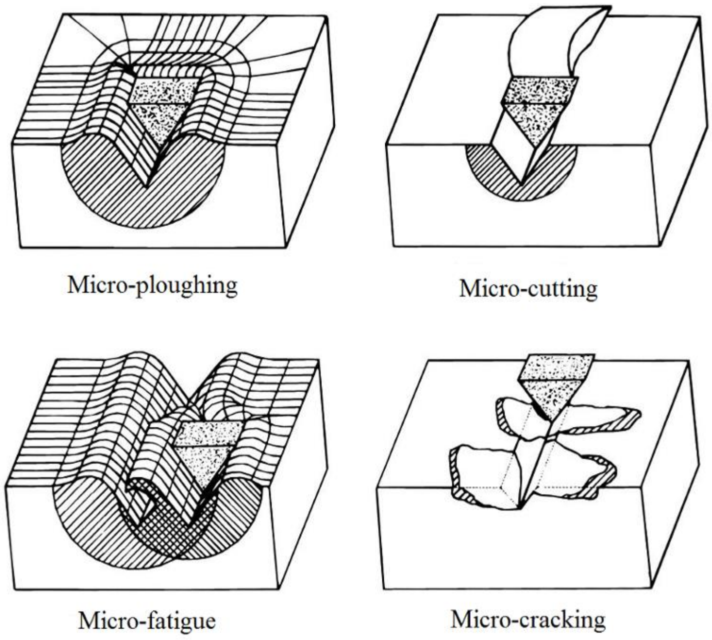

Fig. 2.15. Schematic representation of different interactions between sliding abrasive particles and the target surface [79].

2.4.1.1 Ductile mode erosion

Finnie [47] developed the first mathematical model for the prediction of ductile erosion in 1960, in which he considered erosion as a pure micro-cutting process, and assumed that the erosion process took place in a completely plastic manner. As shown in Fig. 2.16, it is assumed that an ideal ductile material with a smooth surface is impacted by a rigid and angular eroding particle at an angle of α_p, and micro-cutting action stops when the particle tip leaves the surface (i.e., y_t=0). Thus, the material removal volume (V_s) by a single particle cutting is given by

$$V_s = \frac{m_p v_p^2}{\sigma_m R_y \psi}\left[\sin(2\alpha_p) - \frac{6}{R_y}\sin^2\alpha_p\right], (\tan\alpha_p \le \frac{R_y}{6}) \tag{2.30}$$

$$V_s = \frac{m_p v_p^2}{\sigma_m R_y \psi}\left(\frac{R_y \cos^2\alpha_p}{6}\right), (\tan\alpha_p > \frac{R_y}{6}) \tag{2.31}$$

where m_p is the mass of a single particle, v_p is the particle impact velocity, α_p is the particle impact angle, σ_m is the target material flow stress, R_y is the ratio of vertical force to horizontal force (F_y/F_x) and ψ is the ratio of contact depth to impingement depth (y_c/y_t).

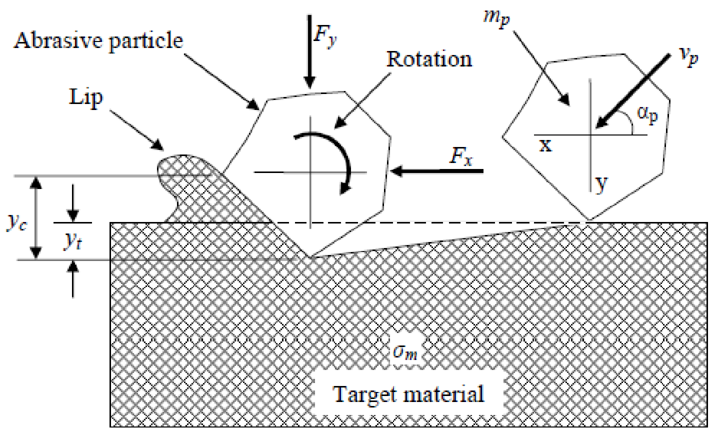

Fig. 2.16. Micro-cutting model of impact erosion [47].

This model showed good agreement with experimental data at shallow angles of attack and correctly predicted a high erosion rate at an impact angle between 15° and 30°, but it also contained several discrepancies mainly concerning the effect of flow stress and the inability of the model to deal with the impact angle of 90°. This model also indicates that wear is proportional to the square of particle impact velocity while experimental findings show that the exponent of particle impact velocity is greater than two and increases with an increment of the particle impact angle. Therefore, in order to improve this model, Finnie modified some of the exponents to compensate for particles which do not remove materials in the ideal situation [80, 81].

Bitter [48, 82] also developed a model to predict the erosion of ductile materials based on the combined effect of cutting wear and deformation wear. Cutting wear referred to the cutting action of the free moving particles and generally takes place when the particle impacts the workpiece at shallow angles. Since this type of wear deals with particles moving across the workpiece, it is mainly associated with the component of particle velocity parallel to the workpiece. As such, to consider whether the tangential component of particle velocity has become zero when the particle leaves the workpiece after the collision, two predictive models for material removal due to cutting wear can be expressed as

$$V_{sc} = \frac{2m_p C'\left(v_p \sin\alpha_p - v_e\right)^2}{\sqrt{v_p \sin\alpha_p}}\left[v_p \cos\alpha_p - \frac{C'\left(v_p \sin\alpha_p - v_e\right)^2}{\sqrt{v_p \sin\alpha_p}}\varepsilon_c\right], (\alpha_p \le \alpha_0) \tag{2.32}$$

$$V_{sc} = \frac{m_p}{2\varepsilon_c}\left[v_p^2 \cos^2\alpha_p - K'\left(v_p \sin\alpha_p - v_e\right)^{1.5}\right], (\alpha_p \ge \alpha_0) \tag{2.33}$$

where V_{sc} is the material removal volume due to cutting wear, m_p is the mass of a single particle, v_p is the particle impact velocity, α_p is the particle impact angle, α_0 is the critical impact angle at which the tangential component of particle velocity becomes zero when the particle leaves the surface, v_e is the critical particle velocity below which the collision process remains elastic, ε_c is the cutting wear factor determined experimentally, and *K'* and *C'* are constants related to the particle and target material properties.

Deformation wear is associated with the near normal impact of particles on the target surface, and the material removal is caused by particles repeatedly colliding with the target [48]. Thus, this type of wear is mainly related to the component of particle velocity perpendicular to the workpiece, and material removal due to deformation wear can be expressed as

$$V_{sd} = \frac{m_p}{2\varepsilon_d}\left(v_p \sin\alpha_p - v_e\right)^2 \tag{2.34}$$

where V_{sd} is the material removal volume due to deformation wear, and ε_d is the deformation wear factor obtained experimentally.

As these two processes occur simultaneously during the material removal process and both need to be considered, the total material removal volume (V_s) at every instant is given by

$$V_s = V_{sd} + V_{sc} \tag{2.35}$$

Based on many experimental results, Bitter [82] has found that for softer materials, α_0 is usually smaller (15°) than that for the harder materials (60°), and the total material removal volume shows good agreement with the corresponding experimental data under various conditions.

However, these two models did not account of the effect of particle size or shape on the erosion process. In order to rectify this deficiency, another predictive model for the erosion of ductile materials was developed by Hashish [53], in which he modified Finnie's model to include the effect of the particle shape and modified the exponent of particle impact velocity. The final form of his model, which is more suitable for shallow angles of attack, is given by

$$V_s = \frac{7}{\pi}\frac{m_p}{\rho_p}\left(\frac{v_p}{C_k}\right)^{2.5}\sin(2\alpha_p)\sqrt{\sin\alpha_p} \qquad (2.36)$$

where V_s is the total material removal volume by a single particle, m_p is the mass of a single particle, v_p is the particle impact velocity, α_p is the particle impact angle, ρ_p is the particle density, σ_m is the target material flow stress, and C_k is the characteristic velocity determined by Eq. (2.16).

There have also been a large number of other investigations dealing with the erosion of ductile materials, but most of them were derived from the two fundamental models proposed by Finnie and Bitter. Some mathematical models for predicting the depth of cut in AWJ cutting were also developed based on these models as discussed in Section 2.3.4.

2.4.1.2 Brittle mode erosion

The erosion of brittle materials is quite different from that of ductile materials. It has been found that the erosion of brittle materials by a solid particle impact is somewhat similar to that under a quasi-static indentation test [83]. When a brittle solid is subjected to a point load by, say, a sharp rigid indenter, an intense stress field is generated. These intense stresses (shear and hydrostatic compression) are relieved by local plastic flow or densification around the tip of the indenter. When the load on the indenter increases to a critical value, the tensile stresses around the contact zone initiate micro-cracks, which can include lateral cracks parallel to the target surface and radial/median cracks into the substrate. The lateral cracks then propagate and terminate at the target free surface, resulting in actual material removal, while the radial cracks running into the substrate cause a decreased strength of the substrate. Fig. 2.17 shows a simplified representation of brittle erosion by a single particle impact, where in reality more than one lateral and redial/median crack can be observed.

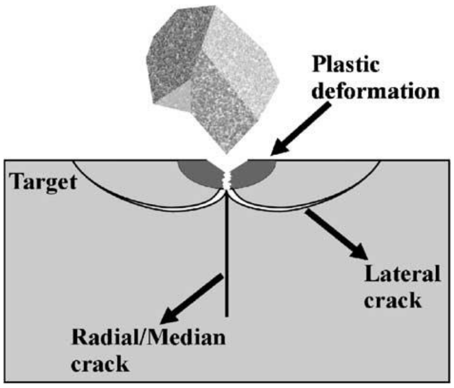

Fig. 2.17. Schematic representation of brittle erosion by a single particle impact [84].

The models for predicting the erosion of brittle materials can be roughly divided into three types: (1) the conical crack model which was based on the assumption that the erosion of target material is entirely due to the propagation of cracks and chipping; (2) the lateral crack model which was based on the assumption that plastic deformation significantly contributes to the formation and propagation of cracks and surface chipping; and (3) the intergranular crack model which was developed to predict the erosion of ceramics. These are discussed below.

(i) Conical crack model

Sheldon and Finnie [85] proposed a conical crack model by assuming that the contact stresses resulting from the particle impact cause crack growth from pre-existing flaws in the target and the material removal from the target is due to the propagation of cracks and chipping. The load at which crack propagation occurs is related to the distribution of pre-existing flaws in the materials which can be obtained through the use of Weibull statistics. Thus, the final model for predicting the material removal volume (V_s) is expressed as

$$V_s = k_b r_p^b v_p^c \tag{2.37}$$

where k_b is a constant determined from the properties of the workpiece, and b and c are constants dependent on the shape of the particle.

This model gives a reasonably accurate prediction of the erosion, but the drawback is that the formation and propagation of lateral cracks are neglected which significantly contribute to material removal in the erosion of brittle materials.

(ii) Lateral crack model

A lateral crack model for predicting the erosion of brittle materials was developed by Evans et al. [63] using an elastic-plastic erosion theory. The amount of material removed is determined from the depth and maximum length of the lateral cracks. It is assumed that the size of the lateral cracks is associated with the size of the plastic deformation zone. This is because lateral cracks are caused by in-plane tensile stresses which are at their maximum near the elastic-plastic zone boundary. Thus, the critical step in deriving this model is to determine the size of the lateral cracks, and the following relation has been obtained.

$$V_s \propto v_p^{19/6} r_p^{11/3} \rho_p^{19/12} K_{Ic}^{-4/3} H_m^{-1/4} \tag{2.38}$$

where v_p is the particle impact velocity, r_p is the particle radius, ρ_p is the particle density, K_{Ic} is the fracture toughness of the target material, and H_m is the hardness of the target material.

Wiederhorn and Lawn [64] also developed a lateral crack model based on the elastic-plastic theory with different assumptions. It is assumed that the size of lateral cracks is proportional to the size of radial cracks and the depth of lateral cracks is proportional to the maximum particle penetration. They derived a model similar to that of Evans et al. [63] although different assumptions were made, and the material removal volume obtained is given by

$$V_s \propto v_p^{22/6} r_p^{11/3} \rho_p^{11/9} K_{Ic}^{-4/3} H_m^{1/9} \tag{2.39}$$

Based on these two lateral crack models, it can be found that the erosion of brittle materials primarily depends on the properties of both the particle and target material, and the most important material property relevant to erosion resistance in brittle materials is fracture toughness rather than hardness.

(iii) Intergranular crack model

According to experimental investigations on the erosion damage of structural ceramics, Ritter and his co-workers [86, 87] developed an intergranular crack model to predict the erosion of structural ceramics. It is assumed that the erosion damage caused by the impacting particle is in the form of grain boundary cracking, and the energy associated with the formation of a pit is the grain boundary fracture energy multiplied by the product of the number of grains per pit and the surface area per grain, where the surface area per grain is proportional to the square of the average grain diameter (d_g). The size of the pit is proportional to the kinetic energy of the impacting particle (U_k), and the volume of the material removed by a particle impact is obtained by taking the cube of the pit diameter, as shown by the following relation:

$$V_s \propto \frac{d_g E_m U_k}{K_{Ic}^2} \tag{2.40}$$

where K_{Ic} and E_m are respectively the fracture toughness and elastic modulus of the target material.

The analytical models for impact erosion have been discussed in this section. However, the extent of these models for the fundamental understanding of material removal in a high velocity micro-particle impact process may be limited. Firstly, these models were mainly developed in a quasi-static manner, but high velocity particle impact is a typical dynamic problem. Secondly, the large numbers of coefficients involved in these models need to be determined from experimental data before they can be used, and there are still many unknown factors from these analytical models. Consequently, using these models to reveal the complicated impact process is almost impossible.

2.4.2 Experimental investigations

Some experimental work has been carried out to explore the impact process by high velocity micro-particles, and the erosion mechanisms obtained from the experimental studies are generally derived from analysing the morphology of the eroded surfaces using a high-powered microscope or scanning electron microscopy (SEM). The erosion of silicon single crystals by angular alumina particles was experimentally investigated over a range of particle diameters (23 to 270 μm), velocities (32 to 134 m/s) and impact angles (22° to 90°) [88]. It has been found from the morphology of the eroded surface, as shown in Fig. 2.18, that the impact erosion is in a brittle-mode nature and material is removed by the impact that causes the propagation of lateral cracks periodically diverging upward and terminating at the free surface. An experimental investigation into the erosion mechanisms of alumina ceramics by the impacts of different types of micro-particles with an average diameter varying from 15 to 25 μm was carried out by Wakuda et al. [89]. They found clear evidences of intergranular cracking, plastic flow and crushed grain particles in the target material as shown in Fig. 2.19, and identified that intergranular cracking played the most important role in material removal during the impact process. In addition, a study of the erosion of monocrystalline silicon under the impact of high velocity micro-particles has also been conducted by Li et al. [90] and Basak et al. [91]. It has been found that the impressions produced by a single micro-particle impact can be classified into three categories, namely large-scale craters, large-scale scratches, and small-scale micro-dents, as shown in Fig. 2.20, in which the large-scale craters are found to be responsible for instant material removal through brittle-type cleavage fracture formation (see Fig. 2.21). Some fundamental erosion mechanisms could be concluded by analysing the morphology of eroded surfaces, but the dynamic impact process cannot be observed experimentally due to the very short impact period between the impacting particle and target surface.

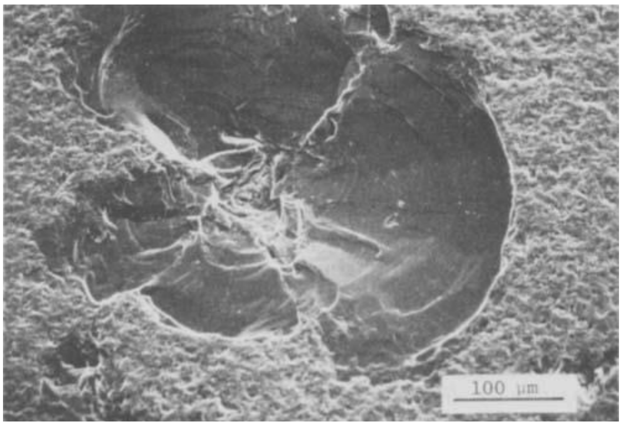

Fig. 2.18. SEM micrograph of eroded silicon single crystals by the impact of 270 µm alumina particle at the velocity of 108 m/s and impact angle of 90° [88].

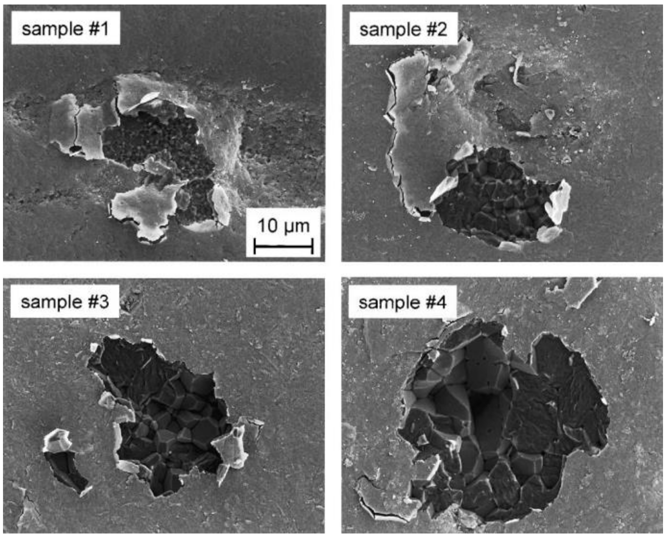

Fig. 2.19. High magnification of alumina surface impacted by micro-particles [89].

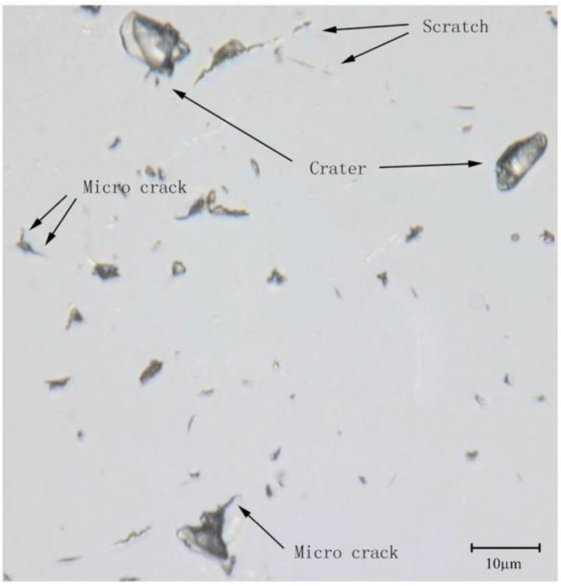

Fig. 2.20. Morphology of an eroded surface under the impacts by micro-particles [90].

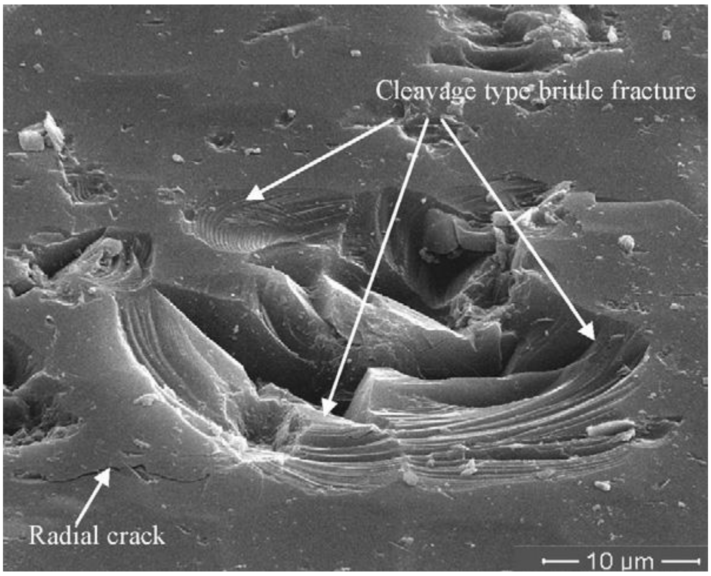

Fig. 2.21. Representative SEM micrograph of a crater impression exhibiting cleavage-type brittle fractures [91].

2.4.3 Numerical methods

2.4.3.1 Finite element method

Finite element (FE) method is a powerful tool to study a wide range of complicated problems that cannot be addressed experimentally. It is a numerical technique to find an approximate solution to the governing partial differential equations by dividing a very complicated problem into small elements that can be solved in relation to each other. It normally does not require as many assumptions as the analytical method, and can reveal the detailed process that cannot be obtained experimentally. Therefore, the FE method has been used to study material response to both single and multiple impacts by high velocity particles and to explore the associated material removal mechanisms.

(i) Studies on single particle impact

The FE method has been employed to model the impact process by a single particle on both ductile and brittle materials. For ductile materials, Li et al. [37] developed an FE model to comprehensively investigate material response to ultrahigh velocity micro-particle impact. Three material failure modes (failures induced by inertia, elongation and adiabatic shear banding) were identified, which are more comprehensive than the well-known cutting and deformation wear modes and provide a deeper understanding of the ductile impact erosion mechanisms. For brittle materials, Flocker and Dharani [92] studied the development of cracks on a glass during the impact by assigning a crack propagation path, while Behr et al. [93] investigated the dynamic strains on a laminated glass by the impact of low velocity steel balls. In these studies, it was assumed that the material was perfectly elastic, so that the damage pattern is difficult to observe. Continuum damage mechanics (CDM) coupled with the FE model was also proposed. Sun et al. [94, 95] used a CDM model to examine the mechanical response of a thin glass plate to the impact of a large ball at relatively low velocities. Although the mesh in their FE model was rather coarse, some damaged elements were revealed in both sides of the thin plate. Ismail et al. [96, 97] also used a CDM-based FE model to predict the nucleation and crack propagation direction in a glass subject to static indentation, and the impact damage on the glass. Predicted results were found to be in good agreement with those experimentally obtained.

(ii) Studies on multiple particle impacts

Since material removal in AWJ micro-machining is regarded as an accumulation of the material removed by the impacts of a flow of high velocity micro-particles, it is important to understand the damage accumulation process and the associated material removal mechanisms. For this purpose, some important investigations have been carried out to simulate the multiple impact process relevant to AWJ machining [38, 98, 99] using FE models. A multiple micro-particle impact process was modelled by Li et al.

[38] in which the Monte Carlo method was employed to generate a stochastic flow of impacting particles and the thermal exchange was considered during the whole impact process. It was found that the inertia-induced fracture is the primary material removal mechanism for normal impacts, while it is the thermal-instability-driven failure that contributes to the higher material removal rate at oblique impacts. Anwar et al. [98, 99] used an FE model to simulate the AWJ milling process for titanium alloy, in which the impacting particles involved in the particle flow were modelled in layers in order to reduce the computation time, and these layers were spaced close to each other to make the impact interval close to that in the real AWJ cutting process. It has been shown that this model enables an accurate prediction of the jet footprints and material erosion rate.

It is noted that most of the numerical studies using the FE method are focused on the erosion of ductile materials, where plastic deformation and thermal diffusion dominate the material removal process, while few studies have been carried out to represent erosion damage of brittle materials by the impact of high velocity single micro-particles, where material removal is mainly caused by the propagation and intersection of cracks. In order to simulate the material removal process for brittle materials, finding a proper way to deal with the formation and propagation of a large number of cracks is important and always challenging.

2.4.3.2 Discrete element method

Discrete element method (DEM) [100] has been used for the analysis of rock mechanics, where a material is treated as a solid specimen with arbitrarily sized spherical elements bonded together. It can simulate the behaviour of material formed by assembling many spherical elements through bonding at their contacts by what is called the bonded-particle model (BPM) [101]. The breakage of the bonds among the elements can represent the formation and propagation of cracks in the specimen to study the erosion process. Thus, the DE method is a promising approach to model the erosion process for brittle materials.

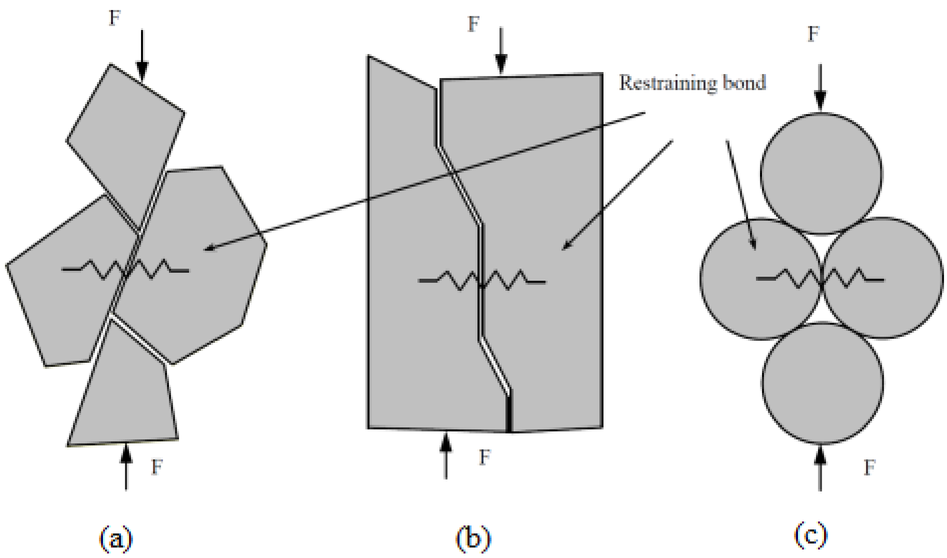

Fig. 2.22. Comparison of the formation of cracks between a real target and the solid specimen constructed with BPM: (a) physical wedge crack, (b) physical staircase crack, and (c) breakage (crack) among spherical elements in a solid specimen [101].

The mechanical behaviour of brittle materials subject to an external force or moment is mainly governed by the formation, propagation and eventual intersection of cracks. Fig. 2.22 shows a comparison of the formation of cracks between the solid specimen constructed with BPM and the real target material. Physical cracks in a real target material occur once a large enough force or moment is applied to the target material as shown in Figs. 2.22(a) and (b), while similar breakages (cracks) also occur among the spherical elements in a solid specimen subject to a large enough force or moment as shown in Fig. 2.22(c). Many such breakages (cracks) would occur inside a solid specimen that contains thousands of bonded spherical elements to represent the erosion process in a brittle material.

The DE model has found application in simulating the machining process for brittle materials. Huang [102] used a DE model to simulate a rock cutting process and found that the transition of failure modes was related to the depth of cut. Lei and Yang [103] used this method to simulate the material removal process in the machining of ceramics and found that both the median and lateral cracks obtained from the simulation were very similar to the cracks observed experimentally. Shen and Lei [104] and Shen et al. [105] developed a DE model to represent the laser-assisted machining process for ceramics and explore the associated material removal mechanisms. Tan and his co-workers [106, 107] also used a DE model to investigate crack length and depth in the scratching of alumina ceramics. They found that both the maximum surface crack length and subsurface crack depth increased as the scratching depth increased. From the above analysis, the DE method appears to be a very promising approach to the study of the crack formation and propagation process and the material removal mechanisms for brittle materials under the impact of high velocity micro-particles.

2.4.4 Summary

In contrast to the analytical and experimental approaches to the investigations into particle impact erosions, numerical methods can provide a deeper understanding of the single and multiple impact processes and the associated material removal mechanisms. The FE method has been comprehensively used to simulate ductile erosion by the impact of a single particle or multiple particles, while few studies have been reported to model the brittle erosion process which involves primarily the formation, propagation and intersection of cracks. DE models appear to be a suitable method to understand the erosion process for brittle materials.

2.5 Concluding remarks

In this chapter, a comprehensive literature review has been conducted on the development of AWJ machining technology and the understanding of particle impact erosion. The various micro-machining technologies were first reviewed to highlight the need for an alternative micro-machining technology. It has been found that traditional machining technologies are incapable of meeting the requirements of micro-machining tasks by the manufacturing industry, while non-traditional machining technologies have limitations. For instance, laser machining often results in HAZ zones around cut features, EDM is applicable only to electrically conductive materials, while chemical etching is associated with low MRR in addition to its negative environmental impact.

AWJ machining is a process in which a high velocity abrasive waterjet is used to remove material by means of impact erosion. It possesses some beneficial characteristics, such as no HAZ, high cutting efficiency, high flexibility and the ability to cut almost any material, particularly difficult-to-machine materials. Thus, in recent years it has been rapidly accepted by industry for machining applications.

The studies of the AWJ jet characteristics have been briefly reviewed in this chapter. Analytical investigations into the structure of a pure waterjet have shown that a waterjet generally consists of three regions, namely a potential core region, a transitional region and a main region. A simple and practical model to predict the velocity of the particles at any location within a jet stream from the nozzle exit has been developed using the

CFD method, and it has been found that particle velocities are characterised by a decay in the axial direction, and exhibit a top-hat profile across the diameter of the jet at a given cross-section downstream from the nozzle exit.

In AWJ cutting, the combined effect of impacting particles results in the removal of the target material to form a kerf. Three traversal cutting stages in the kerf formation process have been identified, namely an entry stage, a developed stage and an exit stage. Generally, a smooth zone is formed at the upper part of the machined surface, while at the lower part, a striation zone exists. In a through cut, the kerf shows a wider entry and its width decreases as the jet cuts into the material, which results in a kerf taper. In a non through cut, a large pocket is normally formed at the bottom of the kerf due to the secondary cutting action of the particles.

The mathematical models for predicting the various cutting performance measures have been reviewed. It has been found that most of the models have been developed to predict the depth of cut using erosion theories, fracture mechanics, energy conservation and dimensional analysis. While these models provide an effective way to predict the depth of cut, most are very complex and not practical to be employed in practice. By contrast, the dimensional analysis technique has proven to be a reliable approach to the modelling of engineering problems and has been successfully applied to model the depth of cut and other kerf characteristics in AWJ machining.

The review of the development of AWJ technology for micro-machining applications has shown that AWJ micro-machining normally uses an ASJ system. It has been found that viscous flow induced ductile-mode erosion dominates the formation of micro-holes and micro-channels on glasses by using a relatively low pressure ASJ. Predictive models have been developed for the major machining performance measures. The limitations of current technology indicate that more studies are essential to develop this micro-machining technology before it can be used commercially by industry.

Finally, a review of analytical, experimental and numerical methods for studying the impact process by high velocity micro-particles was presented. It has been found that in ductile mode erosion, the main cause of material removal is micro-cutting or micro-ploughing, while in brittle mode erosion material removal is mainly caused by the formation and propagation of micro-cracks. It has further been found that the numerical method is a powerful tool to study a wide range of complicated problems that cannot be addressed experimentally. The FE model, as one of the widely used numerical methods, has been successfully used to simulate ductile erosion by the impact of single and multiple particles, while few studies have been conducted to model brittle erosion which is caused mainly by the propagation and intersection of cracks. The DE method treats a material as a solid specimen with arbitrarily sized spherical elements bonded together, and the breakage of the bonds among the elements can represent the formation and propagation of cracks in the specimen. Thus, the DE method appears to be a promising approach for modelling the impact process for brittle materials.

The review in this chapter has shown that only a limited research effort has been made on the AWJ micro-machining process. The reported studies indicate that there is significant room for the technology to be improved to increase the cutting performance, such as the machined surface quality. While earlier studies considered a host of process parameters, some other important parameters, such as the abrasive particle size and jet impact angle which have been shown to have a significant effect on the AWJ cutting process, have yet to be studied in the micro-channelling process, let alone the development of mathematical models for predicting the micro-channelling performance for the effective control of the process. In addition, it has been revealed that there are very few reported studies of the impact event on brittle materials by high velocity micro-particles as well as the erosion process and mechanisms. Therefore, an investigation, possibly through a computational study using the DE method, is essential to provide the required knowledge for the development of AWJ machining technology.

Chapter 3

Experimental study of the micro-channelling process and single impact erosion

3.1 Introduction

Quartz crystals have a special property of piezoelectricity, finding wide applications in resonators, oscillators, micro-sensors, actuators, and frequency standards, etc. [108, 109], and whose performance greatly depends on the quality of the manufactured micro-structures, like micro-channels and micro-holes, on the quartz crystals. For high performance and reliability of the devices, these micro-features need to be fabricated with no or minimum process-induced damage. However, the hard and brittle quartz crystals are considered as difficult-to-machine materials and an enabling technology is needed for fabricating micro-features on the materials with good surface integrity and machining efficiency.

As pointed out in the Literature Review, ASJ micro-machining is a relatively new processing technology with some distinct advantages of no HAZ, high flexibility, high cutting rate and the ability of cutting almost any materials over other machining technologies such as laser machining, EDM and chemical etching. It gains particular favour in processing difficult-to-machine materials, although more research is needed to bring this technology to commercial application. Some preliminary studies have found that this technology enables the machining of micro-holes and micro-channels to a desired depth on glasses, while it has also been found that the micro-channels that are formed suffer from severe waviness on the bottom surface [8, 73, 74]. It is thus necessary to improve the cutting quality in ASJ micro-machining. In addition, an understanding of the erosion process by micro-particle impacts is important for the development of ASJ micro-machining technology. However, little study of the erosion process on quartz crystals by high velocity micro-particle impacts has been reported in order to understand the erosion mechanism.

In this chapter, an analysis of the ASJ micro-channelling process and the characteristics of the micro-channels produced on a quartz crystal are first presented based on an experimental investigation. The machined surface morphology and the micro-channelling performance in terms of MRR, channel depth, channel wall inclination angle and top channel width are discussed with respect to the process parameters. A statistical analysis will be conducted to determine the primary variables that significantly affect micro-channelling performance, followed by a study to examine how each micro-channelling performance measure changes with respect to process parameters. Furthermore, the erosion process by the impact of high velocity micro-particles on a quartz crystal is investigated experimentally to explore the associated erosion mechanisms. The various particle impact velocities and impact angles are considered in experiment, and the impressions formed by individual particle impacts are then examined and analysed to reveal the erosion mechanisms.

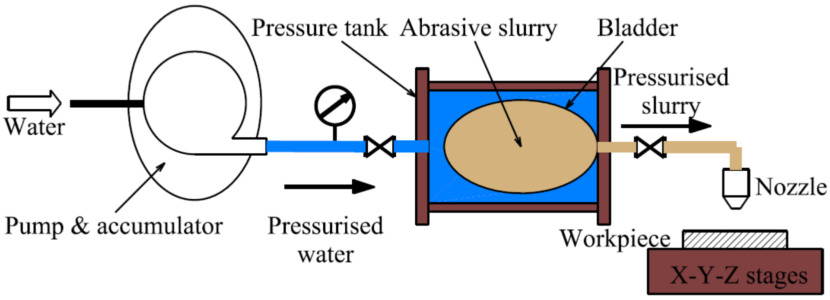

Fig. 3.1. Schematic of experimental setup.

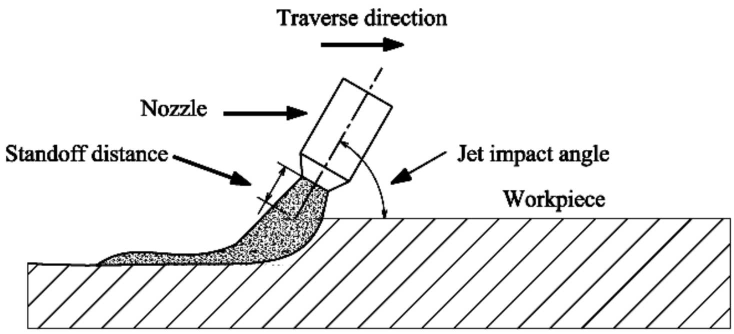

Fig. 3.2. Nozzle and workpiece arrangement.

3.2 Micro-channel machining

3.2.1 Experimental work

The experiment was conducted with an in-house developed ASJ machining system, as shown in Fig. 3.1. In this system, a pressurised air driven pump was used to achieve high water pressure. The pressurised water was then delivered into a high pressure tank where it squeezed a bladder containing premixed slurry and forced the slurry to flow into a nozzle to form a micro-ASJ. The bladder was made of waterproof soft material for isolating the slurry from the incoming water to control the abrasive concentration. A zirconium dioxide ceramic nozzle with an inner diameter of 0.125 mm and 10.5 mm in length was used. This nozzle aspect (length to diameter) ratio allowed the contraction coefficient of the jet to be considered as unity [110]. Three translation stages with the control resolution of 0.01 mm were used to move the nozzle or workpiece in the X-, Y-and Z-directions. The detailed setup of the workpeice with the nozzle is shown in Fig. 3.2, in which the nozzle standoff distance was defined as the distance between the nozzle exit and the target surface along the nozzle centreline, and the jet impact angle was defined as the angle between the nozzle centreline and the target surface.

Table 3.1. Material properties of the quartz crystal used in the experiment.

Properties	Values
Density (g/cm^3)	2.2
Young's modulus of elasticity (GPa)	72
Hardness (GPa)	12.1
Poisson's ratio	0.16
Fracture toughness ($MPa \cdot m^{0.5}$)	1.2

Due to its wide application in electromechanical devices, a quartz crystal (from Zhejiang Crystal-Optech Co. Ltd., China) was used as the specimen material, whose major properties are given in Table 3.1. Silicon carbide (SiC) particles (30.5 GPa hardness and 3.2 g/cm^3 density) with the average particle diameter of 10, 12, 15 and 18 μm were employed as the abrasives. The nozzle standoff distance was kept constant at 2 mm based on previous studies [73]. Since the jet impact angle is a significant factor in affecting the cutting quality in the AWJ machining process [111], four levels of backward jet impact angles at 45°, 60°, 75° and 90° (see Fig. 3.2) were selected. In addition, the water pressure, nozzle traverse speed and abrasive particle concentration were also considered at four levels, as given in Table 3.2. Forward jet impact angles were not included in this study, but may be considered in future investigations.

Table 3.2. Process parameters used in the experimental design.

Process parameters	Level 1	Level 2	Level 3	Level 4
Average particle size, d_p (μm)	10	12	15	18
Particle concentration, C_p (% by mass)	15	20	25	30
Water pressure, P (MPa)	8	12	16	20
Jet impact angle, α_j (°)	45	60	75	90
Nozzle traverse speed, u (mm/s)	0.1	0.2	0.3	0.4

A Taguchi design of the experiment with a standard L16 (4^4) orthogonal array was used for particle size, particle concentration, water pressure and jet impact angle. Each of the 16 combinations was tested under the four nozzle traverse speeds, which resulted in 64 combinations. Additional 28 tests using the parameters given in Table 3.2 were also carried out to improve the data analysis as well as to obtain sufficient "as measured" data for graphic analysis. Thus, a total of 92 tests for machining channels of 5 mm in length were conducted for the study of micro-channelling performance. Each test was repeated at least three times and the average data are used in the analysis.

The channel surface morphology was inspected by using a Keyence VHX-100 3D digital microscope, while the channel characteristics (depth, top width and wall inclination angle) were obtained with the assistance of a Keyence VK-X200 3D laser measurement microscope. Four measurements of the cross-section profile for each channel were carried out and the average was taken. Further, the surface roughness (centreline average R_a) was measured along the traverse direction with the Keyence VK-X200 3D laser measurement microscope with the cut-off wavelength of 0.8 mm. The measurements of the surface characteristics were essentially made on the channel bottom surfaces.

3.2.2 Results and Discussion

3.2.2.1 Micro-channelling performance

Fig. 3.3 shows a typical machined channel in a 2D and a 3D view as well as a cross-sectional profile. It exhibits a U-shaped profile characterised by a wider entry at the top and the channel width reduces downwards, so that the channel walls incline by an angle as shown in Fig. 3.3(c). The channel depth was measured along the centreline of the channel, and the top channel width was defined by using the intersection of fitted straight lines for the sidewalls with the workpiece top surface (see Fig. 3.3(c)).

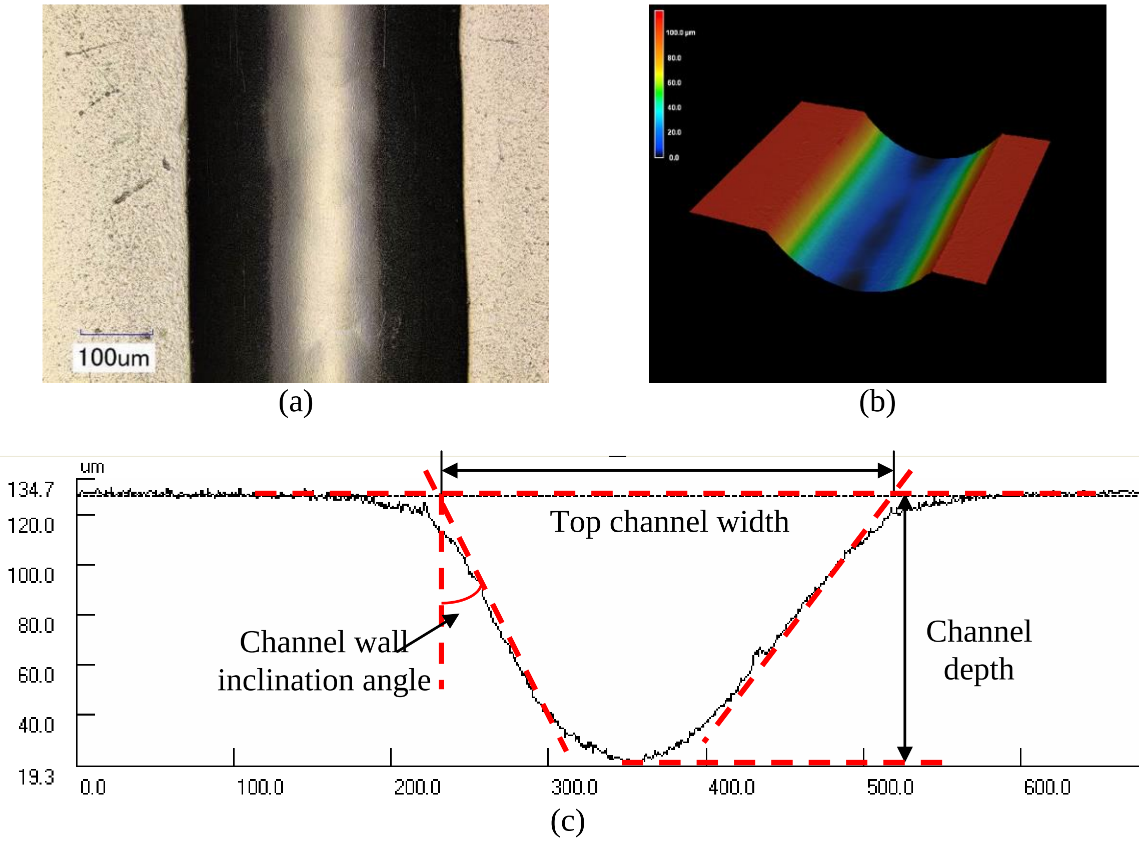

Fig. 3.3. Micro-channel characteristics: (a) top view, (b) 3D view, and (c) cross-sectional profile (d_p=12 μm, P=16 MPa, C_p=15%, α_j=90° and u=0.2 mm/s).

Earlier studies [8, 74] have indicated that channel bottom surfaces machined by ASJ are characterised by wavy patterns, and it was believed to be caused by jet deflection and the secondary viscous flow. It has further been found that the shaker used on the pressure tank in previous studies to minimise the deposition of particles in the slurry contributed to the fluctuation of the slurry pressure and hence to the wave formation. As such, the experiment in this study was improved and the shaker was turned off during the test process. It was expected that during the short duration of each test (maximum of 50 s) the particle setting would not cause a major concern in affecting particle concentration. Furthermore, a backward jet impact angle was used to facilitate the scanning action of the particles so as to increase the surface quality, although it is understood that the use of a backward impact angle may be at the sacrifice of MRR. With this experimental setup, no large wavy pattern is discernible, as shown in Figs. 3.3(a) and (b).

Table 3.3. The analysis of variance for the micro-channelling performance.

	Bottom surface roughness		Material removal rate		Channel depth		Top channel width		Channel wall inclination angle	
Process parameters	P	F	P	F	P	F	P	F	P	F
Particle size	0.00	13.20	0.00	39.46	0.00	16.57	0.00	23.79	0.00	57.77
Particle concentration	0.07	2.44	0.00	19.95	0.00	6.82	0.00	10.31	0.00	10.99
Water pressure	0.00	12.80	0.00	61.96	0.00	23.98	0.00	20.37	0.00	47.06
Jet impact angle	0.00	6.29	0.00	13.48	0.00	5.04	0.36	1.09	0.00	13.88
Nozzle traverse speed	0.00	17.64	0.00	4.62	0.00	27.40	0.00	58.34	0.00	57.21

An analysis of variance (ANOVA) was conducted to identify the significance of the process parameters considered for the micro-channelling performance (channel bottom surface roughness, MRR, channel depth, top channel width and channel wall inclination angle). Table 3.3 shows the ANOVA results. The P value reports the significance level and, since the analysis was carried out at 5% significance level, when the P value is less than 0.05, the effect of the respective factor is significant to the response variable. By contrast, the F value is the mean square error to residual which is used to determine the relative effect magnitude of a factor; for instance, the nozzle traverse speed has the highest F value and hence the largest effect on the bottom surface roughness. A detailed analysis of the effect of the process parameters on these performance measures is given below.

3.2.2.2 Effect of process parameters on bottom surface roughness

From the ANOVA results given in Table 3.3, it can be found that the nozzle traverse speed has the most profound effect on the surface roughness, followed by particle size, water pressure and finally the jet impact angle. The particle concentration has only a minor effect on the surface roughness. Fig. 3.4(a) shows that increasing the water pressure caused the surface roughness to increase. This may be due to the fact that a higher water pressure results in a higher particle velocity and accordingly a higher particle energy that can cause larger craters on the surface by individual impacts and consequently forms a rougher surface. The roughness of the bottom surface gradually decreases with an increase in the nozzle traverse speed, as shown in Fig. 3.4(b). The reason may be that a higher traverse speed is able to remove only a thin layer of the work material from the polished surface, so that the surface formed is less rough than under a smaller traverse speed where a larger depth of cut is generated by removing the material layer by layer with an accumulated and increased surface roughness. Fig. 3.4(c) shows that an increase in the jet impact angle or particle size results in an increase in the bottom surface roughness. This may be due to the fact that a smaller impact angle gives more impact force tangent to the work surface, so that the erosion involves more cutting action to form a smoother surface. Likewise, since smaller particles carry less energy, the machined surface is formed by the cumulative effect of smaller craters generated by individual particles for a smoother surface. Fig. 3.4(d) shows that the bottom surface roughness increases slightly with an increase in particle concentration. This may be attributed to the increased depth by a higher abrasive concentration, which is associated with a rougher surface, as discussed above.

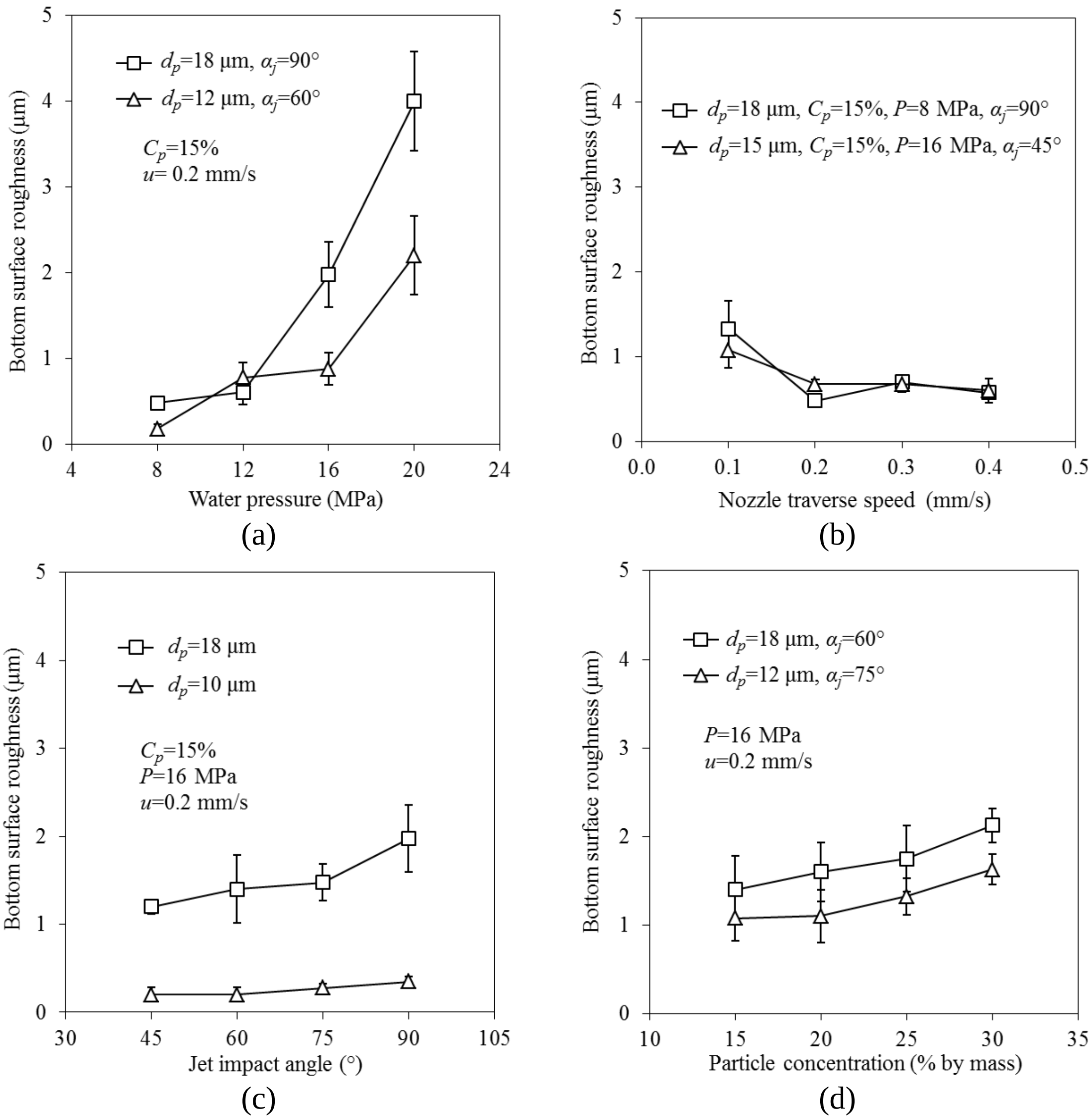

Fig. 3.4. Effect of process parameters on the bottom surface roughness (the scatter bars show standard deviation).

3.2.2.3 Effect of process parameters on material removal rate

According to the ANOVA results in Table 3.3, water pressure plays the most important role in affecting the MRR, followed by particle size, particle concentration, jet impact angle and finally nozzle traverse speed. Fig. 3.5 shows the trends of MRR with respect to process variables. It shows that MRR increases with an increase in the water pressure, jet impact angle, particle size and particle concentration in the slurry, and decreases with an increase in nozzle traverse speed. MRR is primarily affected by the amount of kinetic energy brought into the process. This can be achieved by increasing the water pressure, increasing the particle concentration which permits more particles to impact a given area of the material, and using larger particles which can carry more energy if given sufficient acceleration time inside the nozzle. All of the above can result in an increase in MRR. Likewise, an increasing jet impact angle facilitates brittle mode erosion for increasing the removal rate of brittle materials [63, 112, 113].

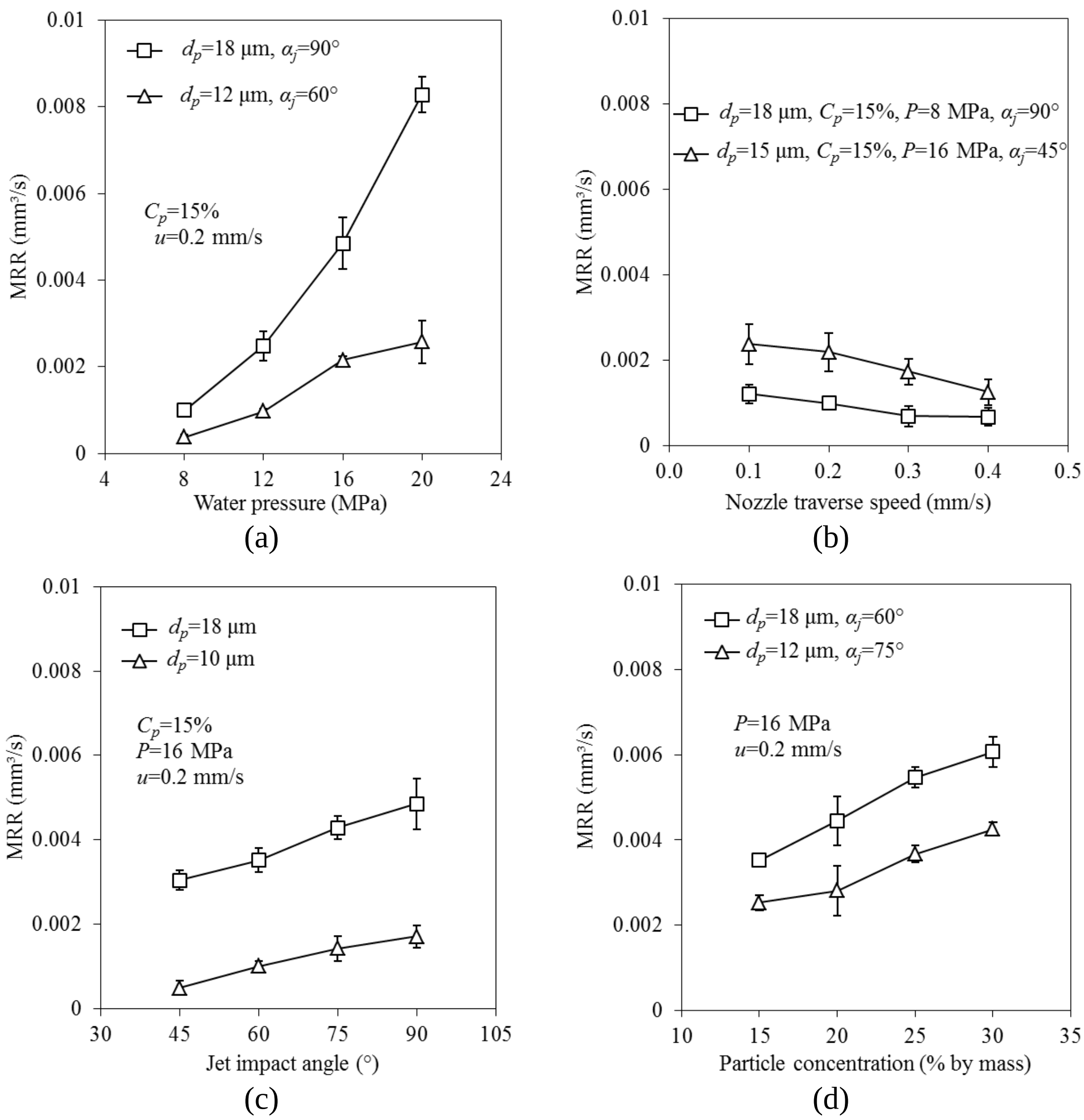

Fig. 3.5. Effect of process parameters on the material removal rate (the scatter bars show standard deviation).

It may be intuitive to believe that the nozzle traverse speed does not affect the MRR, while a reduction in the traverse speed may even reduce the MRR due to increased interference between particles. However, in ASJ machining, a thin water layer on the work surface may cause a shielding effect on the cutting efficiency of the impacting particles and this effect is manifested at higher nozzle traverse speeds where the jet more quickly approaches and impacts a new work surface with water film. As such, the MRR shows a slight decreasing trend with an increase in the nozzle traverse speed (see Fig. 3.5(b)).

3.2.2.4 Effect of process parameters on channel depth

The statistical analysis in Table 3.3 shows that the nozzle traverse speed has the most significant effect on channel depth, followed by water pressure, abrasive size, abrasive concentration and finally the jet impact angle. The channel depth shows an increasing trend with an increase in water pressure, abrasive size, abrasive concentration and jet impact angle, as shown in Figs. 3.6(a), (c) and (d). An increase in the water pressure, abrasive size and abrasive concentration allows more jet energy to be brought into the cutting process after travelling a short standoff distance, and therefore results in an increased channel depth. Likewise, an increase in the jet impact angle is preferred for brittle mode material removal which increases the erosion rate [63, 112, 113]. By contrast, the channel depth decreases with an increase in nozzle traverse speed, as shown in Fig. 3.6(b). This is mainly due to the fact that a faster passing jet under a higher traverse speed allows less jet-material interaction time which yields a smaller channel depth.

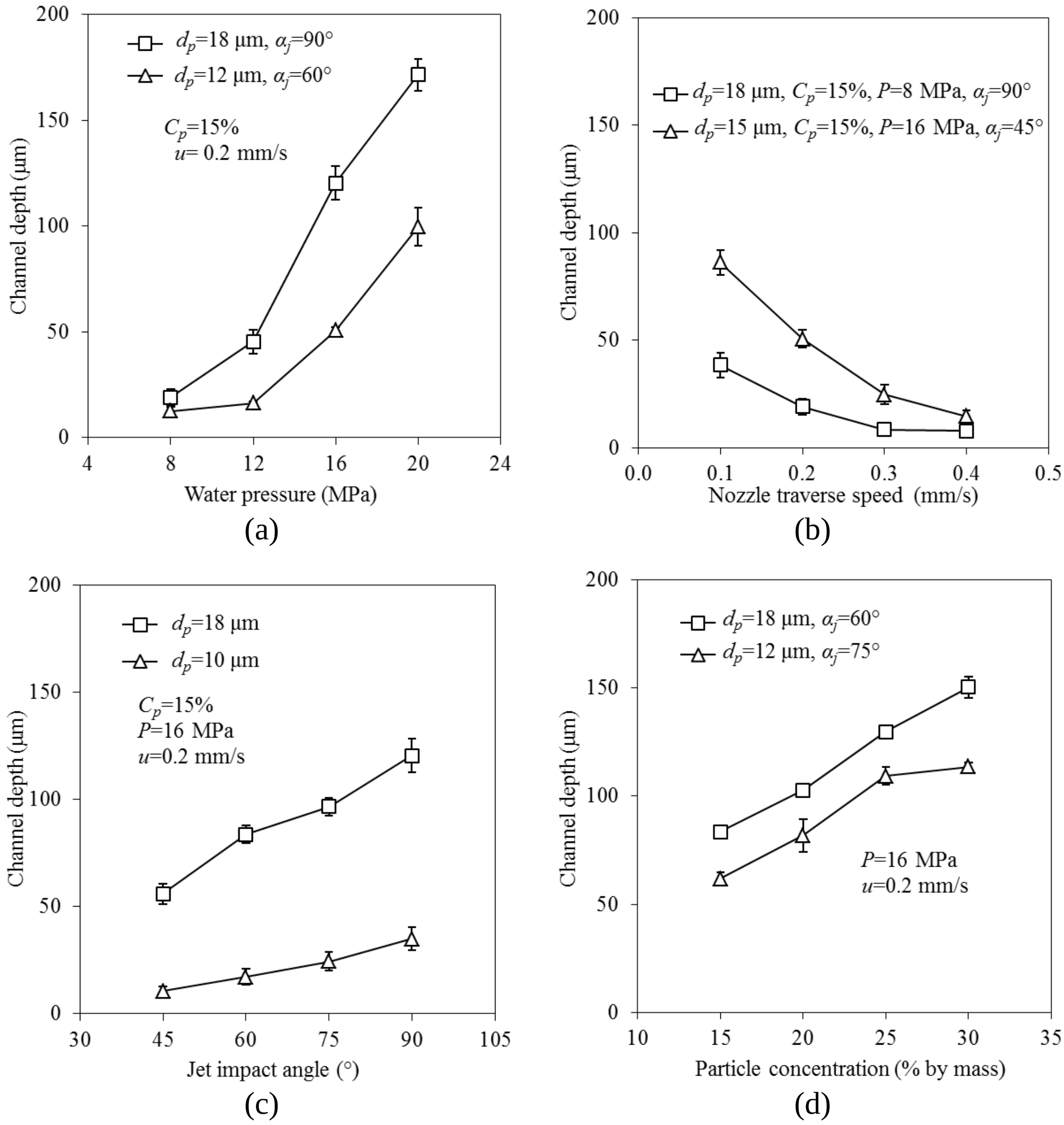

Fig. 3.6. Effect of process parameters on the channel depth (the scatter bars show standard deviation).

3.2.2.5 Effect of process parameters on top channel width

According to the ANOVA results in Table 3.3, the primary variables affecting the top channel width are, in order of significance from the most to the least, the nozzle traverse speed, particle size, water pressure and abrasive particle concentration. It is known that the effective jet diameter is a key factor determining the top channel width [30]. The increase in water pressure results in an increase in the dynamic pressure within the jet, which gives an increase in the effective jet diameter, hence opens a wider channel as shown in Fig. 3.7(a). Fig. 3.7(b) shows a negative effect of nozzle traverse speed on the top channel width. It may be explained that a fast nozzle traverse speed allows less abrasive particles to strike on a given area on the target, generating a narrow slot. It is noticed that the effect of jet impact angle is not significant with the P value larger than 0.05 as shown in Table 3.3. This may be attributed to the fact that the standoff distance was kept constant in the experiment, so that there was not any significant change to the interaction of the jet with the target surface and hence caused little change to the top channel width. By contrast, an increase in the particle size leads to a decrease in the top channel width, as shown in Fig. 3.7(c). This may be due to the fact that small particles with less energy have a greater tendency to follow the diverging water stream than larger ones, resulting in a larger particle jet divergence angle [114] and a wider channel. It can be seen from Fig. 3.7(d) that an increase in particle concentration results in a slight increase in the top channel width. This is because a higher particle concentration allows more particles to strike on the target and opens a wider slot. Further, it is interesting to note that the rate of increase of the top channel width reduces as abrasive particle concentration increases to beyond a certain value. This is possibly caused by the increased interference between particles as the particle concentration increases, which reduces the overall cutting efficiency of particles.

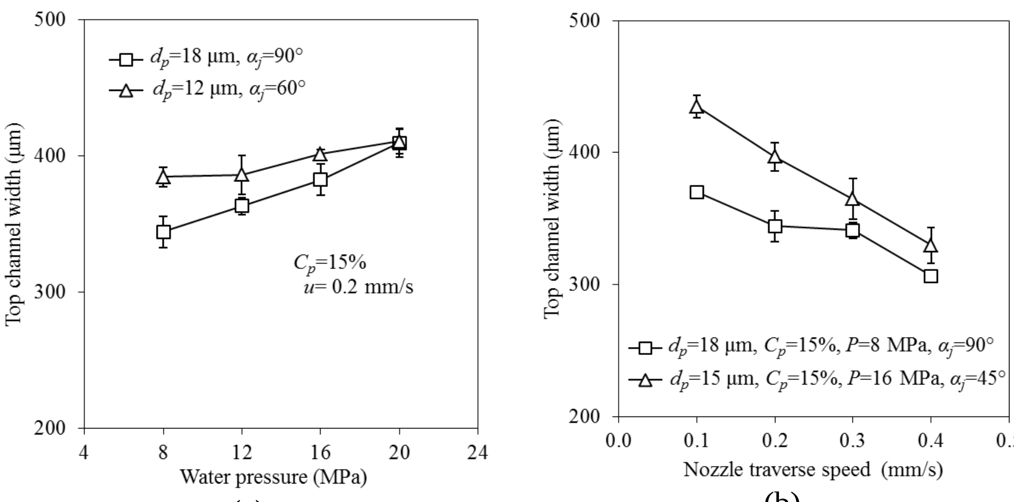

(a) (b)

Fig. 3.7, continued next page.

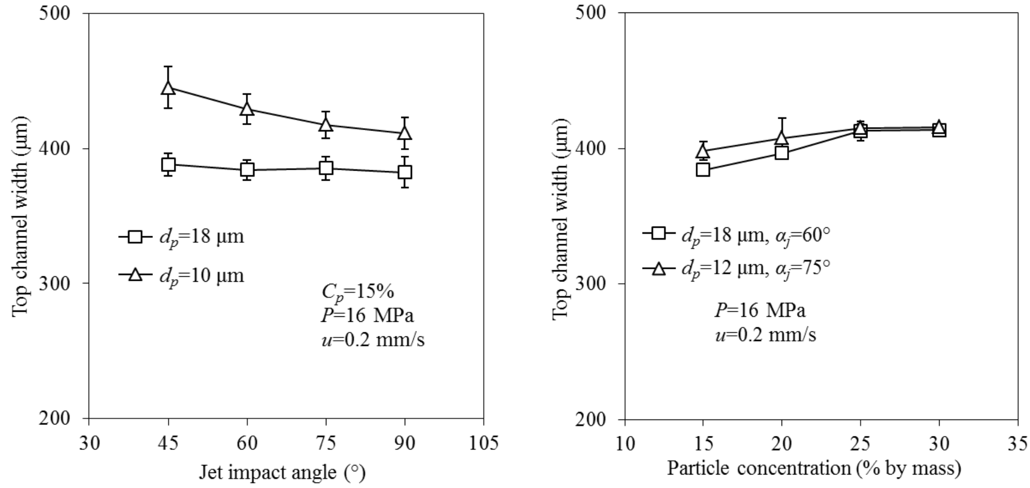

(c) (d)

Fig. 3.7. Effect of process parameters on the top channel width (the scatter bars show standard deviation).

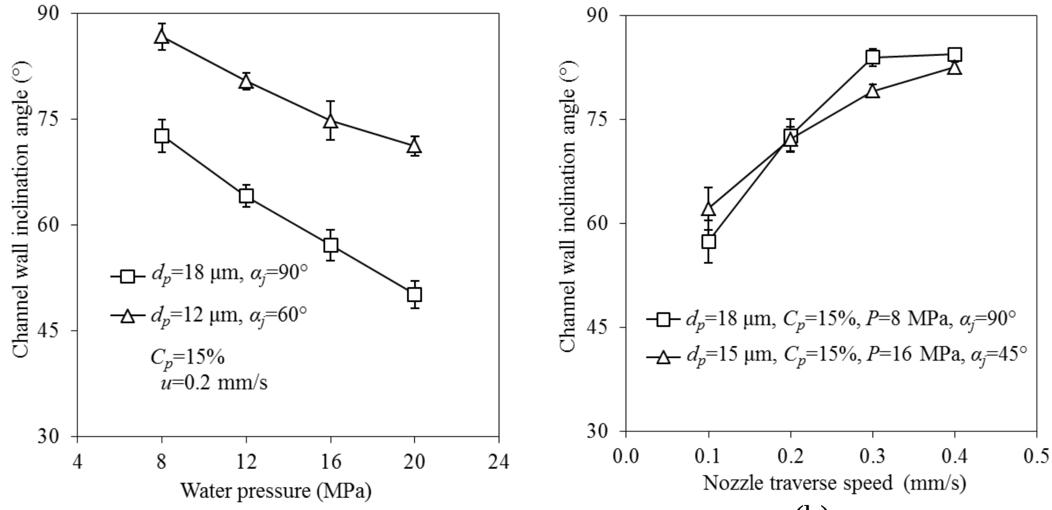

(a) (b)

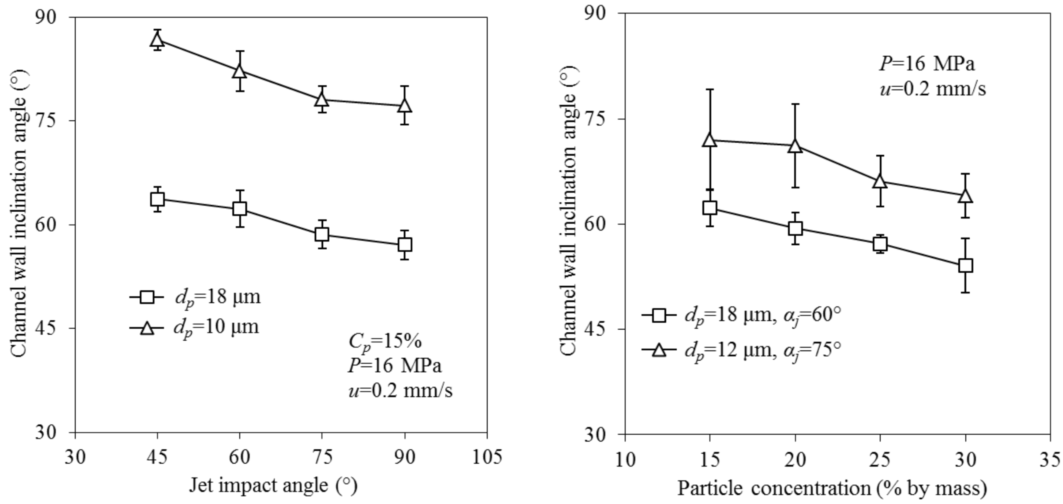

(c) (d)

Fig. 3.8. Effect of process parameters on the channel wall inclination angle (the scatter bars show standard deviation).

3.2.2.6 Effect of process parameters on channel wall inclination angle

Figs. 3.8(a) to (d) show that the channel wall inclination angle decreases with an increase in water pressure, particle size, particle concentration and jet impact angle, but increases with nozzle traverse speed. Unlike in ultrahigh pressure AWJ cutting, the secondary cutting process of the abrasive particles in the viscous flow in the lower pressure case plays a relatively significant role [7, 8, 73, 74]. By increasing the water pressure, an increase in kinetic energy in the viscous flow provides more energy to the turbulent flow which drives the abrasive particles to remove more materials from the lower part of the channel, thus decreasing the channel wall inclination angle as illustrated in Fig. 3.8(a). Fig. 3.8(b) shows that an increase in nozzle traverse speed increases the channel wall angle. A faster travelling jet reduces the interaction between the jet and target and the number of abrasive particles to impact a given area in the lower portion of the channel, which increases the channel wall inclination angle. As shown in Fig. 3.8(c), an increase in particle size and jet impact angle facilitates brittle mode erosion with more particle energy that enables an effective jet cutting action even at the low region of the channel, thus creating a steeper channel wall. Likewise, increasing the particle concentration allows a large number of energy-carrying particles to strike the target material and decreases the channel wall inclination angle.

3.3 Impact erosion by micro-particles

3.3.1 Experimental work

A specially designed nozzle assembly, as shown in Fig. 3.9, was used to conduct the micro-particle impact tests. Rather than using a high pressure water jet, a high pressure air jet was used so that the water damping effect on the impact was eliminated. The pressurised air was connected through a high frequency solenoid valve to an abrasive chamber where a very small amount of micro-particles (~0.1 mg) could be used and expelled out through a small nozzle. The solenoid valve was used to control the air on/off, and a relatively large nozzle with the diameter of 668 μm was used to facilitate the identification of individual particle impacts.

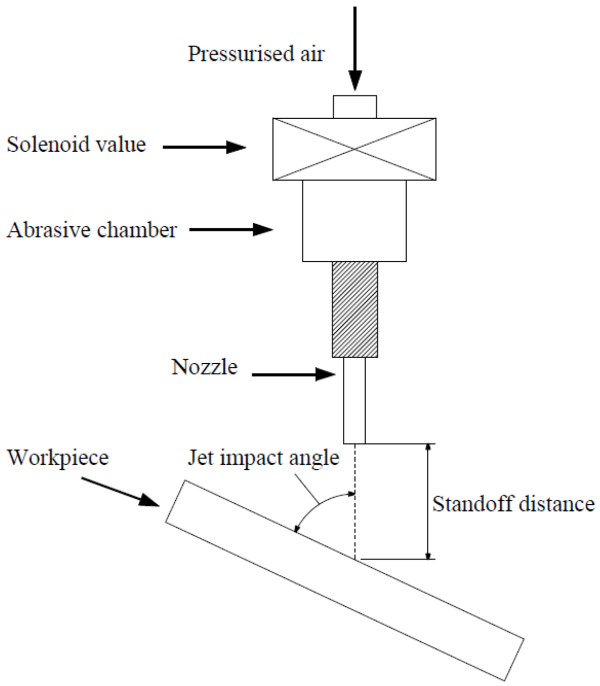

Fig. 3.9. Schematic of experimental setup.

As shown in Fig. 3.9, the jet impact angle could be varied by changing the angle of the specimen supporting frame. Based on the studies in the literature for abrasive air jet flow (e.g. [43, 115]), it was assumed that the impact angle of individual particles within a small radial distance from the jet centreline was equal to the jet impact angle. The jet or particle impact angles considered were 30°, 50°, 70° and 90°. The standoff distance was set at 10 mm for all the tests to allow the separation of the particles at the target surface.

Similar to the work in [91], it has been found that for a given air pressure with a 668 μm nozzle and within a 10 mm standoff distance, the variation of particle velocities within a 300 μm radial distance from the jet centreline is small. Thus, the particle velocity was calculated at 150 μm of jet radial distance using the model developed by Li et al. [43] as the nominal velocity for particles within a 300 μm radial distance. The particle velocity was varied by changing the air pressure, including 100, 130, 150 and 164 m/s, which corresponded to the air pressure of 0.21, 0.41, 0.62 and 0.83 MPa, respectively. Thus, the process variables and their levels for the experiment are given in Table 3.4.

Table 3.4. Variables used in the experiment.

Variables	Level 1	Level 2	Level 3	Level 4
Particle velocity, v_p (m/s)	100	130	150	164
Particle impact angle, α_p (°)	30	50	70	90

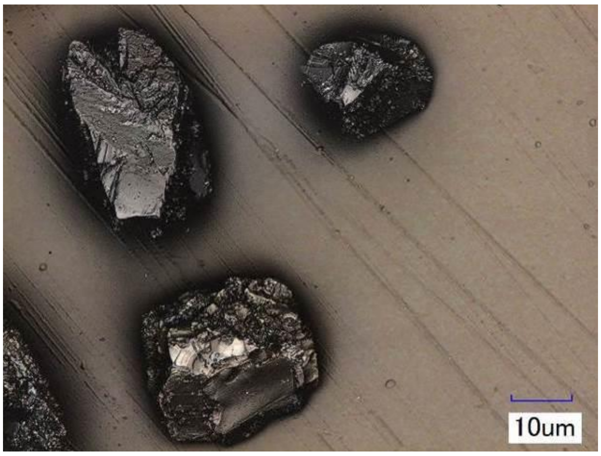

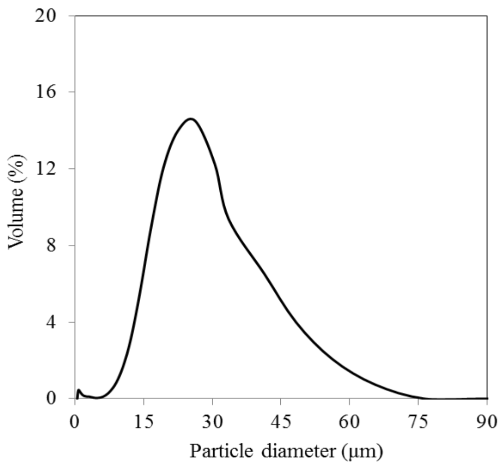

(a) (b)

Fig. 3.10. Alumnia abrasives used in the experiment: (a) general shapes of the particles, and (b) particle size distribution.

Alumina particles with an average diameter of 27 μm were used in the tests. It can be noticed from Fig. 3.10(a) that the particles are not really round. To quantitatively assess the particle shape, the average roundness of the particles (the ratio of the radius of curvature of the corner to the radius of the maximum inscribed circle in the plane of measurement) was obtained with the assistance of a Keyence Model VK-X200 3D laser microscope. This roundness gives information about how blunted or round the corners and edges of a particle are [116]. From 400 randomly selected particles, the average particle roundness has been found to be about 1.4, which indicates that most of the particles used in the experiment were not too far from a spherical ball of roundness 1. Furthermore, the particle size distribution was measured using a Malvern Mastersizer (from Malvern Instrument Ltd., UK). It can be seen in Fig. 3.10(b) that the particles with the diameter of 27 μm represent the largest proportion in volume, and those with the diameter ranging from 20 to 33 μm account for about 63% in volume.

With 4 levels of impact angle and 4 levels of particle velocity, 16 blasting test conditions were considered using a full factorial experimental design. By using a large nozzle diameter and small amount of abrasives, it was possible to differentiate individual particle impact sites with the assistance of a Keyence Model VK-X200 3D laser microscope. 20 impressions were identified for each test condition within a 300 μm radius from the impact centre, within which the particle velocities are almost constant. If required, repeated tests were performed. Thus, a total of 320 impressions were observed for analysis.

3.3.2 Results and Discussion

3.3.2.1 General observation of the eroded impressions

Fig. 3.11 shows a typical morphology of the eroded surface. Inside the jet impact zone, some large dimples generated by the impact of particles can be identified. Fig. 3.11(b) shows an enlarged view where three categories of the eroded impressions can be found, namely craters, scratches and micro-dents, similar to those formed on silicon [90, 91] as might be expected for brittle materials.

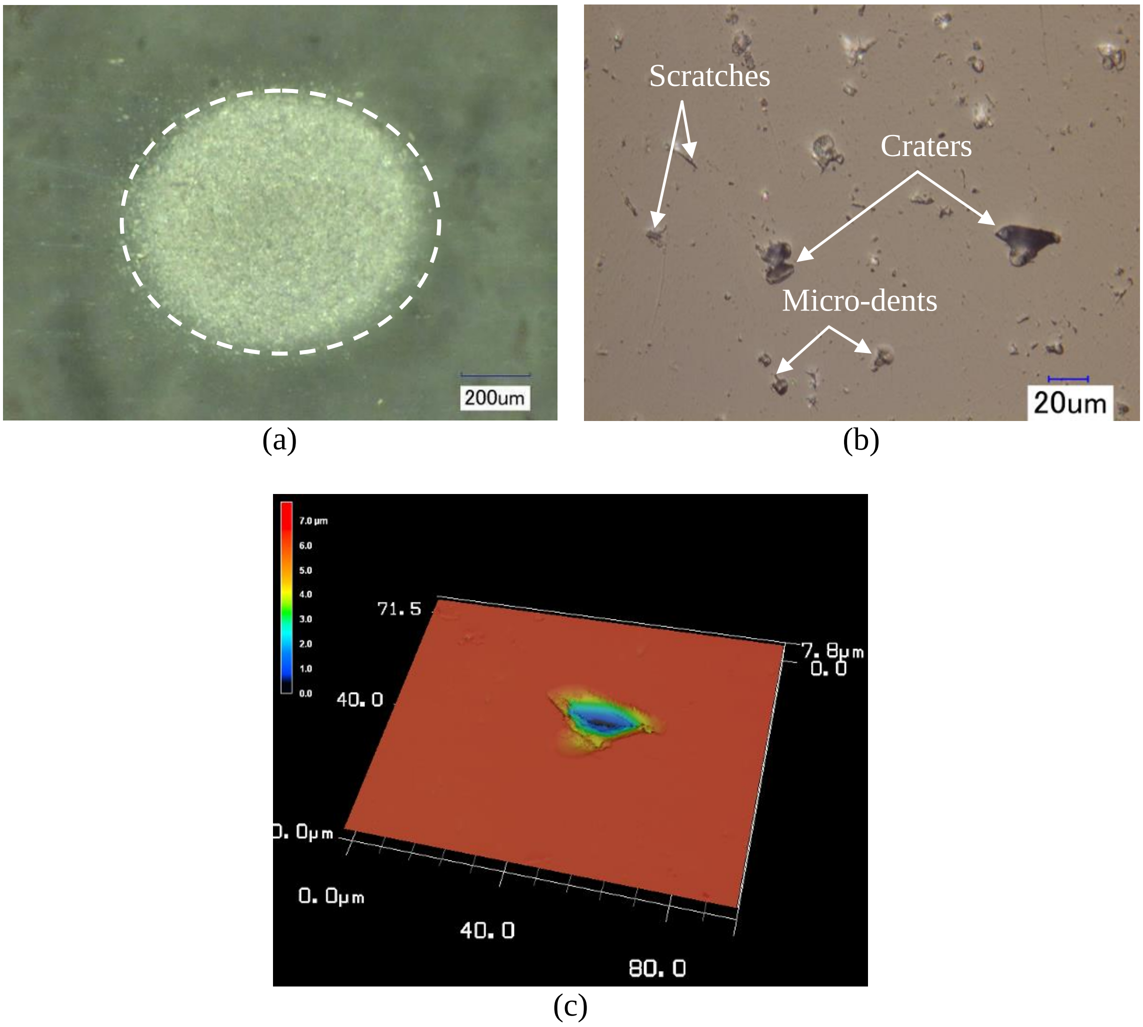

Fig. 3.11. Morphology of eroded dimples: (a) overall eroded impressions, (b) an enlarged partial view of (a), and (c) 3D image of a crater (d_p=27 μm, α_p=70°, and v_p=130 m/s).

3.3.2.2 Classification of eroded impressions

(i) Craters

Fig. 3.12 shows some typical craters formed by a single impact, which includes crashed zones, lateral cracks, radial cracks and conchoidal fractures. Crashed zones, which are roughly in a circular shape with matt surfaces, can be observed from Figs. 3.12(a) and (b). For brittle materials, like quartz crystal, when a particle collides with the target surface, the material under the impact is subjected to a relatively low hydrostatic pressure due to the relatively large contact area, and the tensile stresses around the impact zone start to initiate micro-cracks. Then the substrate material may be disintegrated by the merging of the micro-cracks and eventually removed in the form of fine chippings [90]. Fig. 3.12(b) shows a typical impression with both crashed zones and radial cracks. The pattern of a crashed zone is similar to that described above, but radial cracks are generated when the normal contact force exceeds a critical value [117]. In this type of impression, the radial cracks may run into the substrate, causing a decreased material strength that contributes to the material removal in the subsequent impacts.

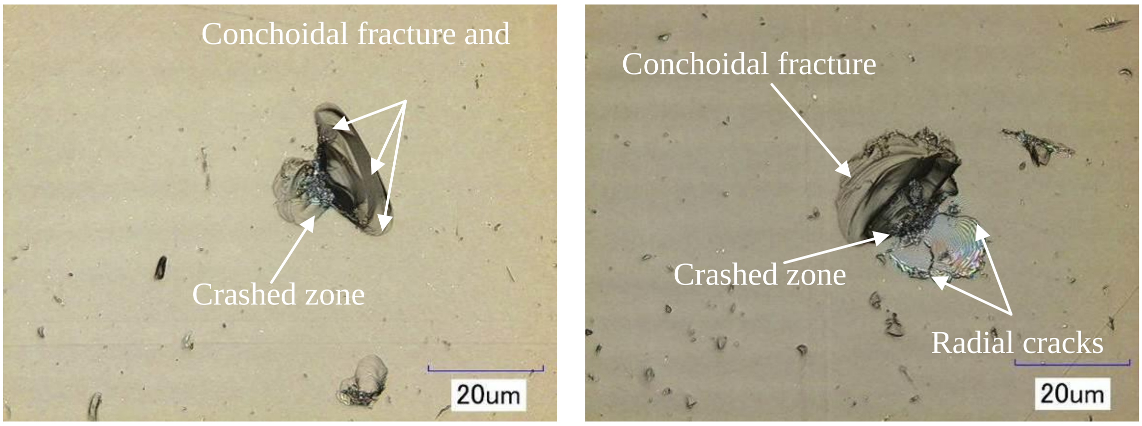

(a) (b)

Fig. 3.12. Impressions of craters: (a) crashed zone and conchoidal fracture, and (b) crashed zone, radial cracks and conchoidal fracture (d_p=27 μm, α_p=90°, and v_p=164 m/s).

A brittle fracture is always accompanied with lateral cracks when the impacting particles possess enough kinetic energy [118], as shown in Fig. 3.12(a). Figs. 3.12(a) and (b) show the craters with brittle fractures caused by the impacts at a high velocity and large impact angles. For quartz crystals, cleavage fracture is not commonly observed but fractures with conchoidal breakage of varying dimensions have commonly been found, and several types of conchoidal breakage patterns may be produced [119].

Ideally, the patterns are perfectly dish-shaped which appears as a depression on the target surface as shown in Fig. 3.12(a). An irregular conchoidal fracture with subsidiary step-like fractures on a curved portion is another common impression, as shown in Fig. 3.12(b). It is probably attributed to the large crack propagation and acoustical wave phenomena along the surface [119]. Around the conchoidal fracture, the crashed zone and radial cracks can be observed as well, but they contribute less to the material removal process than that of the large brittle-type fractures.

In general, when the kinetic energy of a particle is not enough to produce a lateral crack parallel to the target surface, a small crater that may include crashed zones and radial cracks is often generated by either plastic flow or subsurface micro-cracks. It is noted that large-scale craters are dominated by conchoidal fractures that are generated by the propagation of lateral cracks in the erosive process and are responsible for instant material removal. The extension of these conchoidal fractures is relatively large in the initial impact, so that the size of the craters is much bigger than the contact area.

(ii) Micro-dents and scratches

Some typical impressions of micro-dents and scratches are shown in Fig. 3.13. From Fig. 3.13(a), it can be noticed that the scale of the micro-dents is much smaller than the craters, and they were believed to be formed by the impacting particles with small kinetic energies that could not lead to large cracks and hence resulted in little material removal. These low energy-carrying particles are either in the low velocity area of the jet or because of the interference between particles and between particles and the nozzle wall that consumed the particle energy. By contrast, scratches were possibly formed by particles sliding or rolling over the target surface within the jet flow, where micro-cracks no longer intersect and run into the target surface, but propagate along the target surface as shown in Fig. 3.13(b). In this situation, only some radial cracks and a small-scale crashed zone are formed on the surface, which results in little material removal from the target. Therefore, these two types of impressions make a negligible contribution to material removal in the erosion process.

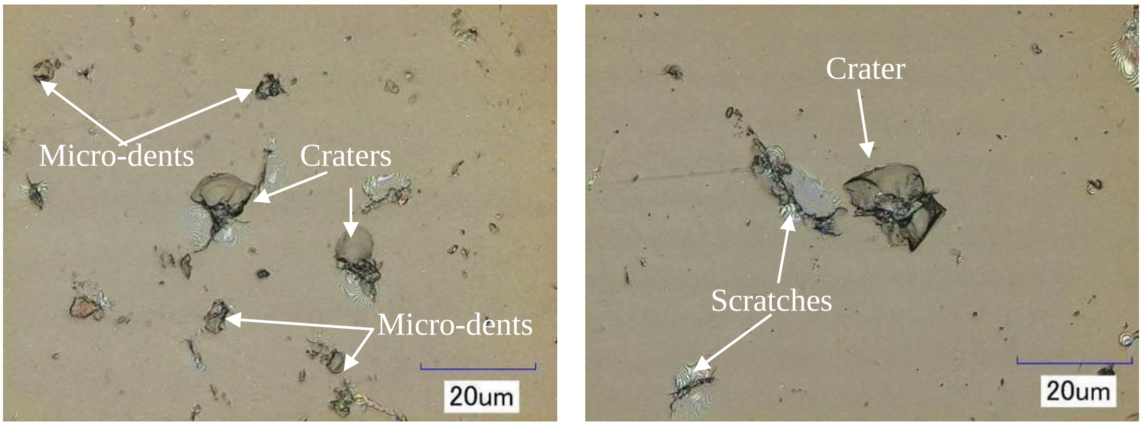

(a) (b)

Fig. 3.13. Impressions of: (a) micro-dents (d_p=27 μm, α_p=50°, and v_p=100 m/s) and (b) scratches (d_p=27 μm, α_p=50°, and v_p=150 m/s).

3.3.2.3 Effect of process parameters on crater volume

The effect of the process parameters, namely the particle impact velocity and impact angle, on the crater volume under the individual particle impacts are illustrated in Fig. 3.14. Due to the negligible contribution of micro-dents and scratches to the material removal, this analysis is based on the craters formed. The volume of the identified craters was measured using a Keyence Model VK-X200 3D laser measurement microscope with a 0.5 nm resolution. A typical image from the microscope is shown in Fig. 3.11(c). Each data point in Fig. 3.14 is in fact for the average of 20 crater volumes under identical impact conditions.

It can be seen from Fig. 3.14 that the crater volume by a particle impact increases significantly with an increase in the particle impact velocity. This effect is related to the increase of particle kinetic energy that is proportional to the square of particle velocity. At a higher velocity, the particle impact can generate a larger crater with an increased crater volume. Further, the effect of the particle impact angle, taken approximately from the jet impact angle, on the crater volume is also significant. The crater volume increases with an increase in the particle impact angle. This may be due to the fact that increasing particle impact angle facilitates brittle mode erosion to increase the crater volume for materials of a brittle nature [117, 118].

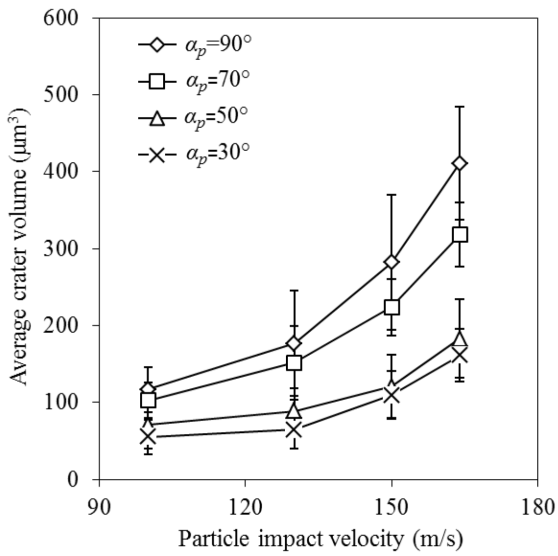

Fig. 3.14. Effect of process parameters on the average crater volume under individual particle impacts (the scatter bars show standard deviation).

3.4 Concluding remarks

In this chapter, experimental investigations have been carried out to understand the ASJ micro-channelling process and performance with respect to the process variables, and the mechanisms of impact erosion by a high velocity micro-particle on a quartz crystal.

A visualisation study has been carried out first on the machined channels. It has been found that the cross-section of the channels exhibits a U-shaped profile characterised by a wider entry at the top and the channel width reduces downwards, so that the channel walls incline by an angle. It has further been found that large wavy patterns are hardly discernible on the bottom surface of the channels. This was achieved by running off the shaker to eliminate the fluctuation of the slurry pressure during the process, and the use of a backward jet impact angle to facilitate the scanning action of the particles so as to increase the surface quality.

A statistical analysis of the effect of independent process parameters on the various channelling performance measures, i.e. channel bottom surface roughness, MRR, channel depth, top channel width and channel wall inclination angle, has been conducted. An ANOVA was performed first to identify the primary variables that significantly affect these channelling performance measures, followed by the study of how each micro-channelling performance measure changes with respect to the process parameters.

It has been shown that the bottom surface roughness increases with an increase in water pressure, particle size, jet impact angle and particle concentration, but decreases with an increase in nozzle traverse speed. The MRR and channel depth increase with the water pressure, jet impact angle, particle size and particle concentration, but decrease with an increase in nozzle traverse speed. The top channel width decreases with an increase in nozzle traverse speed, jet impact angle and particle size, but increases with water pressure and particle concentration. By contrast, the channel wall inclination angle increases with nozzle traverse speed, but decreases with an increase of all the other variables. Based on the conditions considered, a combination of high water pressure and particle concentration, large abrasive particles and jet impact angle, and low nozzle traverse speed is recommended to maximise the MRR and channel depth, while a combination of low water pressure and particle concentration, small abrasive particles and jet impact angle, and fast nozzle traverse speed is recommended to minimise the surface roughness, which is at the sacrifice of MRR and channel depth.

Impact erosion by individual micro-particles on a quartz crystal, in the conditions relevant to ASJ micro-machining, has been investigated to explore the erosion mechanisms. By analysing the morphology of eroded surfaces, three types of impressions similar to previous investigations on a brittle silicon material have been identified, namely craters, scratches and micro-dents. It has been found that large-scale craters caused by brittle conchoidal fractures are responsible for instant material removal and dominate the erosion process, while small-scale craters involving crashed zones and radial cracks are produced by plastic flow and subsurface micro-cracks that decrease the material strength. By contrast, the impacting particles with small kinetic energies produce micro-dents, while particle sliding or rolling on the target surface generate scratches. Thus, the crater-type impressions play a dominant role in the material erosion process, while micro-dents and scratches make only a minor contribution to material removal. The effect of particle impact velocity and impact angle on the material volume removed in the form of craters has finally been studied, which shows that an increase in either particle impact angle or velocity significantly increases the volume of the craters formed by individual particle impacts.

Chapter 4

Modelling of micro-channelling performance

4.1 Introduction

In the previous chapter, a study of the capabilities of the ASJ system in performing micro-channels on a quartz crystal was carried out. This study included a statistical analysis to identify the primary variables that significantly affect the various micro-channelling performance measures or quantities, i.e. channel bottom surface roughness, MRR, channel depth, top channel width and channel wall inclination angle, and an examination of the effect of process parameters on the micro-channelling performance measures. This study is able to provide a guideline for the selection of the process parameters. However, in order to effectively control and optimise the ASJ micro-channelling process on a quantitative and mathematical basis, it is essential to develop predictive models for the micro-channelling performance measures.

As reported in the Literature Review, a dimensional analysis approach which combines theoretical derivation and empirical study has been effectively used to develop predictive models for macro-scale AWJ cutting performance [57, 58, 69, 120, 121]. However, these models are not applicable to the current process which involves the use of a relatively low pressure ASJ and a smaller scale of material removal. In this chapter, predictive models for predicting micro-channelling performance, i.e. MRR, channel depth, top channel width and channel wall inclination angle, will be developed. The predictive models for the MRR and channel wall inclination angle will be developed using a dimensional analysis approach, while the predictive model for the top channel width will be established using an empirical approach due to the lack of understanding of complex channel formation mechanisms. Then, the model for predicting the maximum channel depth can be derived from the models for the MRR and top channel width. Finally, all the predictive models will be assessed both qualitatively and quantitatively by comparing predicted results from the models and the corresponding experimental data. For this purpose, additional ASJ micro-channelling tests will be performed to aid in the development of the predictive models.

4.2 Predictive models

4.2.1 Material removal rate

Material removal in ASJ micro-machining can be regarded as an accumulation of the material removed by individual particles. However, not all the particles inside an ASJ actually contribute to material removal; some may not even have sufficient energy to remove the material [3, 58]. An efficiency factor (ε_p) can be introduced to account for this effect, so that the MRR may be expressed as

$$MRR = \varepsilon_p n_p V_s = \varepsilon_p \frac{m_a}{m_p} V_s \qquad (4.1)$$

where n_p is the number of abrasive particles supplied per unit time, which can be found from the abrasive mass flow rate (m_a) and the average mass of a single particle (m_p), and V_s is the average volume of material removed by an impacting particle.

Assuming that the shape of abrasive particles is spherical and the particle size distribution is uniform, the average mass of a particle can be calculated from

$$m_p = \frac{\pi}{6} d_p^3 \rho_p \tag{4.2}$$

where d_p is the average particle diameter, and ρ_p is the abrasive particle density. Thus, Eq. (4.1) becomes

$$MRR = \varepsilon_p \frac{6m_a}{\pi d_p^3 \rho_p} V_s \tag{4.3}$$

It is now necessary to model material removal by a particle impact (V_s).

4.2.1.1 Material removed by a particle impact

As reported in the Literature Review, considerable research efforts have been made regarding the development of predictive models for the material removal volume by a particle impact [80, 122-125]. It has been found that dimensional analysis [65] is a powerful technique in relating engineering quantities to the influencing variables. As such, dimensional analysis is employed to model the material removed by a single particle impact in this study.

From the erosion theories [117], the impact-induced erosion may be considered as a function of the kinetic energy possessed by a particle, i.e., particle diameter (d_p), density (ρ_p) and particle velocity (v_p), impact angle (α_p) and the properties of the target material. The ratio of material hardness to material fracture toughness (H_m/K_{Ic}) has been found to provide a useful measure for the brittleness of brittle material [124] and hence its effect on the erosion, while Zeng and Kim [126] used the ratio of target material hardness to its modulus of elasticity (H_m/E_m) in their modeling work on the AWJ machining of ceramics and showed good results. To generalise these findings, material hardness, fracture toughness and modulus of elasticity are considered in this study. It may be noted that the quantities discussed above also account for the secondary material removal process by the viscous flow [7, 8, 73, 74], and that the particle velocity is related to water pressure. Thus, the material removal volume by a single particle impact may be expressed as

$$V_s = f(d_p, \rho_p, v_p, \alpha_p, K_{Ic}, H_m, E_m) \tag{4.4}$$

Table 4.1. Variables and their dimensions in deriving the material removal volume by a single particle impact (L, T and M denote length, time and mass, respectively).

Variables	Description	Dimensions
V_s	Material removal volume by single particle impact	L^3
d_p	Abrasive particle diameter	L
ρ_p	Abrasive particle density	ML^{-3}
v_p	Abrasive particle velocity	LT^{-1}
α_p	Abrasive particle impact angle	Dimensionless
K_{Ic}	Target material fracture toughness	$ML^{-0.5}T^{-2}$
H_m	Target material hardness	$ML^{-1}T^{-2}$
E_m	Target material elastic modulus	$ML^{-1}T^{-2}$

According to the dimensional analysis technique [65], all variables involved in a problem can be assembled into a small number of non-dimensional groups (called *Pi* groups), and the fundamental dimensions should be determined first through the analysis of the dimensions of variables involved in this study. Table 4.1 shows these variables and their respective dimensions.

Three fundamental dimensions have been identified from the eight variables in Eq. (4.4), namely length (L), mass (M) and time (T). Since the number of *Pi* groups that need to be generated can be determined by subtracting the total number of variables with the number of fundamental dimensions, five dimensionless *Pi* groups will be formed in this study. By selecting d_p, v_p and H_m as the three repeating variables, and noting that α_p is already a dimensionless variable, the following *Pi* groups can be formed:

$$\pi_1 = \frac{V_s}{d_p^3} \tag{4.5}$$

$$\pi_2 = \frac{E_m}{H_m} \tag{4.6}$$

$$\pi_3 = \frac{K_{Ic}}{d_p^{0.5} H_m} \tag{4.7}$$

$$\pi_4 = \alpha_p \tag{4.8}$$

$$\pi_5 = \frac{\rho_p v_p^2}{H_m} \tag{4.9}$$

It is noted that π_1 represents a relationship between the volume removed during an impact to the volume of the impacting particle, bearing in mind that the volume of a particle increases with particle size. π_2 represents the erosion by plastic deformation during an impact event [8]. It follows that for the portion of material removal caused by the ductile mode erosion, a plastic deformation model may be used to determine material removal. The factor which determines the erosion by plastic deformation is whether micro-cutting or micro-ploughing of the material takes place, and according to Hutchings [117], the ratio E_m/H_m provides a good indicator for this. π_3 can be considered as the erosion by the brittle fracture during an impact event [127]. This interpretation follows from the fact that K_{Ic}/H_m is a measure of the relative resistance of a target material to fracture, i.e., the higher the value of K_{Ic}/H_m, the more resistant the target will be to fracture [128]. The parameter, $K_{Ic}/(d_p^{0.5}H_m)$, can be regarded as representing the erosion by the brittle fracture incorporating the impact (or particle) size effect, or the erosion per unit area. π_4 represents the effect of particle impact angle on the erosion of brittle materials. π_5 represents the ratio of the particle energy density (proportional to $\rho_p v_p^2$ in value for a given particle size) to the target hardness H_m which can be considered as a deformation energy density [127].

Based on the dimensional analysis technique, the functional relation between these five *Pi* groups is given by

$$\pi_1 = f(\pi_2, \pi_3, \pi_4, \pi_5) \tag{4.10}$$

The above mentioned relation is yet to be mathematically determined. According to the dimensional analysis technique, a non-dimensional quantity is proportional to the product of other dimensionless groups raised to a rational power. Thus, by applying the power-law formulation to Eq. (4.10), the volume of material removal by a particle can be given by

$$V_s = k_1 d_p^3 (\frac{E_m}{H_m})^{a_1} \left(\frac{K_{Ic}}{d_p^{0.5} H_m} \right)^{a_2} \alpha_p^{a_3} \left(\frac{\rho_p v_p^2}{H_m} \right)^{a_4} \tag{4.11}$$

where k_1, a_1, a_2, a_3 and a_4 are dimensionless coefficients. In this equation, the particle impact angle (α_p) and the abrasive particle velocity (v_p) need to each be determined.

4.2.1.2 Particle impact angle

It has been found from the previous studies [53, 69, 120, 121] that the particle impact angle in AWJ machining primarily depends on the characteristics of the abrasive particles within the fluid flow that carries them as well as the geometrical characteristics of the target material surface. Due to the large number of variables involved, it is difficult to develop mathematical models to account for every particle, so that the average particle impact angle is considered using the dimensional analysis approach.

Similar to AWJ meso-machining, in ASJ micro-machining the particle impact angle is considered to be affected by the dynamic characteristics of the particles in the slurry jet at the point of impact, and the geometrical characteristics of the target material surface being eroded. All these effects can be attributed to the process parameters, i.e. particle diameter (d_p), particle density (ρ_p), particle velocity (v_p) and abrasive concentration (C_p) in the jet, and the material properties represented by fracture toughness (K_{Ic}), hardness (H_m) and modulus of elasticity (E_m), as discussed earlier, as well as the process parameters such as the jet impact angle (α_j) and nozzle traverse speed (u) [23, 111]. Consequently, the average particle impact angle (α_p) can be expressed as

$$\alpha_p = f\left(d_p, \rho_p, v_p, K_{Ic}, H_m, E_m, C_p, \alpha_j, u\right) \tag{4.12}$$

The dimensions of all variables involved in Eq. (4.12) are given in Table 4.2, where L, M and T are the fundamental variables for length, mass and time, respectively.

Table 4.2. Variables and their dimensions in deriving the average abrasive particle impact angle.

Variables	Description	Dimensions
α_p	Abrasive particle impact angle	Dimensionless
d_p	Abrasive particle diameter	L
ρ_p	Abrasive particle density	ML^{-3}
v_p	Abrasive particle impact velocity	LT^{-1}
K_{Ic}	Target material fracture toughness	$ML^{-0.5}T^{-2}$
H_m	Target material hardness	$ML^{-1}T^{-2}$
E_m	Target material elastic modulus	$ML^{-1}T^{-2}$
C_p	Abrasive particle concentration by mass	Dimensionless
α_j	Jet impact angle	Dimensionless
u	Nozzle traverse speed	LT^{-1}

Similarly, d_p, v_p and H_m are selected as the repeating variables in the dimensional analysis, and the following seven *Pi* groups are formed, noting that C_p, α_j and α_p are already dimensionless terms:

$$\pi_1 = \alpha_p \tag{4.13}$$

$$\pi_2 = \frac{E_m}{H_m} \tag{4.14}$$

$$\pi_3 = \frac{K_{Ic}}{d_p^{0.5} H_m} \tag{4.15}$$

$$\pi_4 = \alpha_j \tag{4.16}$$

$$\pi_5 = \frac{\rho_p v_p^2}{H_m} \tag{4.17}$$

$$\pi_6 = C_p \tag{4.18}$$

$$\pi_7 = \frac{u}{v_p} \tag{4.19}$$

The physical meanings of some of the *Pi* groups have been given before. It may be noted that π_4 represents the effect of jet impact angle on the particle impact angle during the machining process, π_6 represents the effect of abrasive particle concentration on the interferences between the impacting particles involved in the jet and hence, the actual particle impact angle, and π_7 represents the combined effects of nozzle traverse speed and particle impact velocity on the resultant particle impact angle. Similar to the preceding analysis, the relationship between the seven *Pi* groups can be given by the following equation.

$$\pi_1 = f\left(\pi_2, \pi_3, \pi_4, \pi_5, \pi_6, \pi_7\right) \tag{4.20}$$

By using the power-law formulation, the average particle impact angle (α_p) can be given by

$$\alpha_p = k_2 C_p^{b_1} \alpha_j^{b_2} \left(\frac{E_m}{H_m}\right)^{b_3} \left(\frac{K_{Ic}}{d_p^{0.5} H_m}\right)^{b_4} \left(\frac{u}{v_p}\right)^{b_5} \left(\frac{\rho_p v_p^2}{H_m}\right)^{b_6} \tag{4.21}$$

where k_2, b_1, b_2, b_3, b_4, b_5 and b_6 are coefficients.

4.2.1.3 Particle velocity

Particles in ASJ are premixed thoroughly before the micro-ASJ is formed, so that particles are assumed to be distributed uniformly in the slurry and possess the same velocity as the surrounding water at the nozzle exit. Within a small standoff distance, it is believed that the velocity variation from the nozzle exit to the target surface is negligible [73]. Thus, the slurry jet velocity (v_j) and the abrasive particle velocity (v_p) can be obtained from Bernoulli's equation, i.e.

$$v_p = v_j = \gamma\sqrt{\frac{2P}{\rho_s}} \tag{4.22}$$

where P is the water pressure, ρ_s is the mixed slurry density, and γ is the overall coefficient of discharge that characterises the momentum loss due to wall friction, fluid flow disturbances and compressibility of water [4]. With a given abrasive particle concentration (C_p), using the law of mass conservation and Archimedes law [72], the slurry density can be given by

$$\rho_s = \frac{\rho_p \rho_f}{C_p \rho_f + \rho_p (1 - C_p)} \tag{4.23}$$

where ρ_f is the fluid density, which is the water density in this study.

4.2.1.4 Squeeze film effect

A thin layer of water, called squeeze film, forms in the stagnation zone on the target surface and acts as a damping layer to resist the ASJ impacting the target.

It has been found [129-132] that the squeeze film intervening between an erodent particle and a target surface leads to a significant retardation of particle velocity immediately before impacting the target. In order to account for this effect, it is suggested that a correction factor F, which is dependent on the particle Reynolds number in the slurry jet and particle size, density and velocity, be applied to the particle impact velocity calculated from the potential flow analysis, so that the particle impact velocity (v_i) passing through the squeezing film can be found from

$$v_i = Fv_p = F\gamma\sqrt{\frac{2P}{\rho_s}} \tag{4.24}$$

4.2.1.5 Model for material removal rate

With a given particle concentration (C_p), slurry jet velocity (v_j) and nozzle inner diameter (D), the abrasive mass flow rate (m_a) can be expressed as

$$m_a = \rho_s C_p v_j \frac{\pi D^2}{4} \tag{4.25}$$

Consequently, substituting Eqs. (4.11), (4.21), (4.24) and (4.25) into Eq. (4.3) results in

$$MRR = k_3\left(\frac{D^2 P^{0.5}\rho_s^{0.5}}{\rho_p}\right)C_p^{c_1}\alpha_j^{c_2}\left(\frac{K_{Ic}}{d_p^{0.5}H_m}\right)^{c_3}\left(\frac{E_m}{H_m}\right)^{c_4}\left(\frac{u\rho_s^{0.5}}{P^{0.5}F}\right)^{c_5}\left(\frac{\rho_p PF^2}{H_m\rho_s}\right)^{c_6} \tag{4.26}$$

where k_3, c_1, c_2, c_3, c_4, c_5 and c_6 are introduced to generalise all coefficients in the previous equations and can be determined by experimental data.

4.2.2 Channel wall inclination angle

Base on previous studies [29, 30, 34, 56], the distribution of the particle velocity at the jet radial direction is believed to be a significant factor that affects the formation of the channel walls in the AWJ cutting process. At a given cross-section downstream from the nozzle exit, the particle velocity decreases from the centre to the rim of the jet, which will result in a different material erosion rate in the jet radial direction when these particles impact the target surface, and eventually, generating a channel wall with an inclination angle. Moreover, in order to remove material from the target, the kinetic energy carried by the particle must be higher than the destructive energy required to erode the target material; in the other words, the properties of the target material play an important role in the formation of the channel walls. As such, the trajectory of the particles inside an AWJ, the kinetic energy possessed by the particles and the target material properties should be considered in developing the predictive model for the channel wall inclination. As many factors need to be taken into account, the dimensional analysis technique will be used to relate these influencing factors to the channel wall inclination angle.

In the ASJ micro-channelling process, the trajectory of a particle is associated with the characteristics of the fluid flow carrying it, which can be represented by the abrasive particle concentration (C_p), abrasive particle density (ρ_p) and diameter (d_p), the nozzle inner diameter (D) and the jet impact angle (α_j). The kinetic energy carried by the abrasive particle is represented by the abrasive particle mass (m_p) (or alternatively particle density (ρ_p) and diameter (d_p)) and the abrasive particle velocity (v_i). The target material properties are represented by the material fracture toughness (K_{Ic}), hardness (H_m) and elastic modulus (E_m), as discussed earlier. The jet exposure time on the target material also needs to be taken into account, which is represented by the nozzle traverse speed (u). Thus, the channel wall inclination angle (θ) can be expressed in a general form as

$$\theta = f\left(d_p, \rho_p, v_i, D, K_{Ic}, H_m, E_m, C_p, \alpha_j, u\right) \tag{4.27}$$

All variables involved in above equation are listed in Table 4.3 with their dimensions.

Table 4.3. Variables and their dimensions in deriving the channel wall inclination angle.

Variables	Description	Dimensions
θ	Channel wall inclination angle	Dimensionless
d_p	Abrasive particle diameter	L
ρ_p	Abrasive particle density	ML^{-3}
v_i	Abrasive particle impact velocity	LT^{-1}
K_{Ic}	Target material fracture toughness	$ML^{-0.5}T^{-2}$
C_p	Abrasive particle concentration by mass	Dimensionless
α_j	Jet impact angle	Dimensionless
u	Nozzle traverse speed	LT^{-1}
D	Nozzle inner diameter	L
H_m	Target material hardness	$ML^{-1}T^{-2}$
E_m	Target material elastic modulus	$ML^{-1}T^{-2}$

By selecting d_p, v_i and H_m as the repeating variables and noting that C_p and α_j are already dimensionless terms, eight *Pi* groups can be generated as follows.

$$\pi_1 = \theta \tag{4.28}$$

$$\pi_2 = \frac{E_m}{H_m} \tag{4.29}$$

$$\pi_3 = \frac{K_{Ic}}{d_p^{0.5} H_m} \tag{4.30}$$

$$\pi_4 = \alpha_j \tag{4.31}$$

$$\pi_5 = \frac{\rho_p v_i^2}{H_m} \tag{4.32}$$

$$\pi_6 = C_p \tag{4.33}$$

$$\pi_7 = \frac{u}{v_i} \tag{4.34}$$

$$\pi_8 = \frac{D}{d_p} \tag{4.35}$$

The physical meanings of some of the *Pi* groups have been given before. It may be noted that π_8 represents the ratio of nozzle inner diameter to the particle size, which can be considered as the effect of the distribution of impacting particles involved in the jet on the formation of channel walls. Again, the relationship between the eight *Pi* groups can be given by the following equation.

$$\pi_1 = f\left(\pi_2, \pi_3, \pi_4, \pi_5, \pi_6, \pi_7, \pi_8\right) \tag{4.36}$$

Thus, by using the power-law formulation and noting that v_i can be found from Eq. (4.24), the channel wall inclination angle (θ) can be given by

$$\theta = k_4 C_p^{d_1} \alpha_j^{d_2} \left(\frac{K_{Ic}}{d_p^{0.5} H_m}\right)^{d_3} \left(\frac{E_m}{H_m}\right)^{d_4} \left(\frac{u\rho_s^{0.5}}{P^{0.5} F}\right)^{d_5} \left(\frac{\rho_p P F^2}{H_m \rho_s}\right)^{d_6} \left(\frac{D}{d_p}\right)^{d_7} \tag{4.37}$$

where k_4, d_1, d_2, d_3, d_4, d_5, d_6 and d_7 are introduced to generalise all coefficients in the previous equations and can be determined experimentally.

4.2.3 Top channel width

The top channel width will be determined from a regression analysis using the experimental data. As discussed in Section 3.2.2.5, abrasive particle size (d_p), water pressure (P), nozzle traverse speed (u) and abrasive particle concentration (C_p) are the primary variables affecting the top channel width, while the jet impact angle has little effect on the top channel width, such that the factor of jet impact angle is not considered in this model.

The regression analysis was conducted using the SPSS software. Three commonly used regression models, namely the linear model, power model and quadratic model, were tested for the top channel width at a confidence interval of 95% using the experimental data obtained from 92 tests as stated in Chapter 3. A comparison of the coefficients of determination (R^2) was carried out from the preliminary regression analysis in order to select the best model. As the quadratic model gives the highest R^2 values of 82%, it can best describe the variation in the top channel width with respect to the process parameters. Consequently, the regression model for the top channel width is developed based on a quadratic model.

As there are four process variables involved in the modelling process, the resultant quadratic equation can be made up of 15 estimated items. However, not all the estimated items significantly affect the developed model, thus the inclusion of all 15 estimated items in the model may result in a too complicated form for practical use. In order to simplify the model, the backward elimination procedure in SPSS software was employed to eliminate those estimated items that have only a minor or negligible effect on the top channel width. Following the model simplification process, the final form of the regression model for the top channel width (w_t) is given by

$$\begin{aligned} w_t &= 389.71 - 1838.93C_p^2 + 27.71d_pC_p - 24.63C_pP + 594.94C_pu - 9.12d_p \\ &\quad + 749.27C_p + 7.39P - 339.51u \end{aligned} \tag{4.38}$$

where the units of each parameter are given in the Nomenclature. The assessment of the model will be given later in the Chapter.

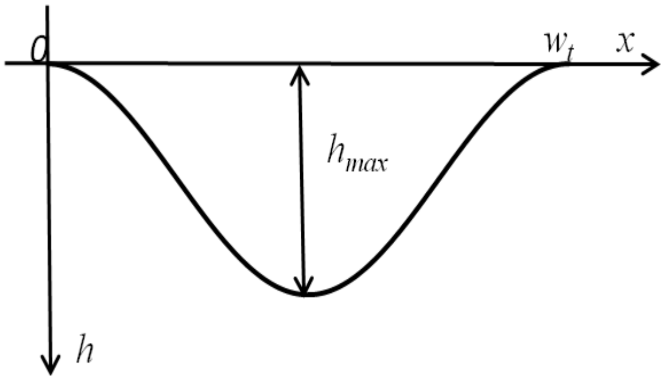

Fig. 4.1. Schematic of the cross-sectional profile.

4.2.4 Channel depth

Fig. 3.3(c) shows that the cross-sectional profile of a machined-channel is similar to a cosine function curve, such that the channel depth (h) at any position can be approximated by a cosine function shown in Fig. 4.1, i.e.

$$h(x) = \frac{h_{\max}}{2}\left[1 - \cos\left(\frac{2\pi}{w_t}x\right)\right], x \in [0, w_t] \tag{4.39}$$

where h_{max} is the maximum channel depth and w_t is the top channel width. When $x=w_t/2$, $h=h_{max}$.

Thus, the total area (S_c) between the curve of $h(x)$ and the x axis is expressed by

$$S_c = \int_0^{w_t} h(x)dx = \int_0^{w_t} \frac{h_{\max}}{2}\left[1-\cos\left(\frac{2\pi}{w_t}x\right)\right]dx = \frac{h_{\max}}{2}w_t \tag{4.40}$$

By ignoring the profile variation along the traverse direction, the MRR is given by

$$MRR = S_c\, u \tag{4.41}$$

Consequently, by substituting Eq. (4.40) into Eq. (4.41), the maximum channel depth can be given by

$$h_{\max} = \frac{2MRR}{w_t u} \tag{4.42}$$

where the top channel width (w_t) can be determined from Eq. (4.38), and MRR can be found from Eq. (4.26).

4.3 Model assessment

Before the developed models can be used for predicting the micro-channelling performance measures, the coefficients in each predictive model need to be determined. For this purpose, the experimental data from the 92 tests as stated in Chapter 3 were employed to find the coefficients in Eqs. (4.26) and (4.37) by regression analysis at a 95% confidence level. Thus, Eq. (4.26) for the experimental conditions used in this study becomes

$$MRR = 8.65\times10^{-11}\left(\frac{D^2P^{0.5}\rho_s^{0.5}}{\rho_p}\right)C_p^{0.761}\alpha_j^{1.028}\left(\frac{K_{Ic}}{d_p^{0.5}H_m}\right)^{-4.395}\left(\frac{u\rho_s^{0.5}}{P^{0.5}F}\right)^{-0.27}\left(\frac{\rho_p PF^2}{H_m\rho_s}\right)^{1.357} \quad (4.43)$$

Substituting the constant values for nozzle inner diameter, material properties and abrasive properties relevant to this study as stated in Chapter 3 into Eq. (4.43) gives

$$MRR = 1.79\times10^{-9}\,\frac{P^{1.992}C_p^{0.761}\alpha_j^{1.028}d_p^{2.196}F^{2.984}}{\rho_s^{1.127}u^{0.27}} \quad (4.44)$$

where the units of the parameter are given in the Nomenclature.

Similarly, the coefficients in the model for channel wall inclination angle (θ) can be given by

$$\theta = 4.22\times10^3 C_p^{-0.221}\alpha_j^{-0.14}\left(\frac{K_{Ic}}{d_p^{0.5}H_m}\right)^{0.855}\left(\frac{u\rho_s^{0.5}}{P^{0.5}F}\right)^{0.255}\left(\frac{\rho_p PF^2}{H_m\rho_s}\right)^{-0.144} \quad (4.45)$$

By substituting the constant values for nozzle inner diameter, material properties and abrasive properties relevant to this study as stated in Chapter 3 into Eq. (4.45), Eq. (4.45) becomes

$$\theta = 708.5 \frac{\rho_s^{0.272} u^{0.255}}{P^{0.272} C_p^{0.221} \alpha_j^{0.14} d_p^{0.428} F^{0.543}} \tag{4.46}$$

where the units of each parameter are given in the Nomenclature.

Thus, the maximum channel depth can be calculated by substituting the Eqs. (4.38) and (4.44) into the Eq. (4.42).

In order to assess the developed models, an additional 30 model verification tests were conducted, and the experimental data was compared with the model predicted MRR, maximum channel depth, top channel width and channel wall inclination angle under the corresponding conditions to assess the models.

4.3.1 Qualitative assessment

Comparisons between the predicted and experimental results in terms of MRR, channel wall inclination angle, top channel width and maximum channel depth are illustrated in Figs. 4.2 to 4.5, respectively, where the lines represent the predicted values while the symbols are for the experimental data. In general, it can be seen from these figures that model predictions for the micro-channelling performance agree well with the experimental data and correctly represent the trends of these four performance measures with respect to the various process parameters.

The plausibility of the predictive model for MRR is examined by analysing the predicted trends with respect to the process parameters. As shown in Figs. 4.2(a) to (d), the predicted MRR increases with an increase in water pressure, jet impact angle, abrasive particle size and the particle concentration. These are in line with the experimental findings given in Chapter 3. This can possibly be attributed to an increase in kinetic energy carried by individual particles, which enables a particle to penetrate deeper into the workpiece, resulting in greater material removal. This can be achieved by increasing the water pressure, which increases the particle velocity and hence the kinetic energy, increasing the particle concentration, which increases the amount of solid-solid interaction and thus the MRR, and using larger particles, which results in a smaller deceleration rate after the particle exits from the nozzle so that the particles have more energy to impact the material. Likewise, increasing the jet impact angle facilitates brittle mode erosion for increasing the removal rate of brittle materials [63, 112, 113]. In addition, it is noticed from Fig. 4.2(e) that an increase in nozzle traverse speed results in a decrease in MRR, due to the thin water layer which forms on the target surface that causes a shielding effect on the cutting efficiency of the impacting particles, this being particularly so at higher nozzle traverse speeds, so that the MRR shows a declining trend with an increase in the nozzle traverse speed.

The comparison of the predicted channel wall inclination angles with the corresponding experimental data is shown in Fig. 4.3. It shows that the predicted channel wall inclination angle decreases with an increase in water pressure, particle size, particle concentration and jet impact angle, but increases with an increase in nozzle traverse speed. These are again consistent with the experimental findings presented in Chapter 3. Based on previous studies [7, 8, 73, 74], it has been found that the secondary cutting process of the abrasive particles in the viscous flow in the lower pressure case plays a relatively significant role in the material removal process. Increasing water pressure can result in an increase in the kinetic energy of the viscous flow which provides more

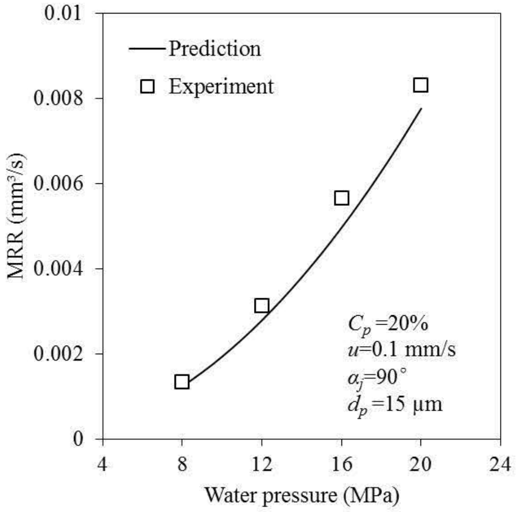

(a)

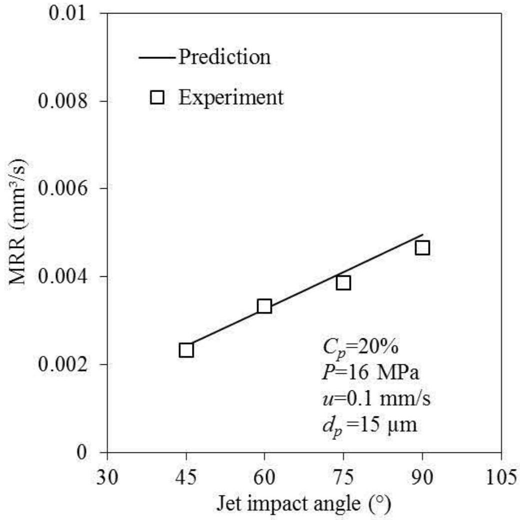

(b)

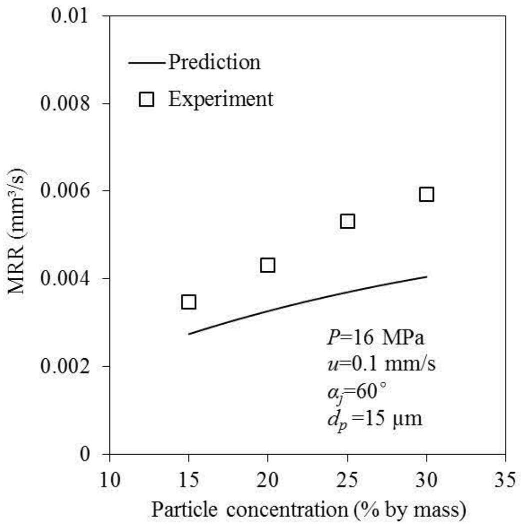

(c)

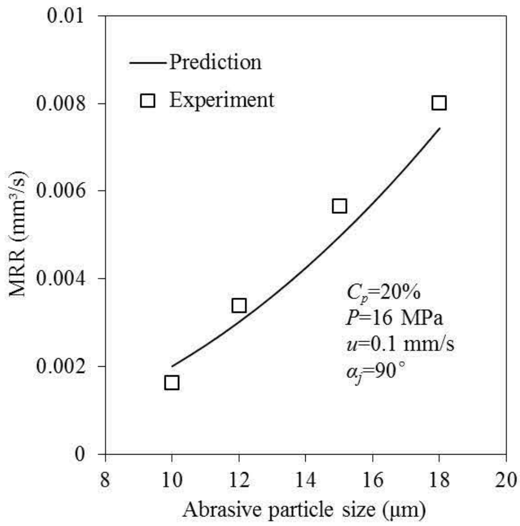

(d)

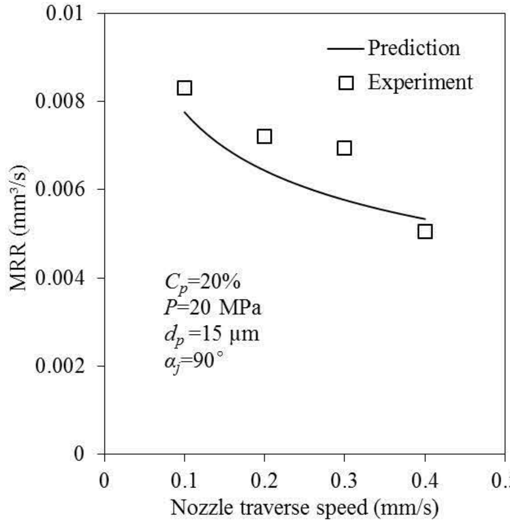

(e)

Fig. 4.2. Comparison between predicted and experimental MRR.

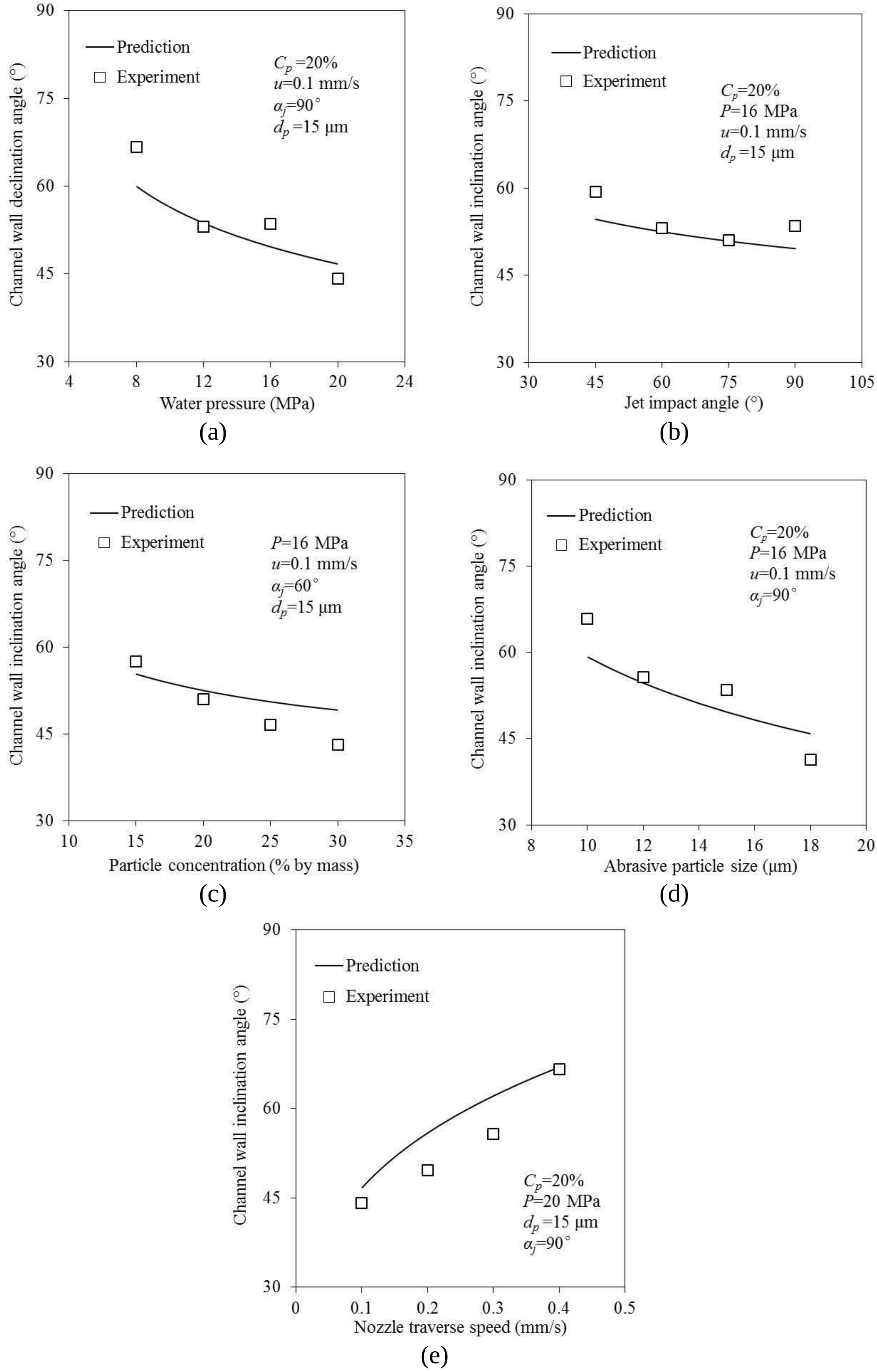

Fig. 4.3. Comparison between predicted and experimental channel wall inclination angles.

energy to the abrasive particles involved in the turbulent region of the flow that can remove more materials from the lower part of the channel before exiting the cutting zone, thus decreasing the channel wall inclination angle as illustrated in Fig. 4.3(a). As shown in Figs. 4.3(b) and (d), an increase in particle size and jet impact angle facilitates brittle mode erosion that enables an effective jet cutting action even at the low part of the channel, thus creating a steeper channel wall. Likewise, Figs. 4.3(c) and (e) indicates that decreasing the particle concentration or increasing the nozzle traverse speed reduces the interaction between the jet and target and the number of abrasive particles to impact a given area in the lower portion of the channel, which in turn increases the channel wall inclination angle.

A comparison between the model predicted and experimental top channel widths is illustrated in Fig. 4.4. As pointed out in the Literature Review, the top channel width is primarily affected by the effective jet diameter [30], and increasing water pressure results in an increase in the dynamic pressure within the jet which increases the effective jet diameter, and hence generates a wider channel as shown in Fig. 4.4(a). It can be seen from Fig. 4.4(b) that an increase in particle concentration results in a slight increase in the top channel width at the beginning, but when the particle concentration is increased to beyond a certain value, the top channel width seems to decrease slightly. This is possibly caused by particle interference which becomes significant in affecting the overall material removal when the particle concentration is increased to beyond a critical value. By contrast, an increase in the particle size or nozzle traverse speed leads to a decrease in the top channel width, as shown in Figs. 4.4(c) and (d). The trend with respect to the particle size is probably due to the fact that larger particles are less likely to diverge so that a more converged particle trajectory yields a smaller channel width.

By contrast, a higher traverse speed results in fewer particles that attack a given area of the target material where the particles at the jet rim are unable to widen the channel, so that the channel becomes narrower.

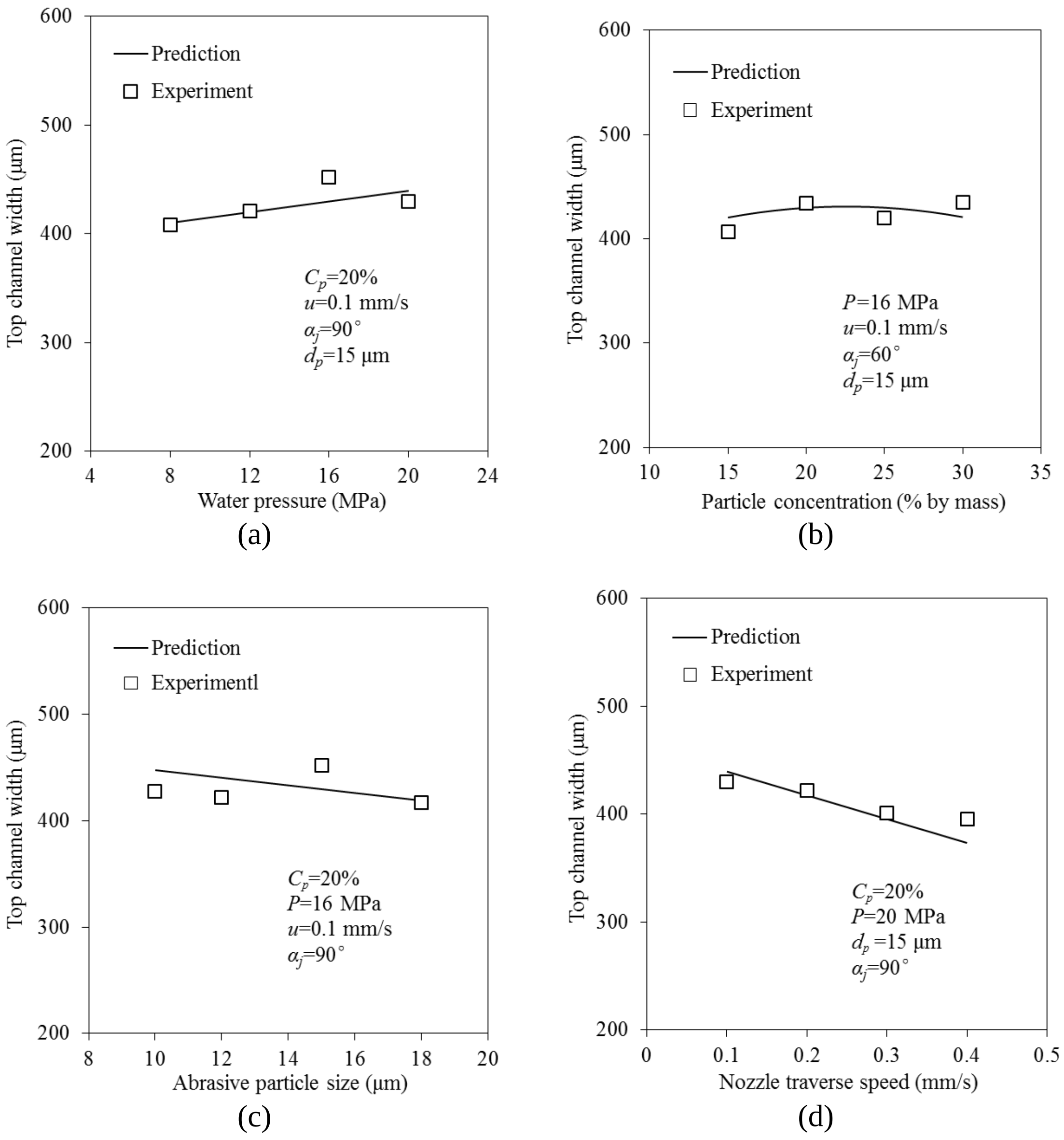

Fig. 4.4. Comparison between predicted and experimental top channel widths.

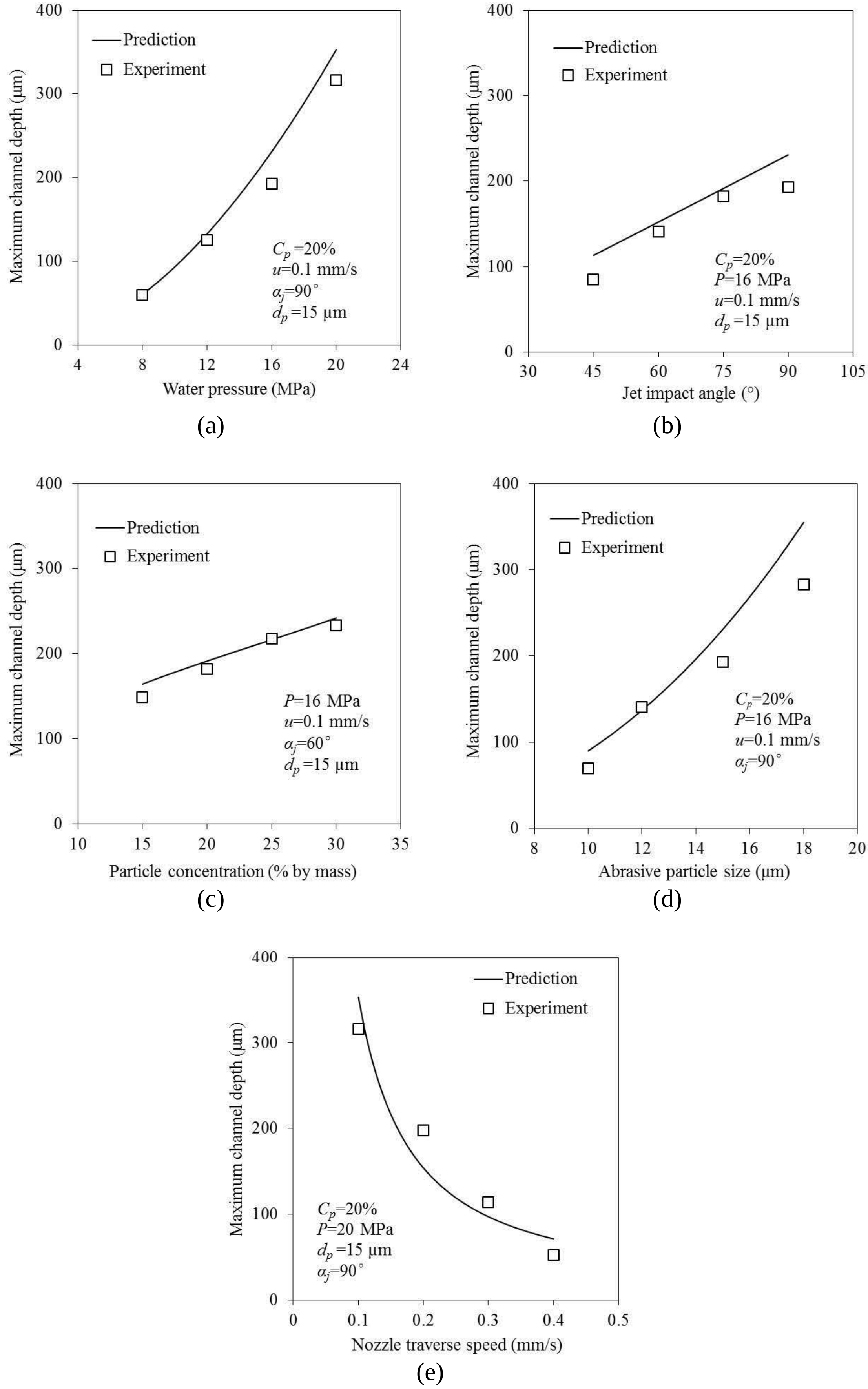

Fig. 4.5. Comparison between predicted and experimental maximum channel depths.

The maximum channel depth can be calculated from Eq. (4.42) using the predicted MRR and top channel width. The predicted channel depths are assessed by comparing them with the experimental data obtained from the model verification tests. The maximum channel depth shows an increasing trend with an increase in water pressure, jet impact angle, particle concentration and abrasive particle size, as shown in Figs. 4.5(a) to (d), respectively. More kinetic energy of the impacting particles can be brought into the cutting process by increasing the water pressure, abrasive particle size and particle concentration, and hence creating an increased channel depth. Again, brittle erosion mode is facilitated by using large jet impact angles, which increases the erosion rate as well as the channel depth (Fig. 4.5(b)). By contrast, the channel depth decreases with an increase in nozzle traverse speed, as shown in Fig. 4.5(e). It is attributed to the fact that a higher traverse speed allows less jet-material interaction time which in turn yields a smaller depth of cut.

4.3.2 Quantitative assessment

In order to assess the predictive ability and adequacy of the developed models for channelling performance, a further quantitative analysis was conducted based on the percentage deviations of the model predictions with respect to the corresponding experimental data. The percentage deviations are calculated from the following equation:

$$\text{Percentage Deviation} = \frac{\text{Model prediction - Experimental data}}{\text{Experimental data}} \times 100\% \qquad (4.47)$$

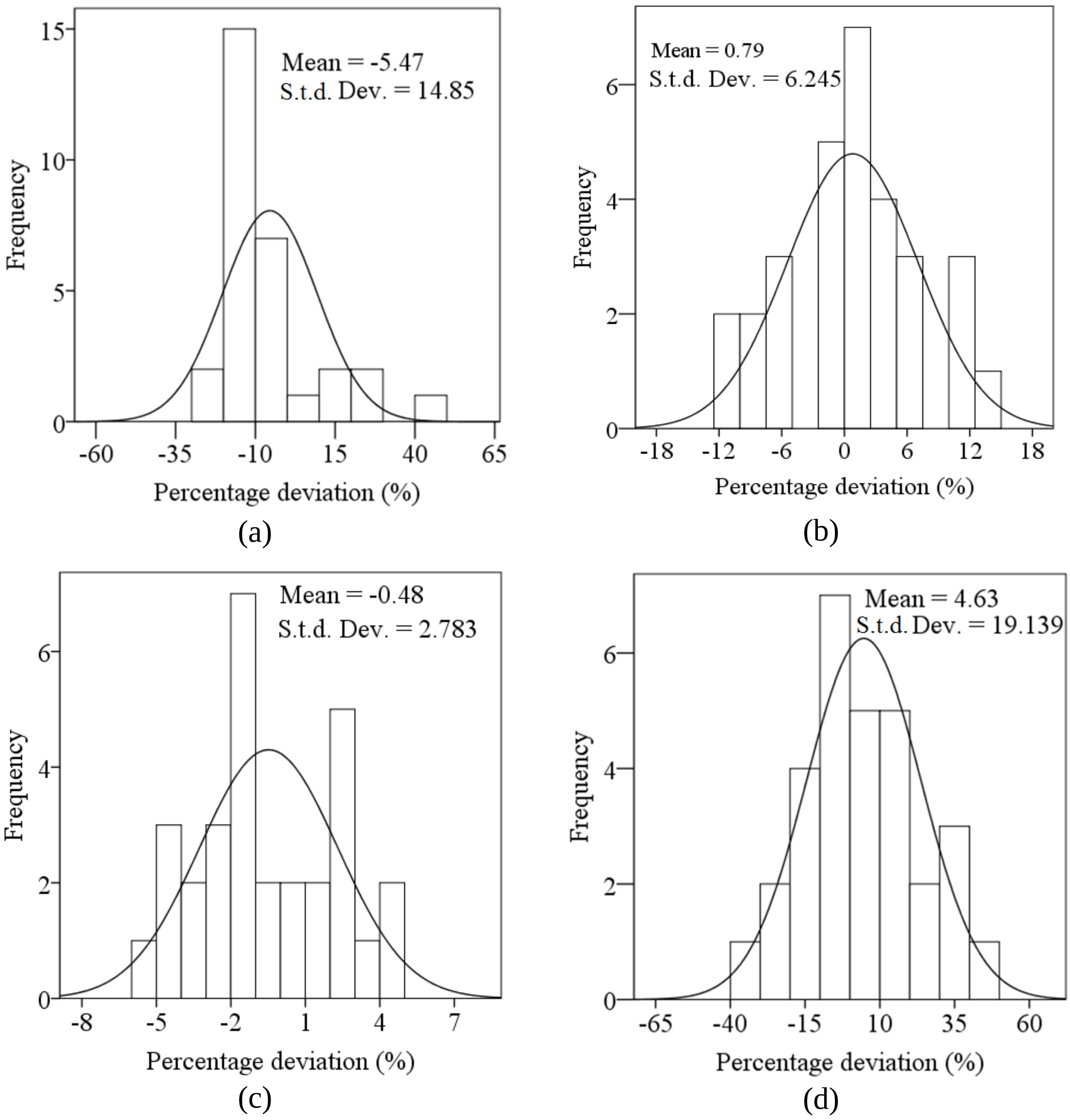

Fig. 4.6. Percentage deviations of model predictions with the corresponding experimental data: (a) MRR, (b) channel wall inclination angle, (c) top channel width, and (d) maximum channel depth.

By comparing it with the experimental data from the 30 model verification tests, the mean and standard percentage deviations are shown in the histograms in Figs. 4.6(a) to (d) for MRR, channel wall inclination angle, top channel width and maximum channel depth, respectively. For the MRR, the mean deviation is -5.47% with a standard deviation of 14.85%. For the channel wall inclination angle, the model predictions yield an average deviation of 0.79% with a standard deviation of 6.25%, while for the top channel width the mean deviation is -0.48% and the standard deviation is 2.78%. By contrast, the average deviation for the maximum channel depth is 4.63% with the standard deviation of 19.14%. It has been found that both the mean and standard deviations are acceptable. Thus, it may be stated that developed models can give adequate predictions of these four quantities in ASJ micro-channelling on a quartz crystal within the ranges of the variables considered in this study.

4.4 Concluding remarks

In this chapter, predictive models for the major micro-channelling performance measures, i.e. MRR, channel wall inclination angle, top channel width and maximum channel depth, have been developed. A dimensional analysis technique has been employed to develop the models for MRR and channel wall inclination angle, while the model for the top channel width was established by regression analysis of the experimental data. The model for the maximum channel depth was then derived from the MRR and top channel width equations by using their geometrical relationships.

The predictive model for MRR was first developed based on the assumption that the overall material removal in ASJ micro-machining is the accumulation of material removed by individual abrasive particles. In order to obtain the predictive model for the material removed by a single particle impact, a dimensional analysis approach was used to relate the material removal volume to its influencing parameters. To arrive at the MRR model, the predictive model for the abrasive particle impact angle was also obtained from a dimensional analysis which took into account the squeeze film effect when evaluating abrasive particle velocity. The coefficients (constants and exponents) in the MRR equation were determined by regression analysis of the experimental data obtained from the 92 tests as stated in Chapter 3.

The predictive model for the channel wall inclination angle has also been developed using a dimensional analysis, in which the influencing parameters, such as the target material properties, abrasive particle properties and major process parameters, were considered to form the model, and a regression analysis of the experimental data from Chapter 3 was performed to obtain the coefficients in the model.

By contrast, the predictive model for the top channel width was developed using a regression analysis. Several forms of equations were assessed. It was found that the quadratic form gave the highest coefficient of determination and was therefore selected. According to the ANOVA results given in Chapter 3, it was found that only four parameters, namely abrasive particle size, water pressure, nozzle traverse speed and abrasive particle concentration, played a significant role in affecting the top channel width, so that the regression analysis of the experiment data was carried out based only on these four parameters. In order to simplify the model, a backward elimination technique was used to eliminate the non-significant terms from the developed model.

The model for the maximum channel depth was finally derived based on an idealised channel cross-sectional profile and using the models for the MRR and top channel width.

The models have finally been verified experimentally with the help of an additional 30 model verification tests. The effect of the process parameters was first examined to assess the plausibility of the models. It has been shown that the predicted trends of the major micro-channelling performance measures correlated very well with the corresponding experimental data. A quantitative study was then performed to assess the predictive ability and adequacy of the models based on the percentage deviations of the model predictions with regard to the corresponding experimental data. It has been shown that both the mean and standard percentage deviations are small and acceptable. Therefore, the models developed in this study can provide an adequate prediction of micro-channelling performance.

Chapter 5

The erosion process by high velocity single micro-particle impact

5.1 Introduction

In Chapter 3, an experimental investigation into the AWJ micro-channelling process for a quartz crystal has been presented with a focus on exploring its machining process and performance, as well as the associated erosion process. It has been found that the fundamental action that takes place in AWJ micro-machining is the impact of high velocity micro-particles on the target surface, which causes material removal by means of impact erosion. While the study has identified that material removal in the impact erosion is made in the forms of craters, scratches and micro-dents, as well as the relationship between material removal and the impact velocity, a further understanding of the erosion process and mechanisms is essential to guide the development of the AWJ micro-machining technology.

As reported in the Literature Review, the numerical method is found to be a powerful tool to study the particle impact erosion, and can give more information that is difficult or impossible to obtain experimentally. The numerical method is therefore employed to study the particle impact process in this chapter. As discussed in the Literature Review, the DEM appears to be a suitable approach for the purpose of this study.

In this chapter, a DE model is developed to represent the impact process by a high velocity micro-particle on a brittle specimen, namely a quartz crystal. The developed model is then verified numerically and experimentally. The model is finally used for a study to understand the various aspects of the impact process, including the material removal process and mechanisms, energy consumption during an impact process, and the impact-induced cracks left on the target.

5.2 Discrete element model

5.2.1 Target solid specimen model

In order to model the material response to the impact of a micro-particle using DEM, it is essential to create a solid specimen whose mechanical properties are the same as those of the real target material. For this purpose, the BPM is used, in which a solid specimen is divided into a selected number of spherical elements that are bonded together at their contact points as shown in Fig. 5.1(a). The BPM is implemented in a three-dimensional (3D) software program, PFC3D, using a parallel-bond model which can transmit both forces and moments between spherical elements and is often used to simulate solid specimens of brittle materials [105-107].

A parallel bond can be envisioned as a finite-sized disk of elastic massless material around the contact and centred at the axis connecting the centres of two spherical elements, as shown in Fig. 5.1(a). The disk is associated with a set of ideal elastic springs with normal stiffness and shear stiffness uniformly distributed over its circular cross-section. A mechanical deformation is reflected in the displacements of the generalised coordinates with respect to its initial position, contact elastic forces and moments. The resulting force and moment (Fig. 5.1(b)) are developed within the solid specimen according to its constitutive law as given below.

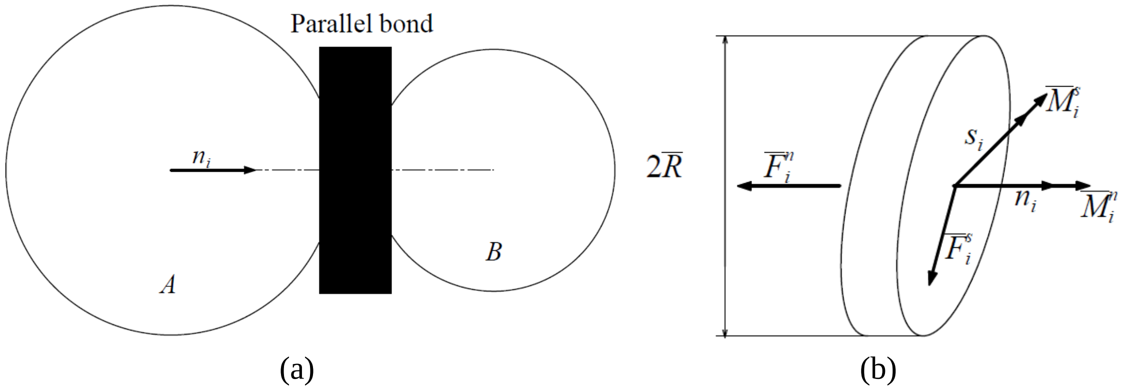

Fig. 5.1. Parallel-bond model: (a) parallel-bond idealization, and (b) forces and moments carried in the bond material.

The contact force and moment carried by the parallel bond between the spherical elements can be resolved into normal and shear components with respect to the contact plane and are expressed as

$$\bar{F}_i = \bar{F}_i^n + \bar{F}_i^s \tag{5.1}$$

$$\bar{M}_i = \bar{M}_i^n + \bar{M}_i^s \tag{5.2}$$

where $\bar{F}_i^n$ and $\bar{F}_i^s$ are the force components at the normal and shear directions, respectively, with respect to the parallel bond, and $\bar{M}_i^n$ and $\bar{M}_i^s$ are the moments at these two directions.

Thus, the maximum tensile and shear stresses acting on the bond can be given by

$$\sigma_{\max} = \frac{-\bar{F}^{n}}{A} + \frac{\left|\bar{M}^{s}\right|}{I}\bar{R} \tag{5.3}$$

$$\tau_{\max} = \frac{\left|\bar{F}^{s}\right|}{A} + \frac{\left|\bar{M}^{n}\right|}{J}\bar{R} \tag{5.4}$$

where $\bar{F}^{n}$, $\bar{F}^{s}$, $\bar{M}^{n}$ and $\bar{M}^{s}$ are the scalar value of $\bar{F}_i^{n}$, $\bar{F}_i^{s}$, $\bar{M}_i^{n}$ and $\bar{M}_i^{s}$, respectively, A, I and J are the area, moment of inertia and polar moment of inertia of the parallel bond cross-section, respectively, and $\bar{R}$ is the parallel bond radius as shown in Fig. 5.1(b).

In a parallel bond, the relative motion at the contact causes a force and a moment to act on the two bonded spherical elements, thus affecting the maximum tensile and shear stresses between them. If either of these maximum stresses exceeds its corresponding bond strength, the parallel bond breaks, so that two failure modes occur, namely bond breakage by tensile failure and bond breakage by shear failure.

Since the behaviour of a brittle material in a material removal process is dominated by its mechanical properties, such as Young's modulus of elasticity, Poisson's ratio, compressive strength and fracture toughness [49, 117], it is important to properly define these properties for the spherical elements, so that the specimen constructed in the DE model can represent the real material properties. The material used in this study is a quartz crystal whose properties were given in Table 3.1 in Chapter 3, while Table 5.1 gives the corresponding properties in the BPM that are determined as follows. The minimum diameter of the spherical elements is chosen to be equal to 3 μm to ensure a fine resolution for the simulation. The effect of spherical element size on the simulation results is assessed in the next section. The target solid specimen tends towards a crystalline arrangement when the spherical element size ratio (the ratio of the maximum radius of the spherical elements to the minimum radius of the spherical elements) is unity [101], so that a uniform spherical element size (3 μm) distribution is used to model the target specimen. Other properties in the BPM are determined according to Refs. [101, 133, 134].

Table 5.1. Properties in parallel bond model.

Properties	Values
Minimum spherical element size in radius, R_{min}, (μm)	1.5
Spherical element size ratio, R_{max}/R_{min}	1
Density of the spherical elements, ρ, (kg/m^3)	2200
Young's modulus of the spherical elements, E_c, (GPa)	55
Ratio of normal to shear stiffness of the spherical elements, k_n/k_s	1.1
Particle friction factor, μ	0.4
Young's modulus of the parallel bond, $\bar{E}_c$, (GPa)	55
Ratio of normal to shear stiffness of the parallel bond, $\bar{k}_n/\bar{k}_s$	1.1
Radius multiplier of the parallel bond, $\bar{\lambda}$	1
Tensile strength of the parallel bond, $\bar{\sigma}_n$, (MPa)	827
Shear strength of the parallel bond, $\bar{\sigma}_c$, (MPa)	1200

5.2.2 Model geometry and boundary conditions

The geometry of the solid specimen is modelled as shown in Fig. 5.2. To consider the experimental work that has been stated in Section 3.3 of Chapter 3 where the average impacting particle size of 27 μm is used, a larger target specimen size may need to be employed to minimise the boundary effect. To assess the specimen size effect, specimens of four dimensional sizes as given in Table 5.2 were tested, together with the spherical elements of 3 μm in diameter, using a rigid particle of 27 μm (d_p) to impact the target at the 90° angle (α_p) and 164 m/s velocity (v_p). The mass of material removed for each specimen was calculated, as given in Table 5.2, which appears to be stable when the model dimensions vary from 100×100×30 μm^3 to 200×200×75 μm^3. Thus, the solid specimen with the dimensions of 150×150×50 μm^3, consisting of 51,725 spherical elements, is selected for the model to achieve an accurate solution and reduce the computation time.

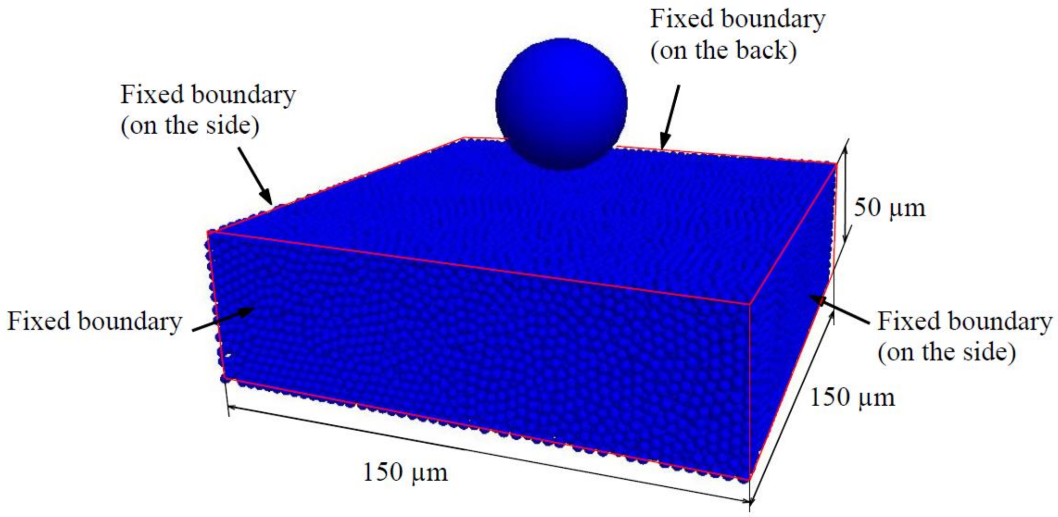

Fig. 5.2. Model geometry and boundary conditions.

Table 5.2. Effect of specimen size on simulation results (d_p=27 μm, α_p=90°, and v_p=164 m/s).

Specimen size (μm^3)	NO. of spherical elements	Material removal mass (×10^{-13} kg)
50×50×30	3448	5.8
100×100×30	13793	7.2
150×150×50	51725	7
200×200×75	137934	7.2

Likewise, the effect of the element size was examined considering the computation time and model accuracy, where the spherical element sizes at 2, 3, 4, 5 and 6 μm in diameter were tested with the specimen dimension of 150×150×50 μm^3. The mass of material removal for each element size was calculated and is presented in Fig. 5.3. It can be noticed that there is a negligible difference for the mass of material removal when the particle size of 2 to 4 μm is used. As such, the spherical element of 3 μm in diameter is chosen.

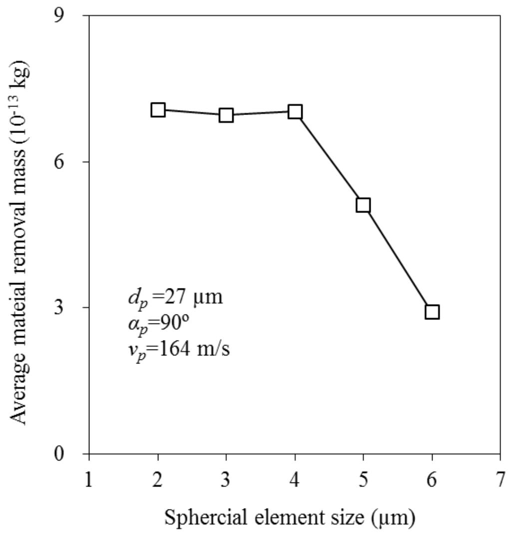

Fig. 5.3. Effect of spherical element size on the simulation results.

The boundary conditions are as follows: the top face of the specimen is set free which is to be impacted by a particle, while spherical elements on the other five exterior faces of the specimen are set at zero freedom in both translational and angular velocities.

In this study, alumina (Mohs hardness 9) particles are used as the impacting particles and are considered to be significantly harder than the target quartz crystal (Mohs hardness 7). Thus, the impacting particle may be considered as a rigid body as commonly assumed in simulation studies, and particle fragmentation is not considered in this study for the same reasons given in [37]. It is noted that based on experimental observations [90, 91, 135], very little plastic deformation occurred on silicon or quartz crystals during the high velocity micro-particle impact process, and material removal was mainly realised by brittle fractures. As such, plastic deformation is not considered.

Heat can be generated in an impact process mainly due to plastic deformation and friction if the impacting particle slides on the target. Since plastic deformation is neglected as discussed above, and frictional loss during an impact process is small as will be discussed later in this chapter, the heat generated is believed to be small. In addition, although the fracture toughness of a brittle material increases considerably with temperature at a quasi-static loading condition [136], at a dynamic loading condition, both the hardness and the toughness are considered invariant with temperature within the conditions of this study [137]. Consequently, thermal diffusion is not considered in the single impact model.

5.3 Model verification

5.3.1 Mechanical properties of target solid specimen

It is first necessary to verify the mechanical properties of the target solid specimen constructed above, for which a compression test and a fracture toughness test are simulated to obtain and assess these quantities of the solid specimen with respect to the corresponding physical properties of the target material.

5.3.1.1 Numerical compression test

A numerical compression test was conducted to get the stress-strain relationship, which was then used to estimate Young's modulus of elasticity, Poisson's ratio and the compressive strength of the specimen. In PFC3D, the numerical compression test can be simplified to a model of two moving walls compressing the specimen as illustrated in Fig. 5.4. The loading walls move toward each other at a slow speed to apply a quasi-static load. In this numerical test, the specimen dimension considered was 40×40×80 μm^3 and the properties involved in the spherical elements were set according to Table 5.1. Unlike ductile materials, the stress-strain curve for brittle materials is typically linear over their full range of strain, and terminates at the ultimate strength without appreciable plastic deformation [138]. The maximum stress loading on the specimen causes the failure of the specimen. By analysing the stress-strain relationship determined from the numerical test, the elastic modulus, Poisson's ratio and compressive strength of the target specimen can be caclulated as given in Table 5.3. It can be seen that all mechanical behavour quantities of the solid model are in good agreement with the properties of the target material.

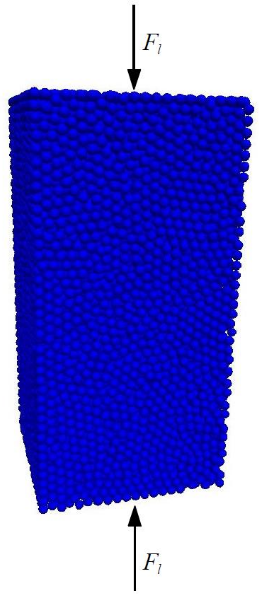

Fig. 5.4. Compression test on solid specimen.

5.3.1.2 Fracture toughness test

The numerical toughness test was performed based on the principle of the single-edge notch bending (SENB) test used in practice to determine the fracture toughness of a material, as shown in Fig. 5.5(a). The model for the numerical test is given in Fig. 5.5(b), where the specimen was 0.04 mm in height (W) and width (B), and the crack length (a) is set to be at half of the height. Two fixed rigid cylinders at the distance of $4W$ were used to support the specimen, and a third cylinder at the centre of the two supports moves downward at a slow speed to apply a quasi-static load. The loading force applied is a function of time. The force may fluctuate at the beginning, and then increases steadily until the maximum that causes the failure of the specimen. The fracture plane is shown by the red lines in Fig. 5.5(b). The maximum force (F_l) is then used to calculate fracture toughness according to the formula given in [139], i.e.

$$K_{Ic} = \frac{4F_l}{B}\sqrt{\frac{\pi}{W}}\left\{1.6\left(\frac{a}{W}\right)^{1/2} - 2.6\left(\frac{a}{W}\right)^{3/2} + 12.3\left(\frac{a}{W}\right)^{5/2} - 21.2\left(\frac{a}{W}\right)^{7/2} + 21.8\left(\frac{a}{W}\right)^{9/2}\right\} \tag{5.5}$$

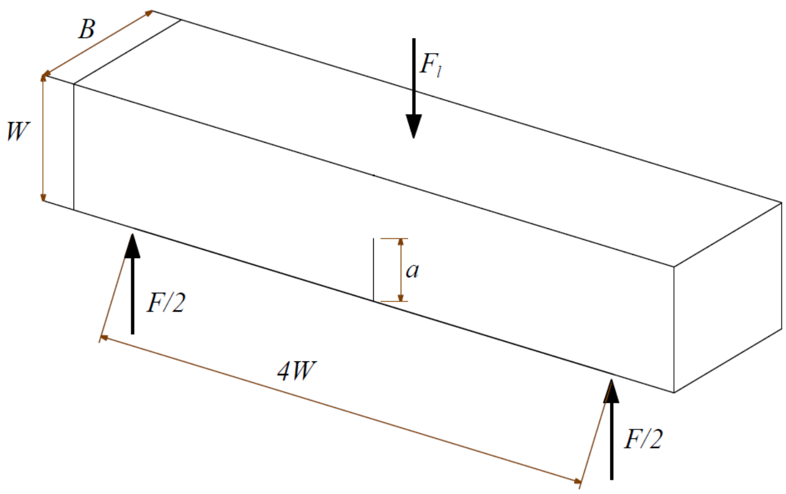

(a)

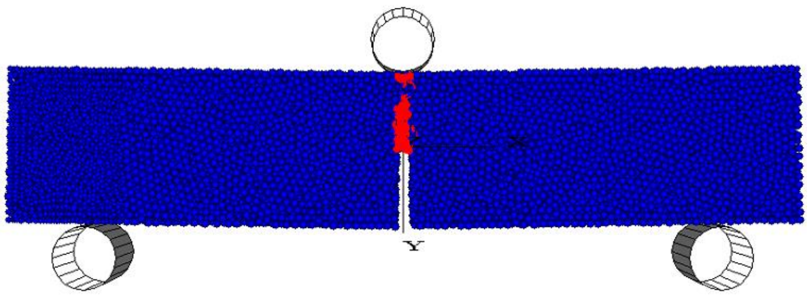

(b)

Fig. 5.5. Fracture toughness test on solid specimen: (a) SENB specimen for fracture toughness test, and (b) numerical model of SENB test (red lines represent cracks).

It has been found that the mechanical properties of a solid specimen in the DE model agree well with those of the real target material, as shown in Table 5.3. Thus, it may be stated that the specimen model can represent the mechanical behaviour of the quartz crystal considered.

Table 5.3. Comparison of quartz crystal properties between real target and solid specimen.

Material properties	Quartz crystal	Solid specimen model	Errors (%)
Elastic modulus (GPa)	72	69	4.1
Compressive strength (GPa)	1.1	1.3	18.1
Poisson's ratio	0.16	0.16	0
Fracture toughness (MPa·m$^{0.5}$)	1.2	1.13	5.8

5.3.2 Experimental verification

A set of single micro-particle impact tests on a quartz crystal was stated in Section 3.3. The impact conditions included four impact angles at 30°, 50°, 70° and 90°, and four impact velocities at 100, 130, 150 and 164 m/s. The experimental data are used to verify the DE model by comparing the model predicted and the experimental material removal mass under the corresponding conditions. Since the micro-dents and scratches formed by individual particle impacts make little contribution to material removal, as discussed in Chapter 3, the experimental material removal mass is based on the craters formed in the tests, where the volume of the craters was measured using a Keyence Model VK-X200 3D laser measurement microscope with a 0.5 nm resolution and the density of the material in the impact zone was assumed to be unchanged and constant.

The impact conditions in the experiment were also used in the DE model to obtain the mass of the material removed. Fig. 5.6 shows the comparison of the model predicted and corresponding experimental material removal mass, where each experimental data point represents the average material removal mass of 20 craters. Likewise, each simulated data point in Fig. 5.6 is the average material removal mass at four random locations on the solid specimen surface, although these four data are very close to each other. It can be seen that the model predictions are in good agreement with the corresponding experimental data for all impact velocities and impact angles. The average and standard deviations of the model predicted from the corresponding experimental material removal mass are 0.07% and 24.7%, respectively. The model is now used to simulate the impact process as follows.

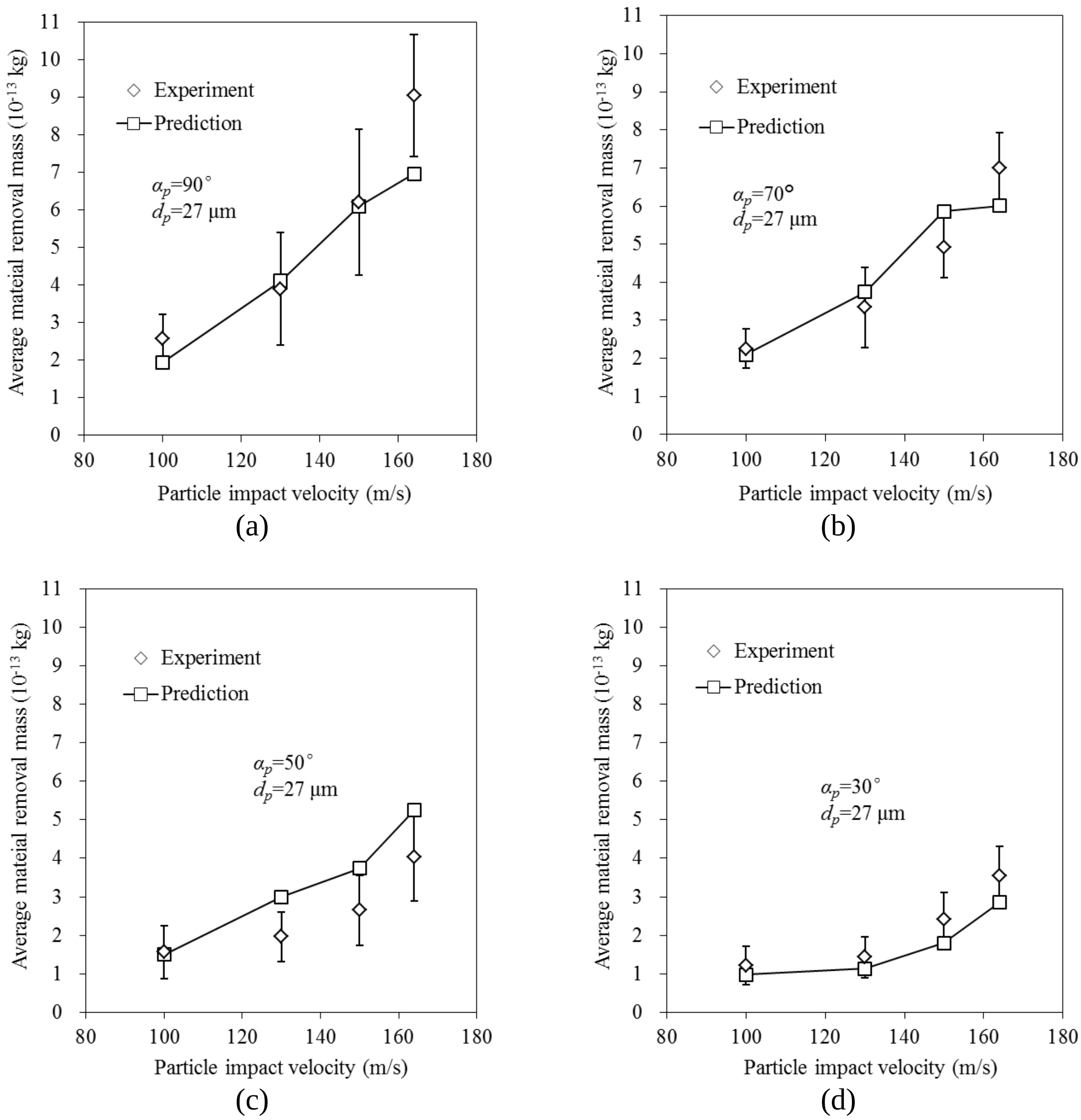

Fig. 5.6. Comparison between simulated and experimental material removal mass (error bars show the standard deviation of the experimental results).

5.4 Simulation results and discussion

5.4.1 Material removal mechanisms

5.4.1.1 The particle-target impact event

With the DE model, the particle-target interaction during an impact process can be examined to provide an insight into the impact event. As a rigid particle impacts the target specimen, the energy is transferred to the surrounding spherical elements, resulting in an increase in the tensile and shear stresses on the bonded spherical elements, as shown in Eqs (5.3) and (5.4). If either of these stresses exceeds their corresponding bond strength, the bonds begin to break, forming cracks inside the solid specimen. At the beginning of the impact, a high compressive force can be found at the region near the contact zone, which usually results in a high stress field as shown in Fig 5.7(a). The cracks under the contact zone are then initiated by the high stress, as illustrated in Fig. 5.7(b). As the impact event progresses where the particle velocity decreases, the contact force redistributes and propagates into the target specimen to induce further cracks. It has been found that crack propagation is associated with the direction of the contact force, as shown in Figs. 5.7(c) and (d). Detailed crack propagation during an impact process will be discussed in a later section. Fig. 5.8 shows a detailed contact force distribution in the normal and shear directions. It can be found that with the progress of the impact process, the shear stress induced by the shear force leads to cracks only around the contact point, but the tensile stress from the normal force dominates crack propagation into the solid specimen.

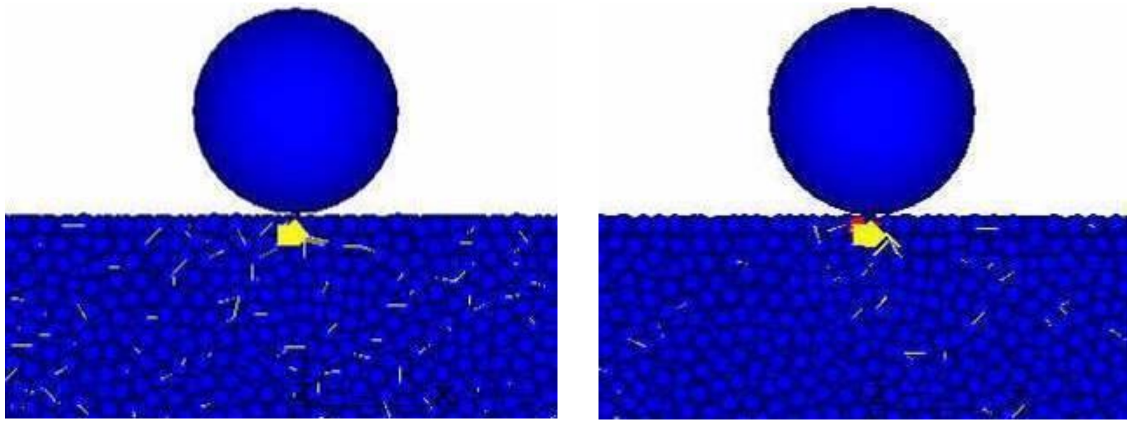

(a) t=0.5 ns (b) t=1 ns

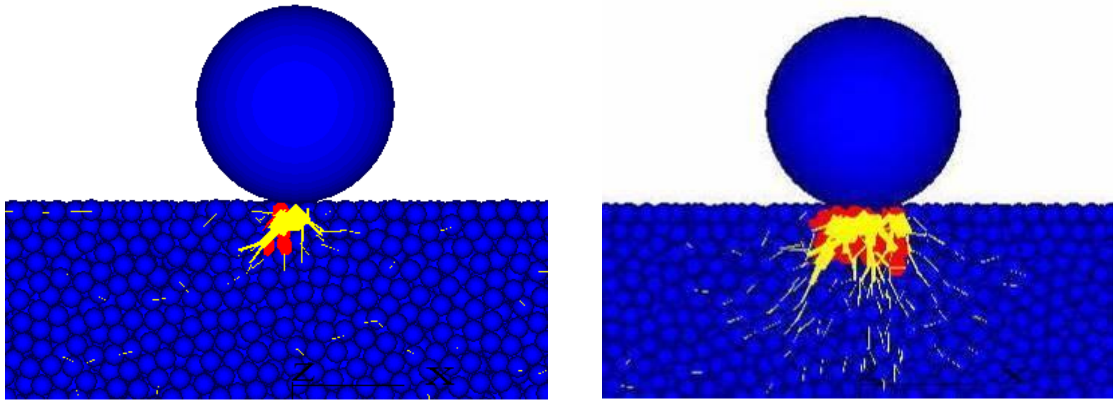

(c) t=2.7 ns (d) t=10 ns

Fig. 5.7. Contact force distribution from simulation (d_p=27 μm, α_p=90°, and v_p=164 m/s; yellow lines are the contact force and their thickness represent the magnitude, red lines represent cracks).

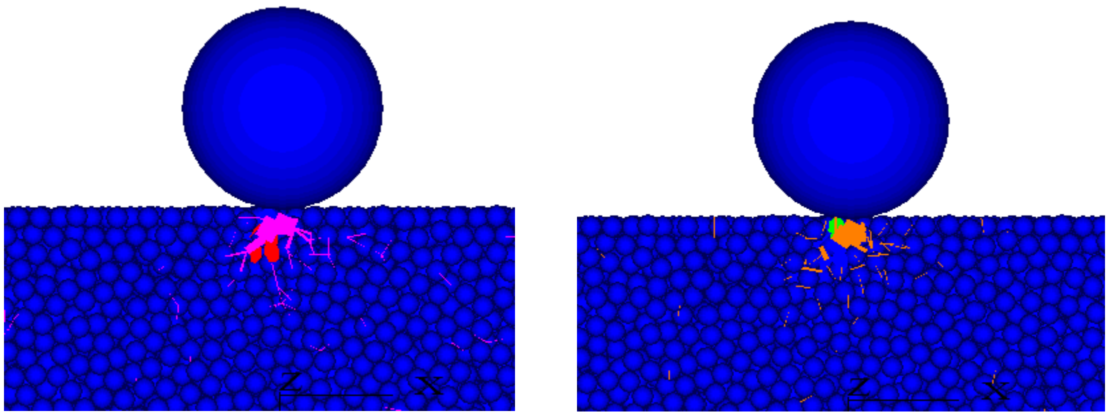

(a) Normal force distribution (b) Shear force distribution

Fig. 5.8. Normal and shear force distribution at t=2.7 ns (d_p=27 μm, α_p=90°, and v_p=164 m/s; magenta lines are the normal force and red lines represent its corresponding cracks in (a), orange lines are the shear force and green lines represent its corresponding cracks in (b)).

5.4.1.2 Energy conversion

When a high velocity particle impacts a solid specimen, the energy consumed E_{con} during the impact can be defined as

$$E_{con} = E_0 - E_1 \tag{5.6}$$

where E_0 and E_1 are the kinetic energy of the particle before and after the impact process, respectively.

E_{con} may be consumed in four different ways, namely crack formation and propagation, frictional loss, conversion to the kinetic energy of the removed material, and residual energy stored in the target after the impact.

The frictional loss occurs if the particle slides on the solid specimen during an impact. The residual energy here is defined as the strain energy that stores in all the contacts and bonds of the solid specimen after the impact process. In theory, strain energy is the energy stored in a body due to deformation under a loading; it then releases gradually and may induce a crack formation [140]. Residual strain energy may still exist in the material after the gradual unloading process [141]. The removed material can also take some energy away from the target. However, most of the consumed energy has been found to be responsible for the bond breakage among spherical elements, which contributes to material removal from the solid specimen. Typical proportions of the energy consumed for crack formation and frictional loss are plotted in Fig. 5.9 with respect to impact angle. It has been found that the energy for crack formation and propagation is dominant, representing 60-88% of E_{con}, while consumption of energy by frictional loss is in the range of 10-35% of E_{con}. The residual energy in the target and the kinetic energy in the removed material only account for less than 1% each.

It can be seen that an increased amount of energy is consumed for crack formation and propagation as the particle impact angle is increased, while a reverse trend applies for frictional loss. It is apparent that a larger impact angle yields a smaller force component along the impact surface and an increased force normal to the target. This in turn increases the force or energy used in the impact and reduces the force for friction loss through particle sliding along the target surface. Fig. 5.9 appears to have correctly shown these trends.

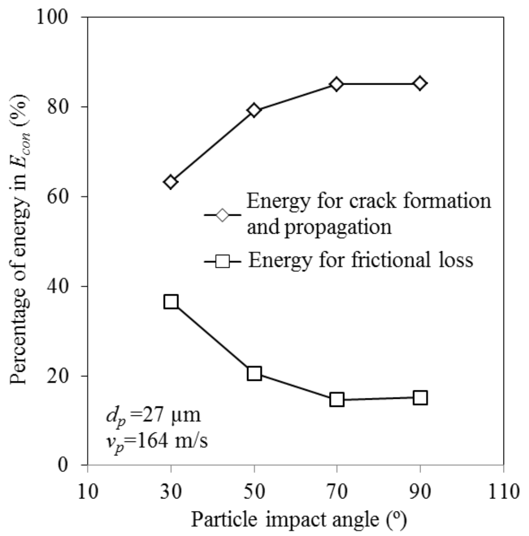

Fig. 5.9. Effect of impact angle on the percentage of energy consumed as frictional loss and for crack formation and propagation.

5.4.1.3 Crack propagation

Unlike in static indentation, the contact time by the impact of a high velocity micro-particle is so short that it is difficult to observe the crack propagation process from experiments. However, the DE model provides an effective means for this purpose, as displayed in Fig. 5.10 where the red and green marks represent bond breakage (cracks) by tensile failure and shear failure, respectively.

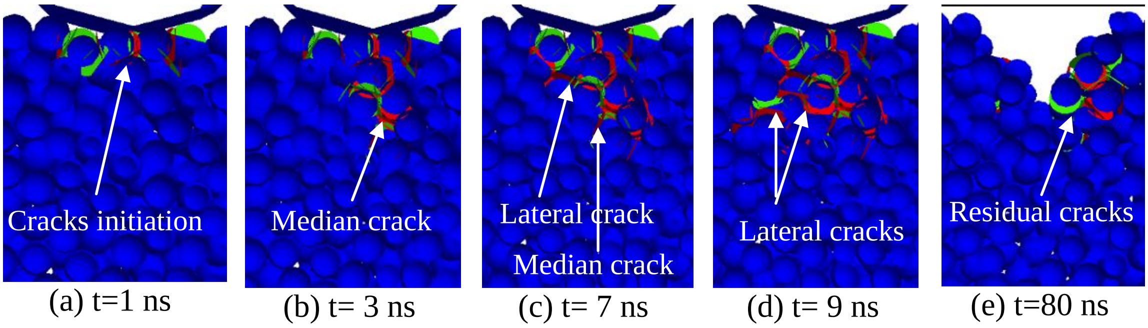

Fig. 5.10. Material removal process with respect to impact time (d_p=27 µm, α_p=90°, and v_p=164 m/s; red and green lines represent the cracks by tensile failure and shear failure, respectively).

Generally, when the impact force is sufficient to cause cracks, the cracks first initiate around the contact zone between the impacting particle and the target that is subjected to structural densification or plastic flow due to a combination of highly hydrostatic compression and shear stresses [97, 117, 128]. The shear stresses provide the driving force to develop cracks close to the impact zone (Fig. 5.10(a)) where most of the cracks are caused by shear failure. With the development of the impact event (while the particle velocity decreases), two main propagation paths of the cracks are observed; the median cracks which propagate almost perpendicularly to the surface, as indicated in Fig. 5.10(b), and the lateral crack that propagates almost in parallel to the surface and terminates at the free surface, as shown in Figs. 5.10(c) and (d). When the particle velocity decreases to zero, it may be rebounded from the target. The continuous bond breakage in the impact area and the coalescence of cracks eventually causes some spherical elements to escape from the target specimen, as shown in Fig. 5.10(e). Since not all the cracks contribute to the material removal from the solid specimen, the spherical elements that have breakage in all their contacts are defined as the removed elements, while spherical elements that do not totally break from its adjacent elements still belong to the solid specimen where cracks around these elements are defined as residual cracks. Therefore, after the impact process, some residual cracks may still exist in the impact area which could decrease the strength of the substrate and facilitates material removal in a subsequent impact.

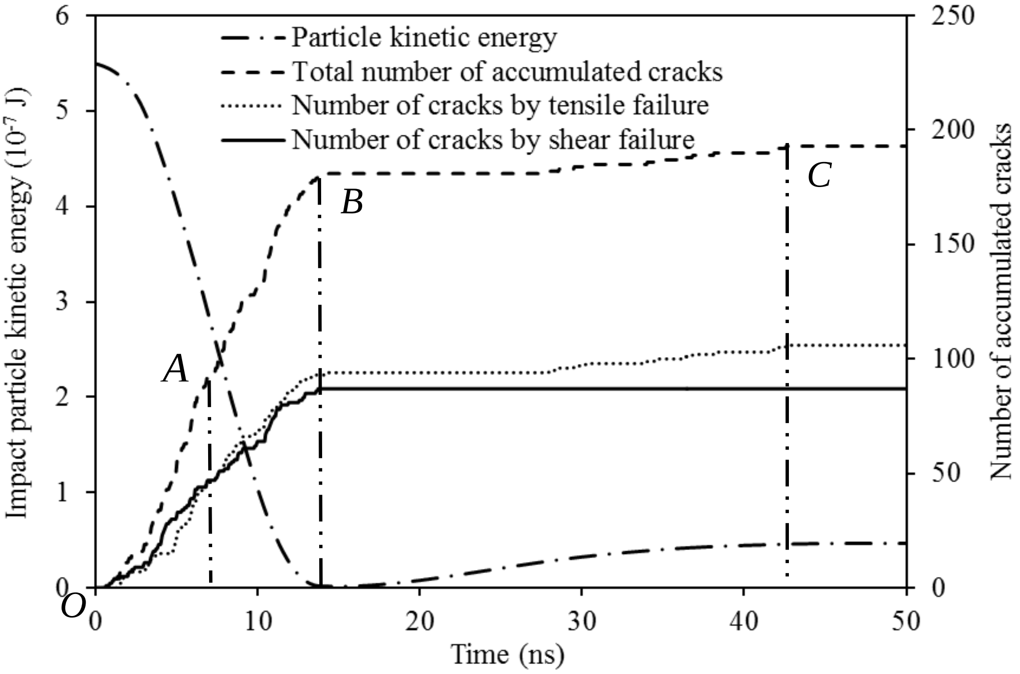

Fig. 5.11. The relationship between impacting particle kinetic energy and the number of accumulated cracks during an impact process (d_p=27 µm, α_p=90°, and v_p=164 m/s).

The relationship between the impacting particle kinetic energy and the number of accumulated cracks during the impact process is shown in Fig. 5.11 as a function of the impact time (or particle-target interaction time). It can be seen that an increase in the number of accumulated cracks is associated with a decrease in the impacting particle kinetic energy. This is due to the fact that more energy is transferred to the surrounding spherical elements, resulting in more bond breakage among the elements in the solid specimen. The small increase of the particle energy from about 15 ns is attributed to the rebounding or sliding of the particle. It is interesting to note from Fig. 5.11 that the impact process may be seen to have three stages. In the first stage as denoted by *OA* in Fig. 5.11, the number of cracks caused by shear failure is more than that of tensile failure. This is probably due to the high shear stress formed in the impact area. As the impact event progresses and the particle kinetic energy decreases, the cracks made by tensile failure start to dominate, as shown by stage *AB* in Fig. 5.11. In this stage, many lateral cracks may be formed, as shown in Figs. 5.10(c) and (d), which significantly contribute to the material removal process. When the particle kinetic energy reduces to zero, the particle begins to rebound from the target. During the rebounding process, the total number of cracks still increases very slightly, as illustrated in the stage denoted by *BC*. This is possibly attributed to the residual tensile stress that results in further bond breakages [117, 128].

From the above analysis, micro-cracks are initiated by high shear stresses in the impact zone, and with the progress of the impact event, both median and lateral cracks are formed in the solid specimen, more of which are caused by tensile stresses than shear stresses. The continued bond breakage in the impact area and the coalescence of the cracks eventually cause some spherical elements to be removed from the target.

5.4.2 Effect of impacting parameters on the erosion rate and subsurface damages

The effect of impacting parameters on the erosion rate and subsurface damages was simulated using the developed DE model for a rigid alumina particle of 27 μm to impact a solid specimen (quartz crystal) under four impact angles (30°, 50°, 70° and 90°) and four particle impact velocities (100, 130, 150 and 164 m/s). This is discussed below.

5.4.2.1 Effect on material erosion rate

Fig. 5.12(a) shows the relationship between particle impact velocity and material erosion rate (the ratio of the removed target material mass to the impacting particle mass) under different impact angles. The velocity exponent (*n*) in the erosion rate-velocity curve is also given in the figure. It has been found that the velocity exponents are around 2-3 for all the simulated conditions, which is consistent with that experimentally found for brittle materials [84, 142].

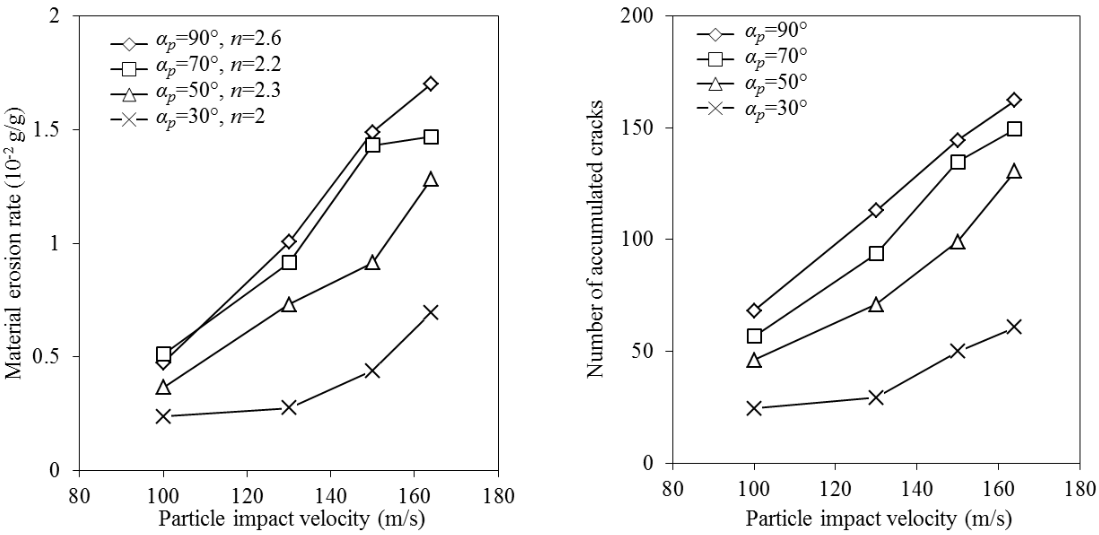

(a) (b)

Fig. 5.12. Effect of impacting parameters on: (a) material erosion rate, and (b) the number of accumulated cracks.

It can be seen in Fig. 5.12(a) that, in general, an increase in the impact angle or the impact velocity results in an increase in the erosion rate. The same trend is found for the number of accumulated cracks shown in Fig. 5.12(b). With an increase in the particle impact velocity or impact angle, more kinetic energy of the particle is transferred to the target as normal impact force which increases the formation of cracks for a brittle specimen, and hence the material erosion rate.

5.4.2.2 Effect on subsurface damage

Subsurface damage, such as micro-cracks, caused by the machining process is a major concern, particularly for micro-machining where such damages can significantly affect the functionality and reliability of the products. As discussed earlier, after the particle impact process, residual cracks may remain with the substrate. In this work, the number of residual cracks and the maximum crack depth, as depicted in Fig. 5.13, are considered as the criteria for assessing subsurface damages.

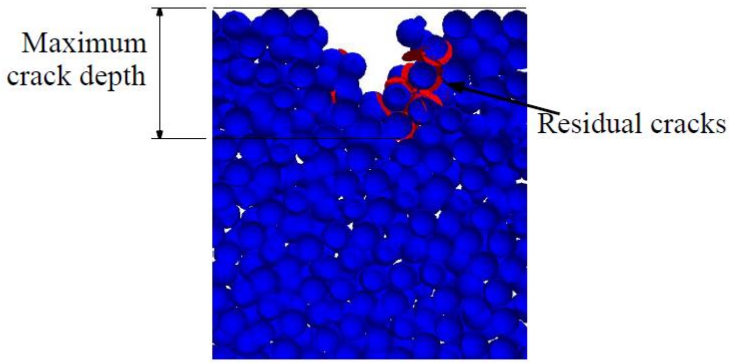

Fig. 5.13. Residual cracks and maximum crack depth after an impact process (d_p=27 μm, α_p=90°, and v_p=164 m/s; red lines represent cracks).

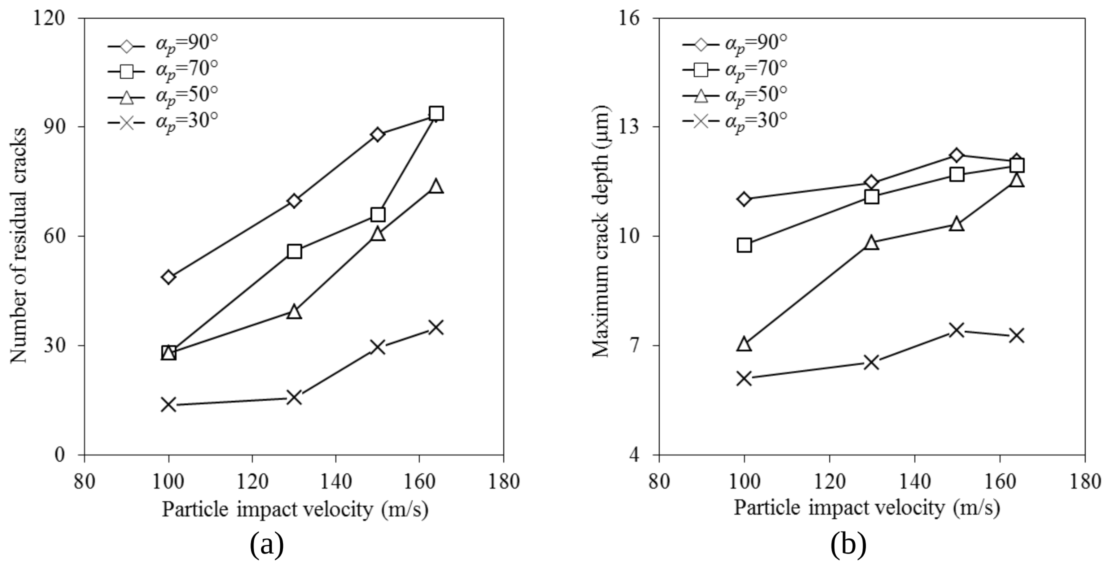

Fig. 5.14. Effect of impacting parameters on: (a) the number of residual cracks, and (b) the maximum crack depth.

Fig. 5.14 indicates that an increase in the particle velocity or the impact angle increases the number of the residual cracks as well as the maximum crack depth. This may be due to the fact that a larger impact angle or a higher impact velocity is associated with a larger velocity component perpendicular to the target surface, which provides more energy to the target to cause more and deeper cracks on the brittle material. It has been found from the simulation that this damage can be reduced by using a lower particle impact velocity and a smaller impact angle, but this is at the sacrifice of a reduced material erosion rate.

5.5 Concluding remarks

In this chapter, a DE model for representing the impact process by a high velocity micro-particle on a quartz crystal has been developed to explore the material removal process and mechanisms, energy consumption during the impact process, and the subsurface damage induced by the impact. The BPM, which is implemented in the PFC3D software, was used to construct the target solid specimen. In order to minimise the boundary effect, a relatively large rectangle target was modelled where the top surface was free to move and to be impacted by a particle, and the other five exterior faces were constrained.

The mechanical properties of the target solid specimen were then verified by material numerical tests, namely a compression test and fracture toughness test. The numerical compression test was conducted to get the stress-strain relationship, which was then used to estimate Young's modulus of elasticity, Poisson's ratio and the compressive strength of the solid specimen, while the numerical fracture toughness test was performed based on the principle of the SENB test used in practice to determine the fracture toughness of the solid specimen. It has been shown that the mechanical properties of a solid specimen in the developed DE model agreed well with those of the real target material, quartz crystal.

The measured crater volume data from a particle impact experiment given in Chapter 3 were converted to material removal mass and used to verify the DE model by comparing the model predictions with the corresponding experimental data. To account for the particle size and shape variation in the experiment, 20 craters for each test condition were measured and the average was used in the comparison. It has been shown that the model predictions are in a good agreement with the corresponding experimental data for all the impact velocities and impact angles considered. The average and standard deviations of the model predicted from the corresponding experimental material removal mass are 0.07% and 24.7%, respectively.

The model has then been used to simulate, and give an insight into, the impact process under various conditions. It has been found that 60-88% of particle energy is consumed for crack formation and propagation of the target, and frictional loss through relative particle-target sliding accounts for 10-35% of the particle energy. It has further been found that micro-cracks on the target are initiated by the high shear stresses in the impact zone, and these cracks appear only around the impact zone. As the progress of the impact event, both median and lateral cracks are formed in the deep layer of the solid specimen, more by tensile stresses than shear stresses. During the impact process, the continuous bond breakage in the impact area and the coalescence of cracks cause some spherical elements to escape from the solid specimen and hence the material removal. Furthermore, the effect of particle impact angle and velocity on the material erosion rate and subsurface damages has been investigated. It has been shown that an increase in the impact angle or velocity increases the material erosion rate and the subsurface damages represented by the number and depth of the cracks remaining on the target.

Chapter 6

The erosion process by high velocity multiple micro-particle impacts

6.1 Introduction

The impact process by a high velocity micro-particle on a quartz crystal has been presented in Chapter 5. Since the material removal in abrasive jet machining is regarded as an accumulation of the material removed by the impact of a flow of many high velocity micro-particles, it is important to understand the impact and erosive process by the impact of multiple particles.

In this chapter, the DE model presented in Chapter 5 is extended to the multiple micro-particle impact process incorporating a particle flow model. The impacting particles involved in the particle flow are arranged in layers to reduce the computation time. The developed model is then verified experimentally and used for a study of the material response to the high velocity multiple micro-particle impacts to explore the impact and material removal process under various impacting conditions. The residual cracks on the target will also be studied.

Due to the availability of the particle velocity model for the particles in an abrasive air jet and the absence of the shielding effect of the water film on the target surface in abrasive airjet machining, the study in this chapter is primarily based on the phenomenon of abrasive airjet machining.

6.2 Computational model for multiple impacts

When considering multiple particle impacts as in the case of AWJ machining, it is first necessary to develop a model to represent the realistic particle flow, followed by the development of a solid specimen whose mechanical properties can represent those of the real target material, quartz crystal.

6.2.1 Model of particle flow

6.2.1.1 Determination of the number of impacting particles

Fig. 6.1 shows a schematic representation of a micro-channelling process by an abrasive jet. The definitions of L and L_1 are depicted in Fig. 6.1(a), where the nozzle moves with a distance of L, and L_1 is the actual completed machining length to be considered in the simulation model. The structure of the particle flow in an abrasive jet is similar to an air jet flow in that both have a flow expansion. However, the jet expansion angle of a particle flow (θ_p), as shown in Fig. 6.1(a), is apparently smaller than that of an air jet due to the larger density and momentum of the abrasive particles. It was reported that the cored part of a particle jet expands with an expansion angle of approximately 7º [115]. As such, in order to realistically model the structure of the particle flow, the particle jet expansion angle is considered.

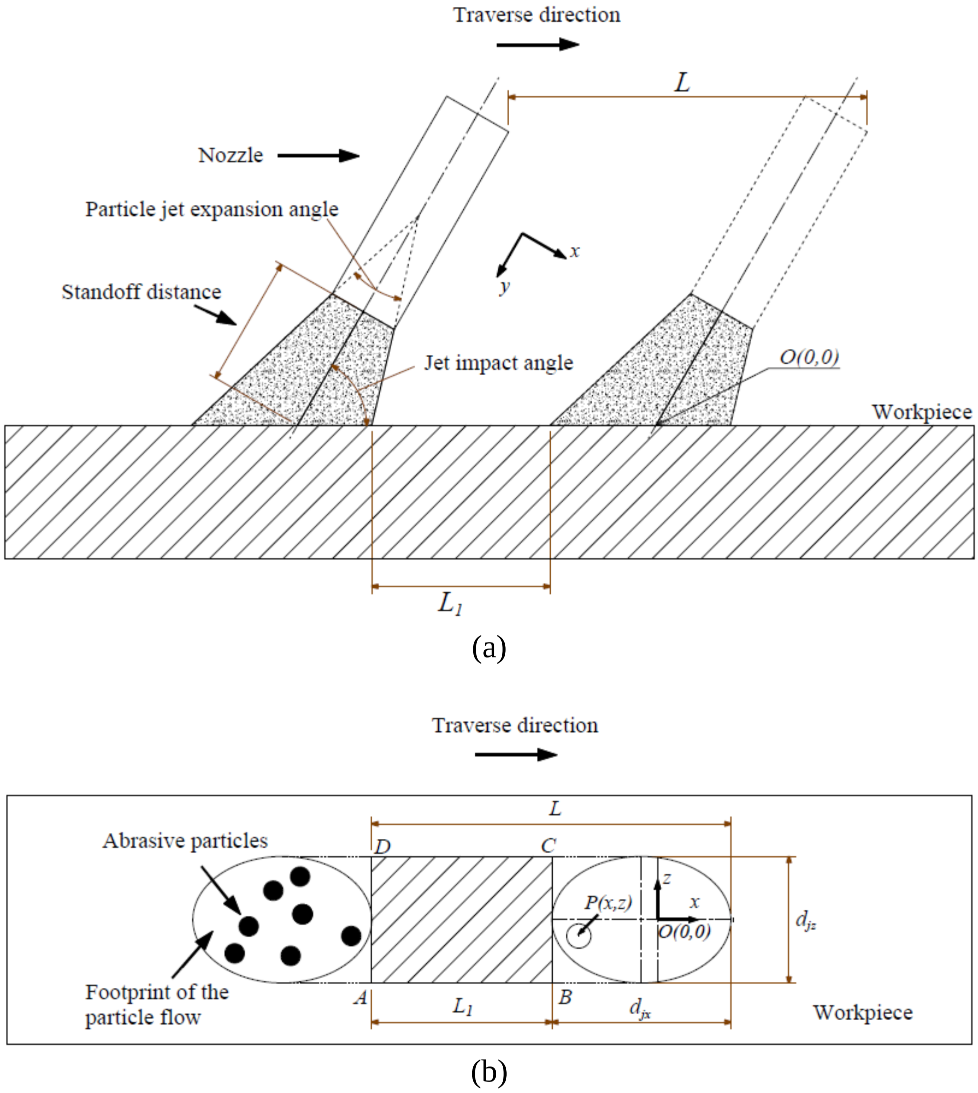

Fig. 6.1. Schematic representation of micro-channelling process by an abrasive jet: (a) relevant parameters, and (b) footprints of particle flow.

The footprint of a particle flow on the target surface is illustrated in Fig. 6.2 under the normal and oblique impact conditions. Only the particles impacting the target surface within the footprint are considered in the simulation model. For a given standoff distance (S), nozzle inner diameter (D), particle jet expansion angle (θ_p) and jet impact angle (α_j), the profile of the footprint, as shown in Fig. 6.2, can be expressed by an elliptic equation as

$$\frac{(x-K_1)^2}{\left(\frac{d_{jx}}{2}\right)^2}+\frac{z^2}{\left(\frac{d_{jz}}{2}\right)^2}=1 \tag{6.1}$$

in which K_1, d_{jx}, and d_{jz} are respectively given by

$$K_1=\frac{-\cos\alpha_j\tan\frac{\theta_p}{2}}{\sin^2\alpha_j-\cos^2\alpha_j\tan^2\frac{\theta_p}{2}}\left(\frac{D}{2}+S\tan\frac{\theta_p}{2}\right) \tag{6.2}$$

$$d_{jx}=\frac{\sin\alpha_j}{\sin^2\alpha_j-\cos^2\alpha_j\tan^2\frac{\theta_p}{2}}\left(D+2S\tan\frac{\theta_p}{2}\right) \tag{6.3}$$

$$d_{jz}=\frac{\sin\alpha_j}{\sqrt{\sin^2\alpha_j-\cos^2\alpha_j\tan^2\frac{\theta_p}{2}}}\left(D+2S\tan\frac{\theta_p}{2}\right) \tag{6.4}$$

where the origin of coordinates, *O(0,0)*, is at the intersection of the nozzle centreline and the target surface, and d_{jx} and d_{jz} are major and minor axes of the ellipse, respectively. It is noted that the ellipse is not symmetrical at the z-axis.

Thus, if a particle impacts within the footprint, its position or coordination (x, z) should satisfy the following condition:

$$\frac{(x-K_1)^2}{\left(\frac{d_{jx}}{2}\right)^2}+\frac{z^2}{\left(\frac{d_{jz}}{2}\right)^2}\le 1 \tag{6.5}$$

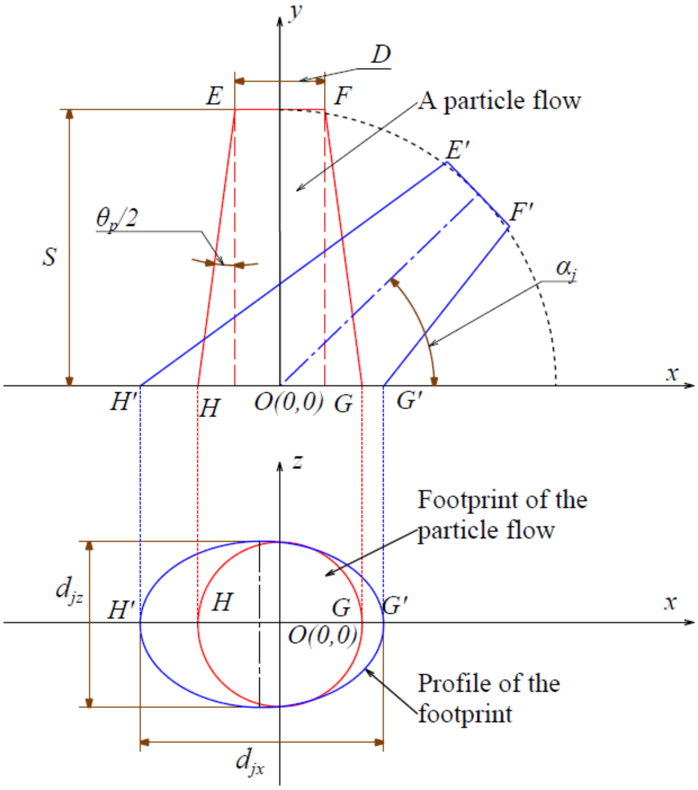

Fig. 6.2. Schematic representation of the structure of the particle flow and the corresponding footprint on the target surface at the normal jet impact angle (red lines) and oblique jet impact angle (blue lines).

During a micro-machining process, the top kerf or channel width primarily depends on the d_{jz}, while the d_{jx} affects the actual nozzle travelling distance (L) in order to achieve a complete cutting length L_1 in a relationship of

$$L = L_1 + d_{jx} \tag{6.6}$$

Considering the experimental work that is to be stated later in this chapter where alumina particles with the average diameter (d_p) of 27 µm, nozzle inlet air pressure (P_a) of 0.66 MPa, abrasive mass flow rate (m_a) of 5 mg/s, nozzle inner diameter (D) of 0.178 mm, standoff distance (S) of 0.5 mm, jet impact angles (α_j) of 30°, 60° and 90°, and nozzle traverse speeds (u) of 15, 20 and 25 mm/s are used, a relatively high nozzle traverse speed and low abrasive mass flow rate are used to reduce the number of impacting particles in the simulation. Even then, the number of impacting particles involved in a small nozzle travelling distance is still large. It can be calculated as follows.

The mass of impacting particles in per unit length of cutting, m_{pl}, is given by

$$m_{pl} = \frac{m_a}{u} \tag{6.7}$$

The mass of the impacting particles during the nozzle travelling over a distance, L, can then be found from

$$m_L = L m_{pl} \tag{6.8}$$

Since the impacting particles used in the simulation are assumed to be spherical with uniform distribution, the average mass of a single particle can be given as

$$m_p = \frac{\pi}{6} d_p^3 \rho_p \tag{6.9}$$

where d_p is the particle diameter and ρ_p is the particle density.

Hence, the total number of impacting particles, n_{pt}, during the nozzle travelling over a distance, L, becomes

$$n_{pt} = \frac{m_L}{m_p} = \frac{6Lm_a}{\pi u d_p^3 \rho_p} \tag{6.10}$$

For instance, when α_j=60° and u=15 mm/s, d_{jx} can be calculated from Eq. (6.3), which is 278 μm, and the actual machining length (L_1) in the simulation is set to be 120 μm by considering the practicality of the computation time, such that the total nozzle travelling distance (L) is 398 μm from Eq. (6.6). The total number of impacting particles required in the simulation model under this condition can be calculated from Eq. (6.10), which is 3,244.

6.2.1.2 Generation of particle flow in a layered arrangement

It is challenging to consider such a large number of impacting particles into the simulation model because this will result in a very long computation time. Two primary approaches in modelling a particle flow relevant to AWJ machining have been reported [38, 98, 99, 143, 144]. One is to arrange the impacting particles in layers, and these layers were spaced close to each other, to significantly reduce the length of the jet plume for the same amount of impacting particles considered and hence the computation time [98, 99, 143, 144]. Another way is to model the particle flow with a Monte Carlo method by considering the time intervals between successive particle impacts [38]. It has been found that for the erosion of ductile materials, the layered arrangement of impacting particles may cause a deviation in the simulation results since the particle impact process is in fact a sequential process, while the layered arrangement changes the particle inter-arrival times, which affects the target cooling process, and hence the thermal diffusion and the material removal [38].

However, it has been found that based on experimental observations [90, 91, 135], very little plastic deformation occurs on silicon or quartz during the high velocity micro-particle impact process, and material removal was mainly realized by brittle fractures. As such, thermal diffusion, which is mainly generated due to the plastic deformation during an impact process, is not considered as significant in brittle material erosion. Since thousands of impacting particles should be considered even in a small cutting distance, the impacting particles involved in the particle flow are arranged in layers in this study to reduce the computation time as in the work [98, 99].

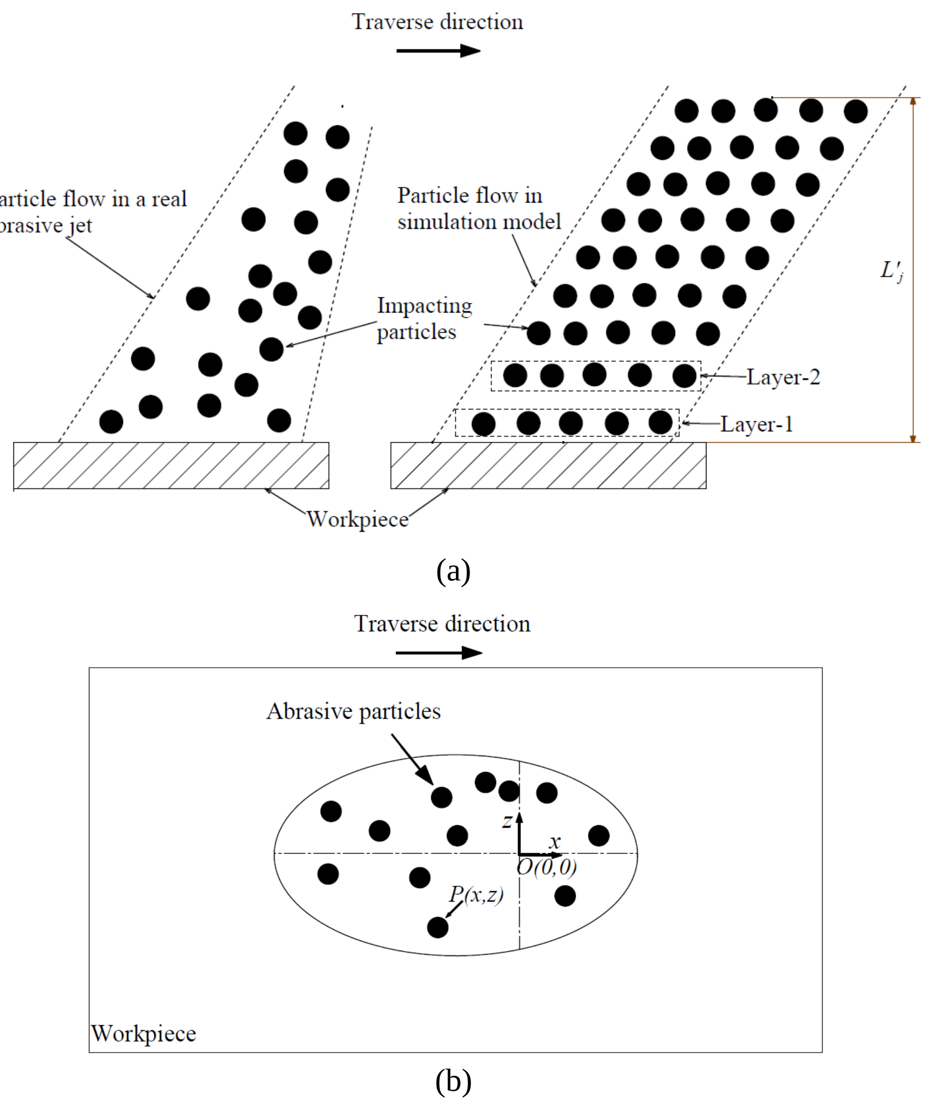

Fig. 6.3. (a) Schematic representation of the difference between the particle spatial density in a real abrasive jet and in the simulation model, and (b) Top view of the layer-1 in (a).

Fig. 6.3(a) shows the schematic illustration of the difference between how the impacting particles are spaced in a real jet and in the simulation model, where the impacting particles are distributed randomly within a real abrasive jet, but they are arranged in layers in the simulated particle flow. These layers are spaced with a short distance of 5 µm between two consecutive layers, to significantly reduce the length of the jet plume in the simulation model. The footprint of layer-1 is shown in Fig. 6.3(b) when the impacting particles approach the target surface. It is assumed that the footprint of each layer in the particle flow when approaching the target surface is the same as layer-1, and as such, the position (x, z) of any particle in each layer should satisfy the condition in Eq. (6.5).

In order to have the same number of particles impacting the target surface in the simulation and in the real jet, the traverse motion in the simulation model needs to be much faster than in the experiment due to the decrease in the length of the jet plume in the simulation model. However, if a higher traverse speed is applied, the resultant particle impact angle will deviate from the original impact angle when they impact the target surface, which may affect the erosion of brittle materials [47]. This is explained below.

As the nozzle travels over a distance, L, the total time, T_t, required by all the impacting particles to hit the target surface in simulation model is given by

$$T_t = \frac{L'_j}{v_{ap} \sin \alpha_j} \tag{6.11}$$

where L'_j is the length of the jet plume in the simulation model as depicted in Fig. 6.3(a), α_j is the jet impact angle and v_{ap} is the average particle impact velocity from nozzle exit to the target surface along the axial direction of the jet. According to the model for the particle velocities in a micro-abrasive jet [43], within a small standoff distance, the particle impact velocity varies little from the nozzle exit to the target surface along the axial direction of the jet flow, so that the average particle impact velocity is assumed to be equal to the centreline velocity at the half of the standoff distance from the nozzle exit along the axial direction of the jet flow.

If u' is used to express the traverse speed for the impacting particles in the simulation model, i.e.

$$u' = \frac{L}{T_t} \tag{6.12}$$

where L is the total nozzle travelling length, the average resultant particle impact angle (θ_R) can be obtained as

$$\theta_R = \tan^{-1}\left(\frac{\sin\alpha_j}{\frac{u'}{v_{ap}} + \cos\alpha_j}\right) \tag{6.13}$$

As an example, under the condition of α_j=60°, u=15 mm/s, S=0.5 mm and P_a=0.66 MPa, if the number of particles in each layer is set at 20, the total number of layers required in the simulation is 162. Considering that the distance between two consecutive layers is set at 5 μm, the length of the jet plume in the simulation model (L'_j) can be obtained as

5.18 mm. The average particle impact velocity (v_{ap}) under the same condition can be obtained from the model developed in [43], which is 137 m/s. Hence, from Eq. (6.11), T_t=43.66 μs. When the nozzle travelling distance (L) of 398 μm at the same condition is considered, the traverse speed for the impacting particles in simulation model (u') can be calculated from Eq. (6.12), i.e. 9.2 m/s. By substituting the values of u' and v_{ap} into Eq. (6.13), θ_R is obtained as 56.8°.

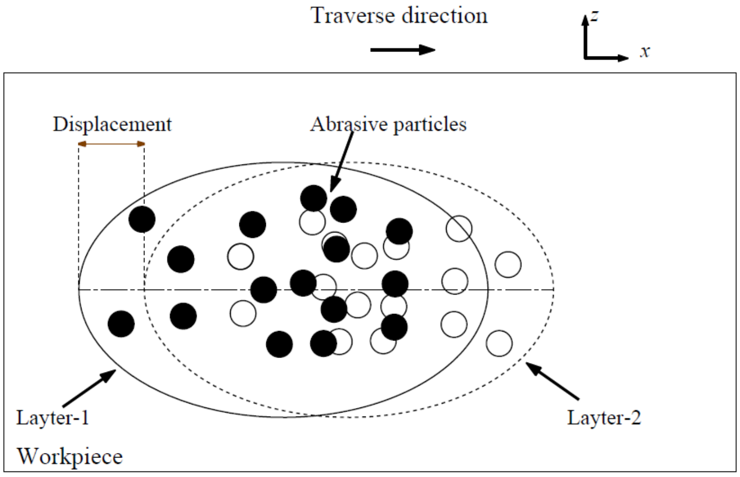

Fig. 6.4. Schematic representation of the displacement between two adjacent layers.

To overcome this issue, it is assumed that the impacting particles move in the traverse direction in steps of equal magnitude between two consecutive layers. Each step is a fixed proportion of the total nozzle travelling length (L). This can be achieved by applying a displacement boundary condition to each layer along the traverse direction. The displacement, as illustrated in Fig. 6.4, is defined as the moving distance between the adjacent layers in each step, which can be calculated from the ratio of the total nozzle travelling distance to the total number of layers required in the simulation. For example, under the condition of α_j=60° and u=15 mm/s, if the number of particles in each layer is set at 20, the total number of layers required in the simulation can be obtained, which is 162. To consider the nozzle travelling distance (L) of 398 μm at the same condition, the displacement is calculated as 2.45 μm.

In order to save computation time, additional assumptions are made for the impact process. Firstly, when the particles in the previous layer have completed the impingement and rebound away from the target surface, the particles in the next layer are generated just on the top of the solid specimen surface with a distance of 5 μm, moving by a distance equal to the programmed displacement and then impacting the target. The particle-particle collisions between the incoming particles and the rebounding particles from the previous layer are not considered in this model. Secondly, after obtaining the particle location before impact with respect to the target surface, a programme is executed to check and delete the particle from the layer if it is going to impact outside of the machining length L_1. This enables the erosion rate obtained from a small segment L_1 in the simulation model to be representative of the erosion rate obtained from a machining process, because the particles that impact outside of L_1 do not contribute to the erosion rate corresponding to L_1. In doing so, the number of particles required to be simulated in the final model is significantly reduced. For example, the above-mentioned 3,244 particles generated under the condition of α_j=60º and u=15 mm/s are reduced to about 781. This treatment is valid for small depths of cut, such as micro-machining in this study where negligible slope of the transient surface at the cutting front is formed and the actual particle impact angle is not greatly affected.

6.2.1.3 Determination of particle velocities

After the generation of particle flow, a key requisite in modelling the multiple particle impacts is to determine the particle velocities. Since it is assumed that the target is impinged by the particles layer by layer, it is only necessary to determine the velocities of impacting particles in each layer when they are going to impact the target surface. In micro-abrasive jets, the radial velocity component is much smaller than the axial velocity component, as such, in the analysis of the particle velocities, only the axial velocity component is considered [44].

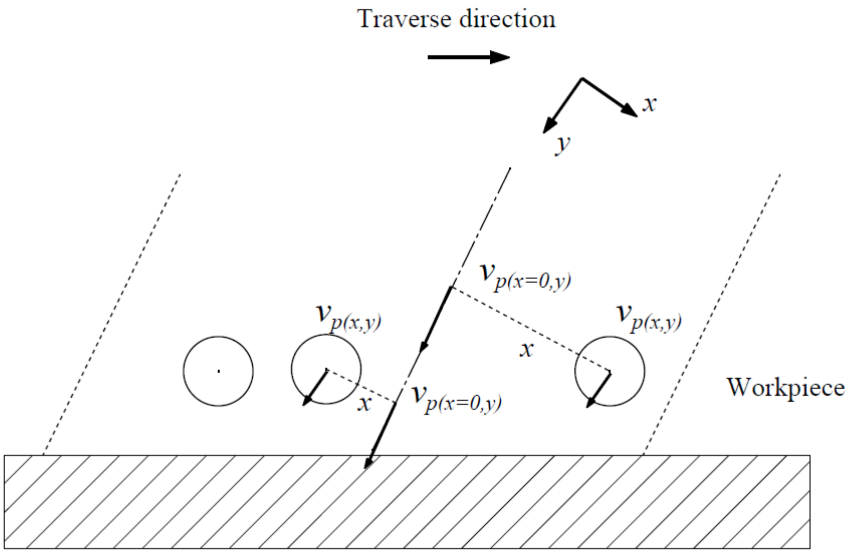

Fig. 6.5. Schematic representation of particle velocities in a micro-abrasive jet.

A mathematical model for the particle velocities in a micro-abrasive jet have been developed by Li et al. [43], where the particle velocity at the jet radial and axial position (x, y), as shown in Fig. 6.5, is given by

$$v_{p(x,y)} = v_{p(x=0,y)} \exp\left(-\ln 2 \left(\frac{x}{\frac{D}{2} + 100D \tan\frac{\theta_A}{2}} \right)^2 \right) \tag{6.14}$$

where $v_{p(x,\,y)}$ is the particle velocity at an axial distance y from nozzle exit and a radial distance x from the jet centreline, $v_{p(x=0,\,y)}$ is the centreline velocity at an axial distance y

from the nozzle exit, and θ_A is expansion angle of pure air jet flow, which is typically between 12.5º and 15º [145].

It can be seen from Eq. (6.14) that the centreline velocity ($v_{p(x=0,\ y)}$) needs to be determined first. Li et al. [43] used a numerical solution method to calculate the centreline particle velocity by dividing the nozzle and the jet flow in air into small segments along the jet axial direction. Since the standoff distance is 0.5mm, the air pressure is set at 0.66 MPa, and the nozzle inner diameter is 0.178 mm, the centreline velocity at an axial distance of 0.5 mm from the nozzle exit can be calculated from the model in [43], which is about 138 m/s. It is also noticed in Fig. 6.5 that by considering the oblique jet impact angle, the centreline velocity for particles in the same layer is different due to the varying axial distances from the nozzle exit. However, based on the model developed in [43], the centreline velocity varies only from 137 to 139 m/s when the axial distance changes from 0.3 to 0.7 mm, hence, when particles are going to impact the target surface it is reasonable to assume that the centreline velocity for every particle is the same and evaluated at the axial distance of 0.5 mm from the nozzle exit, which is 138 m/s. Then, the axial component of the particle velocities at different radial locations in the same layer can be calculated from Eq. (6.14).

6.2.2 Target solid specimen model

The target solid specimen used in this study is the same as that used in the single particle impact study as stated in Chapter 5. The target material used in this study is still a quartz crystal whose properties are given in Table 3.1. Therefore, the relevant quantities used in the BPM are determined according to the data given in Table 5.2.

The geometry of the solid specimen model is shown in Fig. 6.6. Considering the simulated machining length (L_1) of 120 μm and the maximum value of the minor axis (d_{jz}) (see Fig. 6.1(b)) of 240 μm under the jet impact angle of 30º (which gives the largest d_{jz} for all the impact angles to be considered in the model verification, which will be given later in the chapter), the solid specimen model with the dimensions of 180×280×60 μm^3, consisting of 139,037 spherical elements, is selected, which is larger than the actual machining area *ABCD* shown in Fig. 6.1(b), in order to minimise the boundary effect. The boundary conditions are as follows (see Fig. 6.6): the top face of the specimen is set free which is to be impacted by multiple particles, while spherical elements on the other five exterior faces of the specimen are set at zero freedom in both translational and angular velocities.

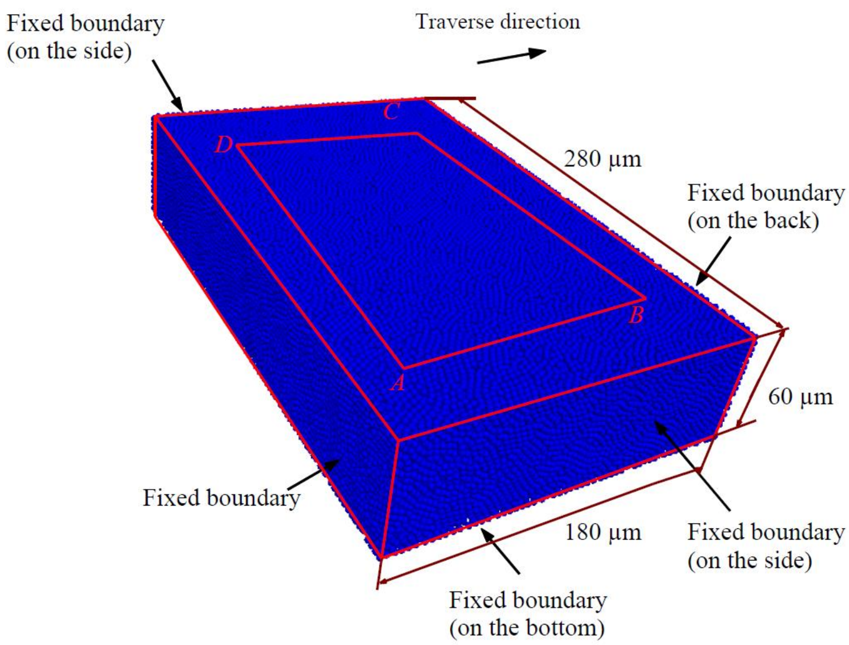

Fig. 6.6. Target geometry and boundary conditions.

6.3 Model verification

The mechanical properties of the modelled solid specimen have already been verified numerically in Chapter 5. Material numerical tests, including a compression test and a fracture toughness test, were conducted using the PFC3D software to obtain and assess these quantities of the solid specimen with respect to the corresponding physical properties of the real material. It has been found that the specimen model constructed can represent the mechanical behaviour of the quartz crystal considered. In this section, a set of abrasive air jet micro-channelling tests on quartz crystals are carried out to verify the DE model by comparing model predictions with corresponding experimental data for some easy-to-measure quantities, as detailed below.

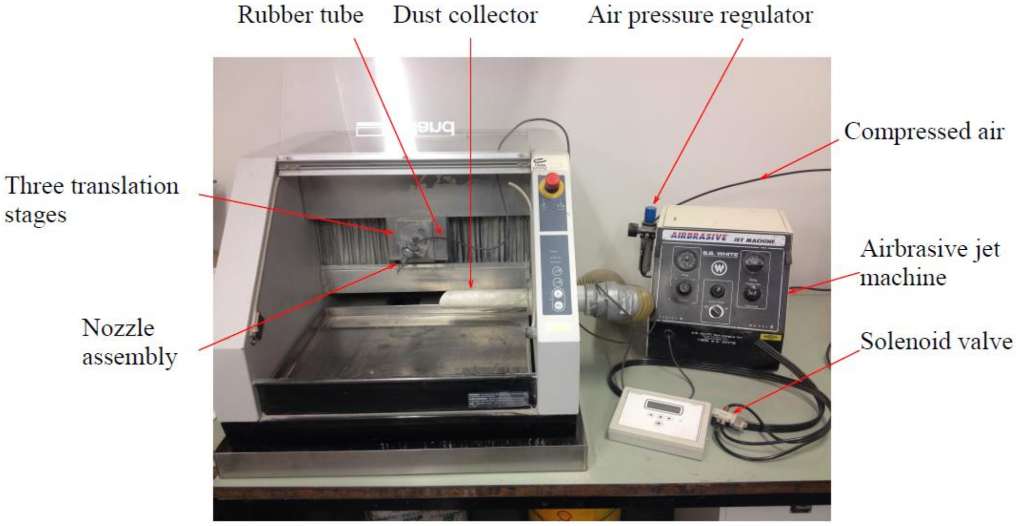

(a)

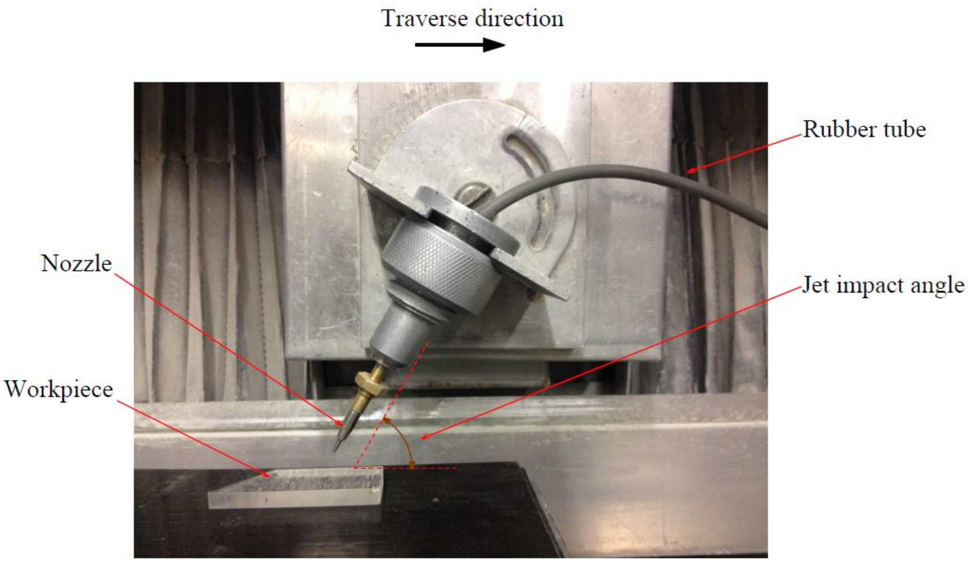

(b)

Fig. 6.7. An abrasive jet micro-machining system used for the experiment: (a) the major elements of the system, and (b) arrangement of nozzle and workpiece.

6.3.1 Experimental work

The abrasive jet micro-channelling tests were carried out on an S.S White Model K Series II Airbrasive jet machine as shown in Fig. 6.7(a). In this machine, an air compressor supplied compressed air through a single stage pressure regulator, filter and air dryer. A solenoid valve was used to precisely control the on/off switch of the air supply. The compressed air was then mixed with abrasives in a mixing chamber, which incorporated an electro-magnetic vibratory system for abrasive delivery, allowing control of the abrasive flow rate. The air-abrasive mixture was finally fed through a rubber tube into a nozzle in a large closed chamber for dust control by a dust collector. Three translation stages with the control resolution of 0.01 mm were used to move the nozzle in the X-, Y- and Z-directions. The arrangement of the nozzle and workpiece is shown in Fig. 6.7(b), in which a backward jet impact angle was used.

The major parameter settings for the test are given in Table 6.1. Nozzle standoff distance is defined as the distance between the nozzle exit and the target surface along the nozzle centreline. Alumina particles with the average diameter of 27 μm were used in the tests. In Section 3.3, the particle size distribution has been measured, which indicates that the particles with the diameter of 27 μm represent the largest proportion in volume. The average roundness of the particles has also been quantitatively assessed, which indicates that most of the particles used in the experiment were not far from a spherical ball. Hence, by assuming that the particles are spherical with uniform distribution in the simulation model, a deviation of the model prediction is expected from the experimental data.

Table 6.1. Parameter settings for the experiment.

Nozzle type	Cylindrical
Nozzle inner diameter (mm)	0.178
Nozzle length (mm)	7
Nozzle inlet air pressure (MPa)	0.66
Nozzle traverse speed (mm/s)	15, 20, 25
Jet impact angle (º)	30, 60, 90
Abrasive	Alumina
Abrasive average diameter (µm)	27
Abrasive density (kg/m^3)	3970
Abrasive flow rate (mg/s)	5
Standoff distance (mm)	0.5

With 3 levels of jet impact angle and 3 levels of nozzle traverse speed, 9 channelling test conditions were considered using a full factorial experimental design. Each channel was machined at 5 mm length and repeated at least three times. With the assistance of a Keyence VK-X200 3D laser measurement microscope, the top channel width, channel depth and material removal volume in a given length were measured. Four measurements for each channelling performance measure were carried out for each test and the average was taken as the final reading.

6.3.2 Comparison between model predicted and experimental results

The same process parameters as those in the experiment were used in the DE model, which gave 9 simulation cases for comparison with the corresponding experimental data. Fig. 6.8 presents the typical 3D views and cross-sectional profiles of the channels from the experiment and simulation. The material erosion rate, top channel width and channel depth were considered for comparisons between the experimental and model predicted values.

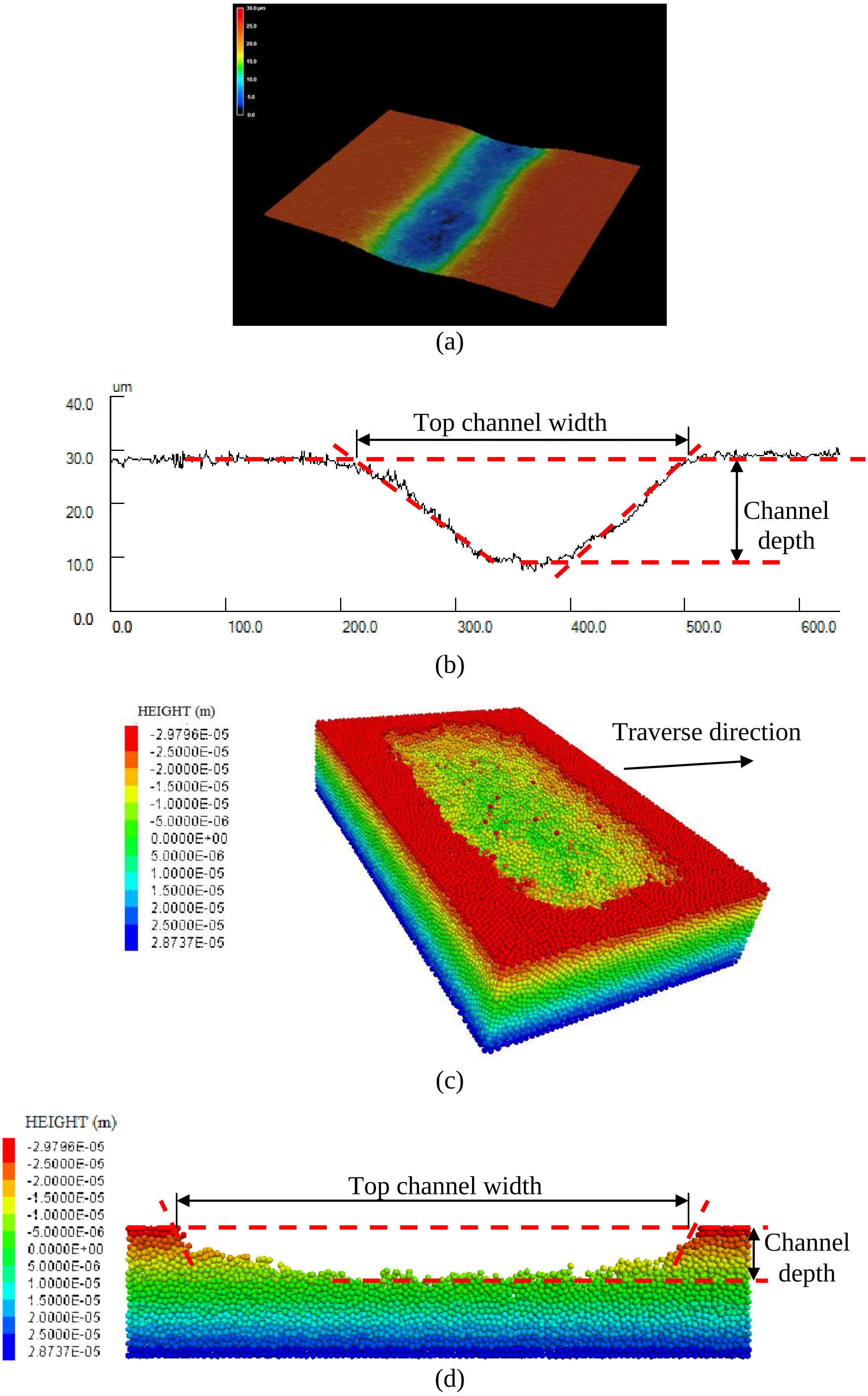

Fig. 6.8. Experimental and model predicted channel characteristics: (a) 3D view of an experimental channel, (b) cross-sectional profile of an experimental channel, (c) 3D view of a simulated channel, and (d) cross-sectional profile of a simulated channel (d_p=27 μm, P_a=0.66 MPa, α_j=90° and u=15 mm/s).

The channel depth and top channel width can be measured directly from experiment and simulation, as illustrated in Figs. 6.8(b) and (d), where the channel depth was measured along the centreline of the channel and the top channel width was defined by using the intersection of a fitted straight line with the target top surface. In addition, the material erosion rate was calculated from the material removal mass divided by the total particle mass involved in the cutting length, where the material removal mass was evaluated from the target material density and the material removal volume measured by assuming that the density of the quartz crystal in the machining zone was unchanged and constant, and the total particle mass was obtained from the abrasive mass flow rate, the cutting length and the nozzle traverse speed. Likewise, the erosion rate in the simulation was calculated as the mass of the spherical elements detached from the solid specimen divided by the mass of the impacting particles involved in the simulated machining length (L_1).

Fig. 6.9 shows that the model predictions are in agreement with the corresponding experimental data for material erosion rate, channel depth and top channel width at various conditions. It is noted that the model predicted erosion rates and channel depths are a little higher than the corresponding experimental data. This is possibly attributed to the particle-particle collisions and the particle deposition on the target surface in the experiment [120], which could reduce the material removal but were not considered in the simulation. Further, it can be seen in Fig. 6.9(c) that the average top channel width obtained from the experiment is larger than the model predictions. This is possibly attributed to the smaller particles involved which have a greater tendency for a higher plume divergence angle due to their smaller inertia [114], and as a result, the experimental channels are wider than the model predictions.

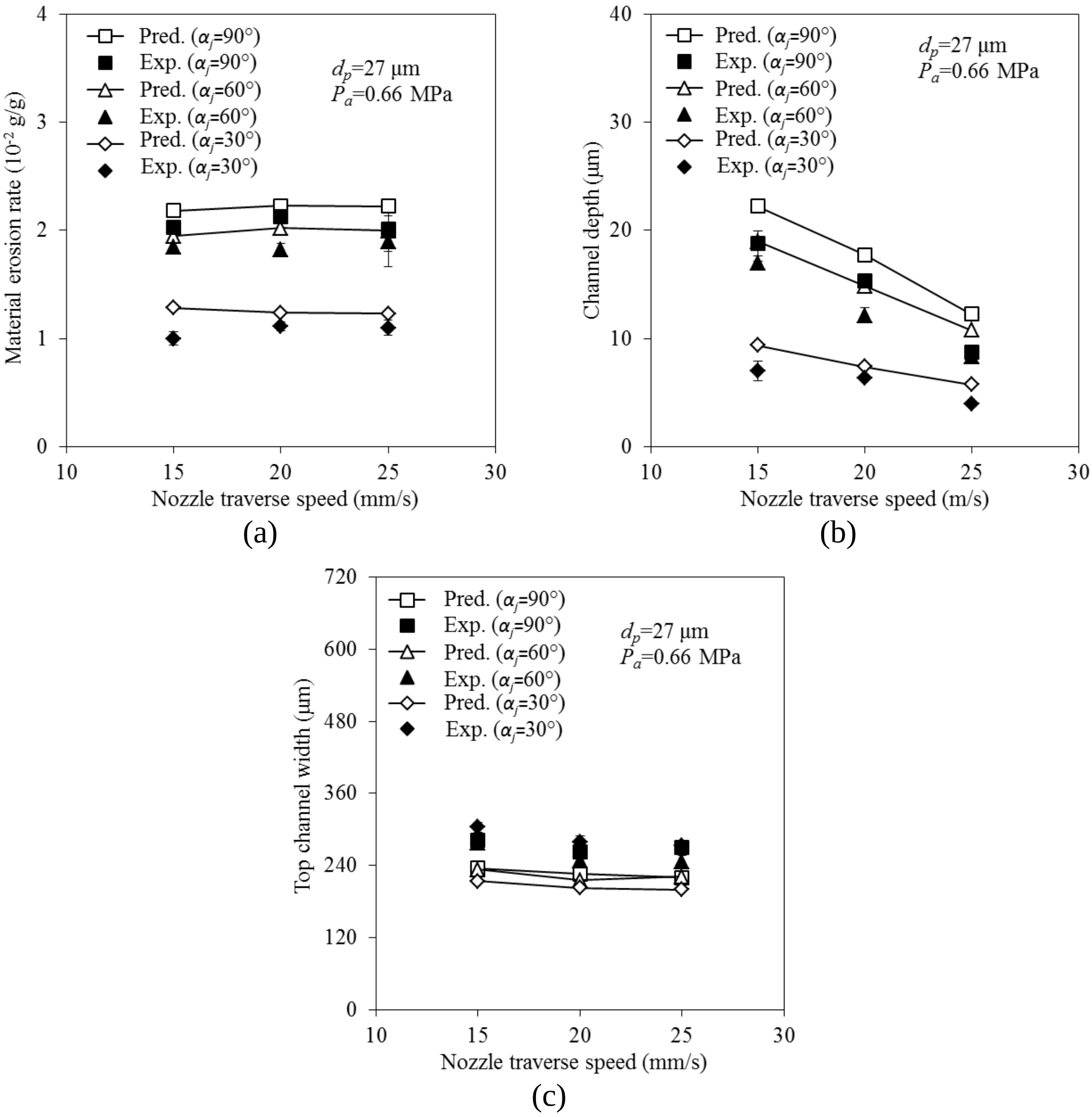

Fig. 6.9. Comparison of predicted and experimental results (error bars show the standard deviation of the experimental data).

A quantitative comparison shows that the percentage deviation of the model predicted from the experimental material erosion rate is 10.72% on average with the standard deviation of 7.16%, while the corresponding average and standard deviations for channel depths are 25.86% and 11.79%, respectively. Likewise, the average deviation for the top channel width is -19.06% with the standard deviation of 6.95%. Based on the above comparisons, it may be deduced that the model developed for multiple particle impacts has been correctly developed for use to simulate the impact process.

6.4 Simulation results and discussion

6.4.1 General observation of material removal mechanisms

In the DE model, material removal refers to detachment of the spherical elements from the solid specimen, caused by the continuous propagation and coalescence of cracks induced by impacts. Fig. 6.10 shows the material removal process under the multiple particle impacts. It has been found that with the increase in the number of impacts, cracks are initiated on the specimen surface. This includes the median cracks which propagate almost perpendicularly to the surface, and lateral cracks which propagate in parallel to the solid specimen surface as the impact event progresses, as shown in Fig. 6.10(a). Apparently, these cracks degrade the strength of the substrate and facilitate material removal in the subsequent impacts. As the number of impacts increases, new cracks are formed and intersect with the previous cracks, which cause some spherical elements to be removed from the solid specimen, as shown in Fig. 6.10(b). The removed spherical elements have breakages in all their contacts. However, there are elements that do not totally break from its adjacent elements and still belong to the solid specimen, although there are cracks around them. These cracks are eventually left on the specimen as residual cracks, as shown in Fig. 6.10(c), which contribute to the subsurface damage of the material.

The relationship between the erosion rate and the number of impacting particles under various jet impact angles is presented in Fig. 6.11 in detail. The erosion rate increases sharply with an increase in the number of impacts initially, but then the erosion rate

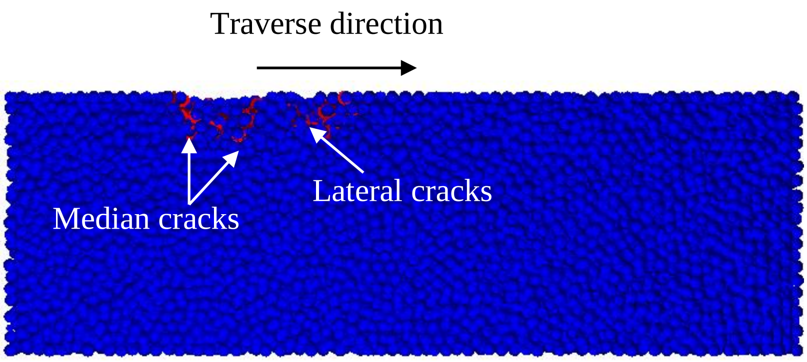

(a) Number of impacting particles: 13

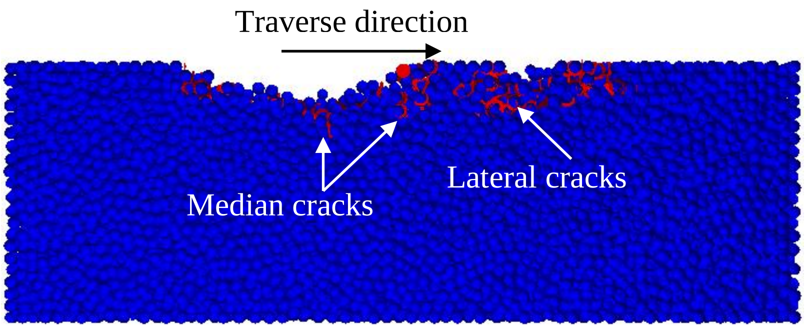

(b) Number of impacting particles: 121

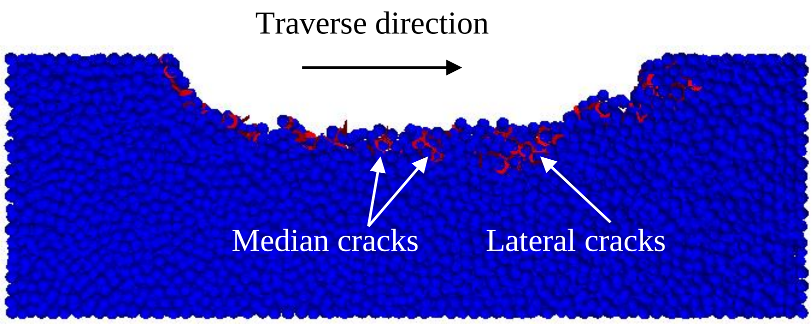

(c) Number of impacting particles: 525

Fig. 6.10. Simulated material removal process under multiple particle impacts (d_p=27 μm, P_a=0.66 MPa, α_j=90° and u=20 mm/s; red lines represent cracks).

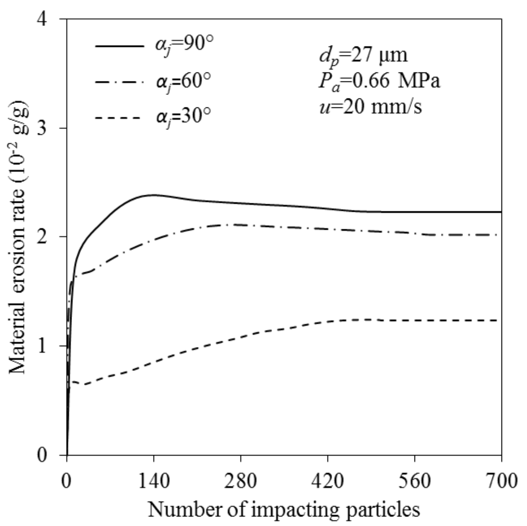

Fig. 6.11. The relationship between the erosion rate and number of impacts.

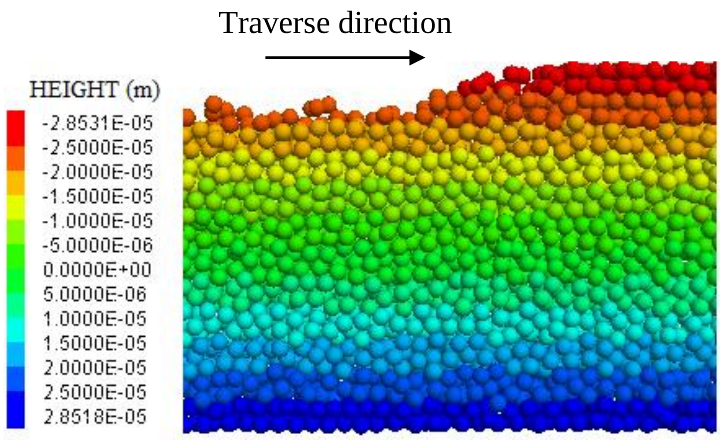

(a) α_j=30°

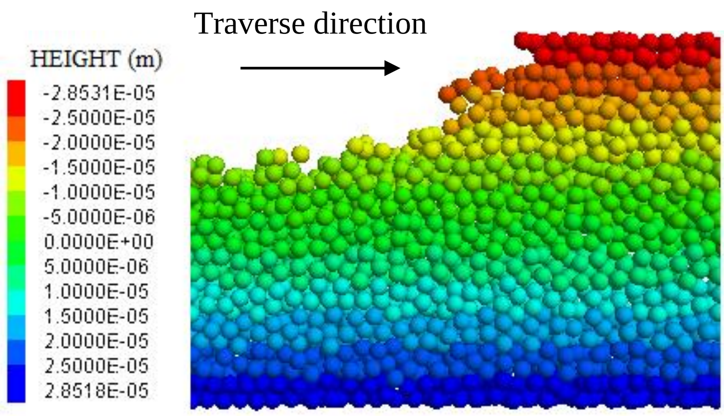

(b) α_j=60°

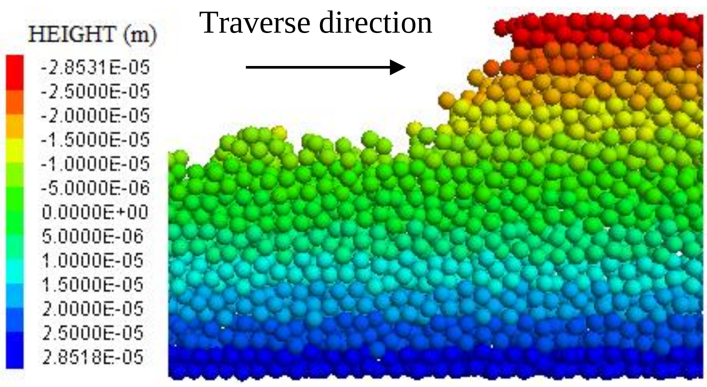

(c) α_j=90°

Fig. 6.12. The slope of the transient surface in the cutting front under various jet impact angles (d_p=27 μm, P_a=0.66 MPa, and u=20 mm/s).

increases steadily until up to its maximum before it decreases slightly to somewhat a steady state. This trend is more apparent by using larger jet impact angles of 60° and 90°, but with the smaller jet impact angle of 30°, the erosion rate increases almost monotonically after an initial sharp increase. This trend can probably be attributed to the slope of the transient surface at the cutting front, as shown in Fig. 6.12. In the impact process, only particles inside the simulated machining length are considered, so that at the end of the impacts by one or more layer of particles, a transient surface is formed after the material removal, which has a slope to affect the actual impact angle of the impacting particles in the front part. Due to the small depth of cut (about 8 μm) at the small jet impact angle of 30°, the actual particle impact angles are not greatly affected by the orientation of the transient surface. However, the slope of the transient surface seems to be steeper under larger jet impact angles, as shown in Figs. 6.12(b) and (c), so that the actual impact angles of the incoming particles may be deviated from the original angles, which may reduce the material erosion rate. This appears to be obvious for brittle material erosion using a backward jet impact angle.

6.4.2 Effect of overlapping impact on material removal

Since the overlapping condition between successive impacts is an important parameter in the multiple particle impact process, it is essential to understand how the impact overlapping condition affects the material removal. For this purpose, an impact distance ratio, φ, is introduced to account for the overlapping condition between the first and second impact location, i.e.

$$\varphi = \frac{l}{r_p} \tag{6.15}$$

where l is the distance between the two successive impacting particles in a plane parallel to the target surface, and r_p is the particle radius, as shown in Fig. 6.13. From this definition, a smaller φ represents a larger overlap, and vice versa. For simplicity, only the overlap along one dimension is considered, and φ is chosen to be 0, 0.5, 1, 1.5 and 2, respectively, where φ=0 represents the case in which the second particle impacts at the same location as the first one, while φ=2 implies that there is no overlap between the two impacts.

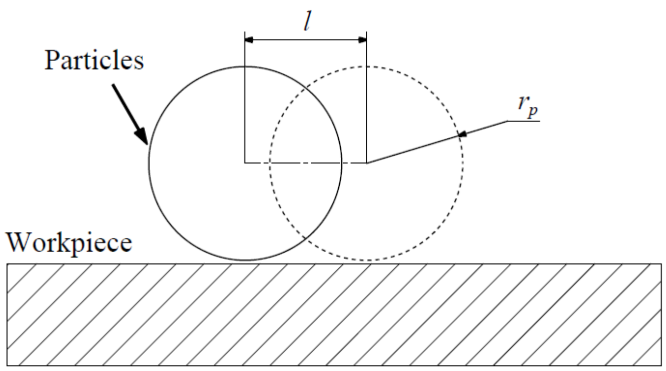

Fig. 6.13. Definition of impact distance ratio between two successive impacts.

Fig. 6.14 shows the relationship between the impact overlapping condition and material erosion rate under different particle impact angles. It is noticeable that material erosions in the first and second impact are essentially the same when the overlapping condition is 1.5 or more. The small difference in material erosion at φ=2 where there is no impact overlap is attributed to the random distribution of the spherical elements in the model which may yield different ways of formation and propagation of cracks and hence little difference in the material erosion from the first impact. However, a significant increase in material erosion can be noticed when φ is less than 1.5. It follows that at a large impact distance (e.g. $\varphi \geq 1.5$), the strength degradation and residual cracks from the first impact do not contribute significantly to the erosion in the second impact and hence the erosion rate. By contrast, at a smaller impact distance, the effect of the first impact accumulates with the second impact through strength degradation and the coalescent of cracks, which causes more material removal.

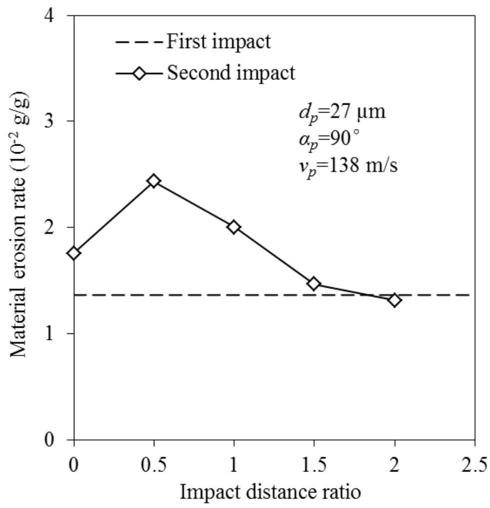

(a)

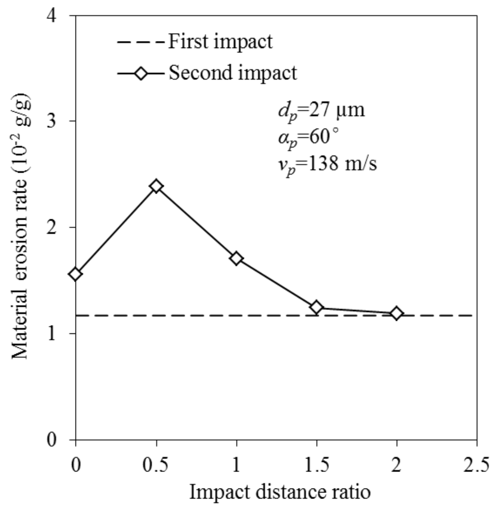

(b)

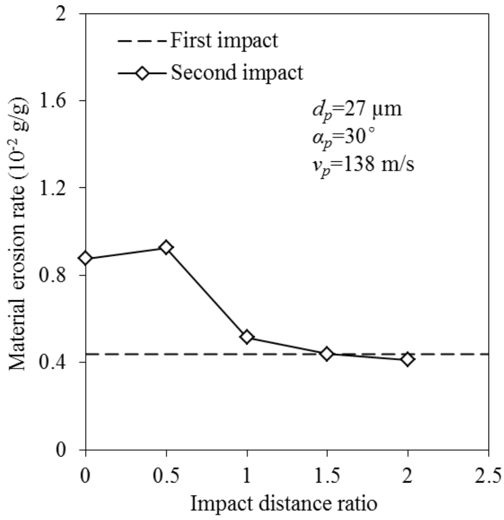

(c)

Fig. 6.14. Effect of impact overlapping condition on the material erosion rate under different particle impact angles.

It is interesting to note in Fig. 6.14 that the maximum erosion rate in the second impact occurs at φ=0.5, rather than at φ=0. The underlying reason for this is possibly attributed to the number of cracks formed in the second impact, as shown in Fig. 6.15. When φ=0.5, the number of cracks caused by the second impact is much greater than that at φ=0. It is due to the fact that after the first impact, the residual cracks left in the crater lip cause significant surface strength degradation at that region which facilitates the material removal in the subsequent impact. When φ=0.5, the centre of the second impact is close to the crater lip and more material is removed. Thus, the second impact with a relatively smaller impact distance ratio (larger overlapping condition) from the first impact can significantly enhance the material removal under both normal and oblique impacts.

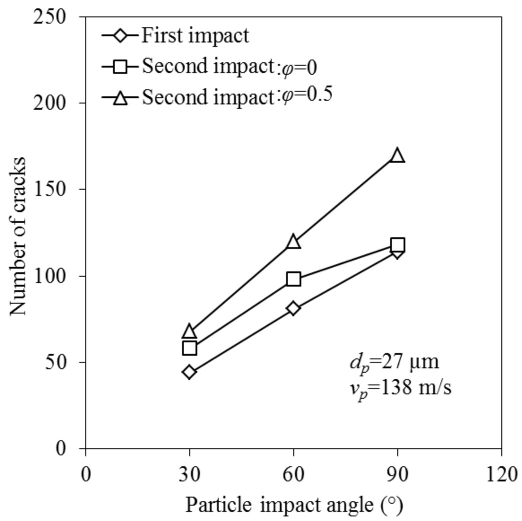

Fig. 6.15. Effect of impact overlapping condition on the number of cracks formed in the second impact.

6.4.3 Effect of process parameters on subsurface damage

A major concern of machining brittle materials is the subsurface damages caused by the process itself. Micro-cracks are one type of such subsurface damages, which can significantly reduce the functionality and reliability of the products. The number of residual cracks and the maximum depth of the cracked (or damaged) layer found from the simulation study are used as the criteria for assessing subsurface damages.

Fig. 6.16 shows the cracks that remain in the specimen after the impact process under various jet impact angles. By using smaller jet impact angles, fewer residual cracks are left and most of them are at close to the machined surface, as shown in Fig. 6.16(a). As the impact angle increases, the residual cracks appear to increase in number and deeper inside the specimen surface (Fig. 6.16(b)). It can be noticed that at the normal jet impact angle, a large number of residual cracks exist and remain in the deep layer of the solid specimen, as shown in Fig. 6.16(c).

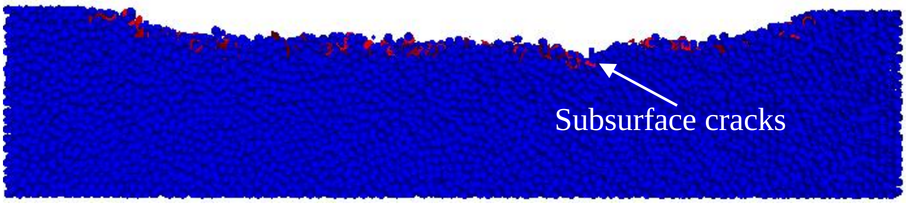

(a) α_j=30° (Maximum depth of subsurface damage: 3.63 μm)

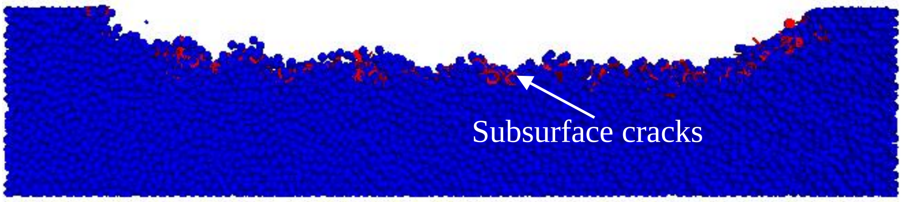

(b) α_j=60° (Maximum depth of subsurface damage: 4 μm)

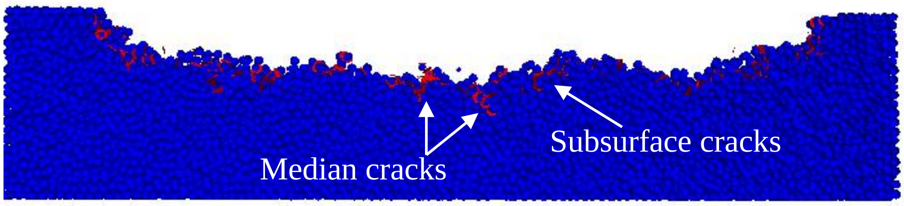

(c) α_j=90° (Maximum depth of subsurface damage: 4.85 μm)

Fig. 6.16. Residual cracks after multiple particle impacts under different jet impact angles (d_p=27 μm, P_a=0.66 MPa, and u=15 mm/s; red lines represent cracks).

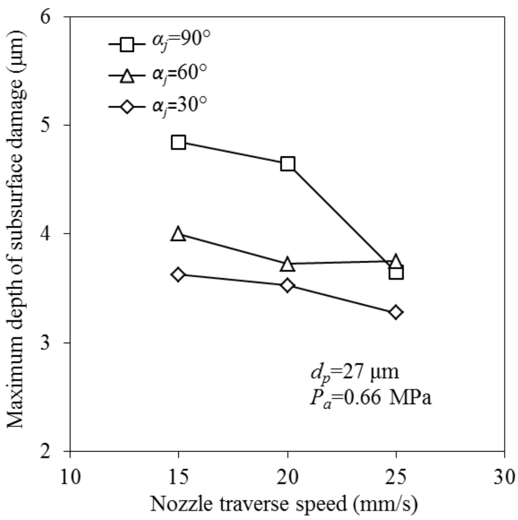

Fig. 6.17. Effect of nozzle traverse speed on the depth of simulated subsurface damage under different jet impact angles.

Fig. 6.17 shows the relationship between the maximum depth of subsurface damage with respect to the simulated process variables. Four measurements of the maximum depth of the damaged layer in four channel cross-sections along the channel were taken for each simulated channel and the average was taken. It is indicated that the depth of subsurface damage decreases with an increase in the nozzle traverse speed. This is due to the fact that fewer particles impacting the solid specimen in a higher traverse speed result in fewer residual cracks, and therefore a smaller depth of the subsurface damaged layer. Furthermore, it is noticed that increasing the jet impact angle results in an increase in the depth of the damaged layer. This may be due to the fact that a larger jet impact angle is associated with more impact force normal to the specimen surface, so that the impact involves less cutting action and forms more cracks towards the bulk of the specimen. It has been found from the simulation that a smaller jet impact angle with a faster nozzle traverse within the ranges considered in this study may be used to reduce the subsurface damage, but this is at the sacrifice of material erosion rate.

6.5 Concluding remarks

In this chapter, the DE model for single particle impact developed in Chapter 5 has been extended to allow for high velocity multiple micro-particle impacts, in which the particle flow has been represented by layered layout within the jet to reduce the computation time. Particle jet expansion angle was also considered in order to realistically consider the structure of the particle flow. While the target solid specimen model was considered in the same way as for the single impact study in Chapter 5, a relatively large rectangle target solid specimen was used in order to minimise the boundary effect in the multi-impact study.

A micro-channelling experiment on a quartz crystal using an abrasive airjet has been carried out to verify the DE model by comparing the model predictions with corresponding experimental data for the material erosion rate, top channel width and channel depth. The model predictions have shown agreement with the overall trend with the corresponding experimental data for the major micro-channelling performance measures under various conditions, while a quantitative assessment has shown that both the mean and standard deviations of the model predictions from the experimental data are small and acceptable.

Using the developed DE model, an investigation into the multiple particle impact process has been conducted. It has been found that median and lateral cracks were initiated soon after the impact process starts, which degrade the strength of the substrate material and facilitate material removal in the subsequent impacts. As the impact event progresses, more cracks are formed which propagate and intersect with the cracks formed previously, so that spherical elements start to be removed when their contacts with all their adjacent elements are broken. It has been found that, in general, the material erosion rate in the second impact is larger than the first impact when the impact distance ratio is within 1.5, and the maximum erosion rate in the second impact occurs at the impact distance ratio of 0.5 rather than at the fully overlapping location. At the end of the impact process, residual cracks have been found in the specimen under the newly formed surface. It has been shown that larger impact angles or slower nozzle traverse speeds result in an increase in the subsurface damage as represented by the number of residual cracks and the thickness of the cracked layer on the machined surface. As such, a smaller jet impact angle with a faster nozzle traverse speed within the range considered in this study may be used to reduce the subsurface damage, but this is at the sacrifice of the material erosion rate.

Chapter 7

Final Conclusions and Future Work

7.1 Final conclusions

The major objectives of this project are to investigate the micro-channelling process and performance for brittle materials by an AWJ, develop mathematical models for estimating the major micro-channelling performance measures, and study the associated impact erosion mechanisms by high velocity micro-particles. The objectives have been fully achieved through the work presented in this thesis as summarised below.

From the extensive literature review conducted in this study, it has been identified that micro-machining is in high demand by the manufacturing industry and the micro-machining technologies currently being employed cannot meet the needs of the industry. AWJ machining has been found to possess distinct advantages in processing a variety of materials, especially difficult-to-machine materials, and is a promising technology for micro-machining applications. Some studies have been carried out to understand the AWJ micro-machining process mostly using a relative low pressure ASJ. However, limitations have also been identified and further efforts are required to enhance its micro-machining efficiency and performance, e.g. the machined surface quality. Furthermore, the review has identified the pressing need to understand the erosion process and material removal mechanisms by the impact of high velocity micro-particles on brittle material to guide the development of this micro-machining technology.

An experimental study has been undertaken on the machining of micro-channels into a quartz crystal using an ASJ. It has been found that the cross-section of the channel exhibits a U-shaped profile and no large wavy pattern on the bottom surface of the channel is discernible.

An ANOVA was performed to identify the primary variables that significantly affect micro-channelling performance, such as the channel bottom surface roughness, MRR, channel depth, top channel width and channel wall inclination angle. An analysis was then carried out to investigate the effect of the major process parameters on the various micro-channelling performance measures. It has been found that within the tested ranges in this study, a combination of high water pressure and particle concentration, large abrasive particles and jet impact angle, and low nozzle traverse speed may be used to increase the MRR and channel depth, while a combination of low water pressure and particle concentration, small abrasive particles and jet impact angle, and fast nozzle traverse speed is recommended to reduce the surface roughness, although this is at the sacrifice of MRR and channel depth.

The impact erosion process by high velocity micro-particles on a quartz crystal has also been studied experimentally. By analysing the morphology of the eroded surface, three types of impressions have been identified, namely craters, scratches and micro-dents. It has been found that craters caused by brittle conchoidal fractures are responsible for instant material removal and dominate the erosion process, while micro-dents and scratches make only a minor contribution to material removal. Based on the craters formed, it has been shown that an increase in either the particle impact angle or velocity increases the volume of the craters formed by individual particle impacts.

Predictive models for the major micro-channelling performance measures have been developed in order to effectively control and optimise the ASJ micro-channelling process. A dimensional analysis technique was employed to develop the models for the MRR and channel wall inclination angle, where the coefficients in the models were determined from the experimental data, and regression analysis was used to establish the model for the top channel width. The model for the maximum channel depth was derived from the models for the MRR and top channel width based on an idealised cross-sectional profile of the channels. The developed models were then verified both qualitatively and quantitatively using a model verification experiment. It has been shown that the model predictions are in good agreement with the corresponding experimental data.

In order to understand the high velocity micro-particle impact process, the response of the target material to the impact and the associated material removal mechanisms under both the single impact and multiple impact conditions have been studied. A DE model was first developed for studying the single micro-particle impact process. The BPM was used to construct a relatively large rectangle target in order to minimise the boundary effect. This model has been verified both numerically and experimentally. It has then been used to simulate, and give an insight into, the impact process under various conditions. It has been found that micro-cracks on the target are initiated by high shear stresses and in the progress of the impact event, both median and lateral cracks are formed in the deep layer of the solid specimen, more by tensile stresses than shear stresses. Material removal is mainly caused by the propagation and intersection of micro-cracks. It has further been found that 60-88% of particle energy is consumed for crack formation and propagation in the target, and frictional loss through relative particle-target sliding accounts for 10-35% of the particle energy. Further, it has been shown that a smaller impact angle with a lower particle velocity within the ranges considered in this study yields less subsurface damage to the target.

The DE model for a single impact has then been extended to the multiple micro-particle impact process incorporating a particle flow model in which the particles involved in the particle flow were arranged in layers to reduce computational time. The developed model was verified by a set of abrasive jet micro-channelling tests on quartz crystals. It has been found that the median and lateral cracks were formed during the impact process which degrade the strength of the substrate and facilitate material removal in the subsequent impacts. As the impact event progresses, more spherical elements were removed from the solid specimen due to the repeated impacts. It has further been found that a relatively larger overlapping condition between successive particle impacts is more efficient in material removal for both normal and oblique impact angles, but the total overlapping does not yield high MRR. Furthermore, the effect of jet impact angle and nozzle traverse speed on the material erosion rate and subsurface damage has been investigated. It has been found that a smaller jet impact angle with a faster nozzle traverse speed within the ranges considered in this study may be used to reduce the subsurface damage as represented by the maximum thickness of the damaged layer, but at the sacrifice of the material erosion rate.

In summary, the work reported in this thesis has made the following contributions:

- A deeper understanding of the ASJ micro-channelling process on quartz crystals has been made. It has been shown that ASJ machining is a capable technology for micro-machining of brittle materials with good machining rates and acceptable surface quality. It has also revealed that craters caused by brittle conchoidal fractures are responsible for instant material removal and dominate the erosion process.
- Predictive models for the major micro-channelling performance measures, such as MRR, channel depth, top channel width and channel wall inclination angle, have been developed and experimentally verified. These models provided a unique means for an adequate estimation of the micro-channelling performance measures for the effective planning and control of ASJ micro-machining of quartz crystals.
- A computational model has been developed to represent the erosion process by the impact of a micro-particle on a quartz crystal and was used to provide a fundamental understanding of the impact event and material removal process, such as the initiation and propagation of micro-cracks, the energy consumption during an impact, and the subsurface damage induced by an impact, which are impossible or difficult to obtain experimentally. It has revealed that most of the particle energy is consumed for crack formation and propagation in the target and the initiation of micro-cracks during an impact is attributed to shear stresses, while tensile stresses create more lateral and median cracks in the deeper layer of the target than shear stresses.
- A comprehensive understanding of the multiple micro-particle impact process on a quartz crystal has been achieved through a numerical simulation study. The study has re-confirmed that the median and lateral cracks created by the shear and tensile

stresses during the impact process degrade the strength of the material in its deeper layer and facilitate material removal in the subsequent impacts. It has been identified that the best impact overlapping condition is not at the full overlapping with a previous impact, but at where the impact centre is at the previous formed crater lip to yield the maximum MRR.

7.2 Proposed future work

From the investigations carried out and reported in this thesis, a few possible future avenues of research derived immediately from this work can be suggested.

In order to increase the machining efficiency of this technology, further hardware development would be required. While the ASJ system developed in this study is adequate for experimental purposes, it has limitations in both total machining time in one slurry loading and slurry reloading time. A two-chamber design may be used to quickly and smoothly switch between the chambers containing abrasive slurry to improve the machine. When one chamber is in use, the abrasive bladder in the other chamber can be refilled. In addition, a vibration or stirring system may be designed to prevent the setting of slurry particles inside the bladder, while at the same time not causing fluctuation of the process parameters for high quality machining. More wear-resistant nozzles may also be an avenue for investigation.

Investigations into machining performance over a wider range of materials and process parameters should be considered. This study has demonstrated that AWJ micro-machining technology is capable of performing micro-channels on a quartz crystal without inducing heat damage. However, materials used in the semi-conductor industry, such as Germanium and Silicon, suffer greatly from damages by lasers or other micro-machining techniques. AWJ micro-machining may be an effective and viable alternative for processing these advanced materials. The effect of a wide range of process variables on the machining performance should also be investigated. For instance, this study included backward jet impact angles to improve the machined surface quality, and the effect of forward jet angles warrants further investigation.

The computational study of single and multiple particle impacts considered spherical particles only and this may be extended to other shapes of particles to make the study more relevant in practice. Likewise, since the distribution of the impacting particles involved in the particle flow has been simplified to reduce computation time, a more accurate model that considers the particle shape, particle size variation and particle distribution in the particle flow may be developed to more realistically represent the impact process. The simulation study considered a small number of variables and a further study may look into the effect of more variables in a wider range, such as particle velocities.

References

[1] J. Fukuda, Micro Mechanical Systems Principles and Technology, Elsevier Science, Amesterdam, The Netherlands, 1998.

[2] M.J. Madou, Fundamentals of Microfabrication, CRC Press, Boca Raton, Florida, United States, 2001.

[3] J. Wang, Abrasive Waterjet Machining of Engineering Materials, Trans Tech Publications, Uetikon-Zuerich, Switzerland, 2003.

[4] A.W. Momber, R. Kovacevic, Principles of Abrasive Water Jet Machining, Springer-Verlag, London, UK, 1998.

[5] D.S. Miller, Micromachining with abrasive waterjets, Journal of Materials Processing Technology, 149 (1-3) (2004) 37-42.

[6] H.T. Liu, Waterjet technology for machining fine features pertaining to micromachining, Journal of Manufacturing Processes, 12 (1) (2010) 8-18.

[7] J. Wang, T. Nguyen, K.L. Pang, Mechanisms of microhole formation on glasses by an abrasive slurry jet, Journal of Applied Physics, 105 (4) (2009) 044906.

[8] K.L. Pang, T. Nguyen, J.M. Fan, J. Wang, Modelling of the micro-channelling process on glasses using an abrasive slurry jet, International Journal of Machine Tools and Manufacture, 53 (1) (2012) 118-126.

[9] V.K. Jain, Micromanufacturing Processes, CRC Press, Boca Raton, Florida, United States, 2012.

[10] X.X. Li, J.H. Wang, W. Li, Current state and prospect of micro-machining, in IEEE International Conference on Automation and Logistics, Jinan, China, 2007, pp. 1414-1419.

[11] F.Z. Fang, H. Wu, X.D. Liu, Y.C. Liu, S.T. Ng, Tool geometry study in micromachining, Journal of Micromechanics and Microengineering, 13 (5) (2003) 726-731.

[12] I. Tansel, O. Rodriguez, M. Trujillo, E. Paz, W. Li, Micro-end-milling-I. wear and breakage, International Journal of Machine Tools and Manufacture, 38 (12) (1998) 1419-1436.

[13] Y.C. Lee, C.Y. Wu, Excimer laser micromachining of aspheric microlenses with precise surface profile control and optimal focusing capability, Optics and Lasers in Engineering, 45 (1) (2007) 116-125.

[14] R.S. Patel, J.M. Bovatsek, High speed micromachining with high power UV laser, in Proceedings of SPIE. San Francisco, California, United States, 2013.

[15] V. Tangwarodomnukun, J. Wang, C.Z. Huang, H.T. Zhu, An investigation of hybrid laser-waterjet ablation of silicon substrates, International Journal of Machine Tools and Manufacture, 56 (2012) 39-49.

[16] D. Gurguí, E. Vázquez, I. Ferrer, Influence of the process parameters to manufacture micro-cavities by electro discharge machining (EDM), Procedia Engineering, 63 (0delete) (2013) 499-505.

[17] C.M. Wang, X.Y. Chu, G. Liu, K. Zhu, Y.Q. Hong, G.X. Chi, The design of integrated route in micro-EDM, Materials and Manufacturing Processes, 28 (12) (2013) 1348-1355.

[18] C. Diver, J. Atkinson, H.J. Helml, L. Li, Micro-EDM drilling of tapered holes for industrial applications, Journal of Materials Processing Technology, 149 (1-3) (2004) 296-303.

[19] M.D. Nguyen, Y.S. Wong, M. Rahman, Profile error compensation in high precision 3D micro-EDM milling, Precision Engineering, 37 (2) (2013) 399-407.

[20] J. Fleischer, T. Masuzawa, J. Schmidt, M. Knoll, New applications for micro-EDM, Journal of Materials Processing Technology, 149 (1-3) (2004) 246-249.

[21] H.T. Ting, K.A. Abou-El-Hossein, H.B. Chua, Review of micromachining of ceramics by etching, Transactions of Nonferrous Metals Society of China, 19 (2009) S1-S16.

[22] T. Masuzawa, State of the art of micromachining, CIRP Annals-Manufacturing Technology, 49 (2) (2000) 473-488.

[23] J. Wang, Abrasive waterjet machining of polymer matrix composites-cutting performance, erosive process and predictive models, International Journal of Advanced Manufacturing Technology, 15 (10) (1999) 757-768.

[24] M. Hashish, Trends and cost analysis of AWJ operation at 600 MPa pressure, Journal of Pressure Vessel Technology-Transactions of the ASME, 131 (2) (2009) 021410.

[25] Y. Ali, J. Wang, Impact Abrasive Machining, in Machining with Abrasives, M.J. Jackson, J.P. Davim (Editors), Springer-Verlag, New York, United States, 2011, pp. 385-419.

[26] M. Hashish, Comparative-evaluation of abrasive liquid jet machining systems, Journal of Engineering for Industry-Transactions of the ASME, 115 (1) (1993) 44-50.

[27] C. Brandt, H. Louis. Profiling with 400 MPa fine-beam abrasive water jet, in 10th American Waterjet Conference, Houston, Texas, United States, 1999.

[28] K. Yanagida. Flow characteristics of water jets, in Proceedings of the Second International Symposium on Jet Cutting Technology, Cambridge, Granfield, 1974.

[29] M. Hashish, M.P. duPlessis, Prediction equations relating high-velocity jet cutting performance to stand off distance and multipasses, Journal of Engineering for Industry-Transactions of the ASME, 101 (3) (1979) 311-318.

[30] M. Hashish, Characteristics of surfaces machined with abrasive-waterjets, Journal of Engineering Materials and Technology-Transactions of the ASME, 113 (3) (1991) 354-362.

[31] J.A.C. Humphrey, Fundamentals of fluid motion in erosion by solid particle impact, International Journal of Heat and Fluid Flow, 11 (3) (1990) 170-195.

[32] Y. Kusano, I.M. Hutchings, Modelling the entrainment and motion of particles in a gap: application to abrasive wear, Proceedings of the Institution of Mechanical Engineers Part J: Journal of Engineering Tribology, 217 (J6) (2003) 427-433.

[33] H. Liu, J. Wang, R.J. Brown, N. Kelson, Computational fluid dynamics (CFD) simulation of ultrahigh velocity abrasive waterjet, Key Engineering Materials, 233-236 (2003) 477-482.

[34] H. Liu, J. Wang, N. Kelson, R.J. Brown, A study of abrasive waterjet characteristics by CFD simulation, Journal of Materials Processing Technology, 153-154 (2004) 488-493.

[35] J. Wang, H. Liu, Mathematical models for the hydrodynamic characteristics of abrasive waterjets, Key Engineering Materials, 291-292 (2005) 459-464.

[36] J. Wang, Particle velocity models for ultra-high pressure abrasive waterjets, Journal of Materials Processing Technology, 209 (9) (2009) 4573-4577.

[37] W.Y. Li, J. Wang, H.T. Zhu, H.Z. Li, C.Z. Huang, On ultrahigh velocity micro-particle impact on steels-a single impact study, Wear, 305 (1-2) (2013) 216-227.

[38] W.Y. Li, J. Wang, H.T. Zhu, C.Z. Huang, On ultrahigh velocity micro-particle impact on steels-a multiple impact study, Wear, 309 (1-2) (2014) 52-64.

[39] W.L. Chen, E.S. Geskin. Measurement of the velocity of abrasive waterjet by the use of laser transit anemometer, in Proceedings of 10th International Symposium on Jet Cutting Technology, Amsterdam, The Netherlands, 1990.

[40] M. Annoni, L. Cristaldi, M. Norgia, C. Svelto, Measurement of water jet velocity distribution using laser velocimetry, IEEE Transactions on Instrumentation and Measurement, 57 (8) (2008) 1524-1528.

[41] M. Annoni, L. Cristaldi, M. Norgia, C. Svelto, Efficiency measurement of water jet orifices by a novel electrooptical technique, IEEE Transactions on Instrumentation and Measurement, 57 (1) (2008) 48-54.

[42] M. Raffel, C.E. Willert, S.T. Wereley, J. Kompenhans, Particle Image Velocimetry: a Practical Guide, Springer-Verlag, London, UK, 2007.

[43] H.Z. Li, J. Wang, J.M. Fan, Analysis and modelling of particle velocities in micro-abrasive air jet, International Journal of Machine Tools and Manufacture, 49 (11) (2009) 850-858.

[44] J.M. Fan, H.Z. Li, J. Wang, C.Y. Wang, A study of the flow characteristics in micro-abrasive jets, Experimental Thermal and Fluid Science, 35 (6) (2011) 1097-1106.

[45] M. Hashish, A modeling study of metal-cutting with abrasive waterjets, Journal of Engineering Materials and Technology-Transactions of the ASME, 106 (1) (1984) 88-100.

[46] M. Hashish, Visualization of the abrasive-waterjet cutting process, Experimental Mechanics, 28 (2) (1988) 159-169.

[47] I. Finnie, Erosion of surfaces by solid particles, Wear, 3 (1960) 87-103.

[48] J.G.A. Bitter, A study of erosion phenomena part I, Wear, 6 (1963) 5-21.

[49] J.Y. Zeng, T.J. Kim, An erosion model of polycrystalline ceramics in abrasive waterjet cutting, Wear, 193 (2) (1996) 207-217.

[50] F.L. Chen, E. Siores, The effect of cutting jet variation on surface striation formation in abrasive water jet cutting, Journal of Materials Processing Technology, 135 (1) (2003) 1-5.

[51] J. Wang, Techniques for enhancing the cutting performance of abrasive waterjets, Key Engineering Materials, 257-258 (2004) 521-526.

[52] L. Chen, E. Siores, W.C.K. Wong, Optimising abrasive waterjet cutting of ceramic materials, Journal of Materials Processing Technology, 74 (1-3) (1998) 251-254.

[53] M. Hashish, A model for abrasive-waterjet (AWJ) machining, Journal of Engineering Materials and Technology-Transactions of the ASME, 111 (2) (1989) 154-162.

[54] J.Y. Zeng, T.J. Kim, Development of an abrasive waterjet kerf cutting model for brittle materials, Fluid Mechanics and Its Applications, 13 (1992) 483-501.

[55] A.A. El-Domiaty, A.A. Abdel-Rahman, Fracture mechanics-based model of abrasive waterjet cutting for brittle materials, International Journal of Advanced Manufacturing Technology, 13 (3) (1997) 172-181.

[56] L. Chen, E. Siores, W.C.K. Wong, Kerf characteristics in abrasive waterjet cutting of ceramic materials, International Journal of Machine Tools and Manufacture, 36 (11) (1996) 1201-1206.

[57] J. Wang, D.M. Guo, A predictive depth of penetration model for abrasive waterjet cutting of polymer matrix composites, Journal of Materials Processing Technology, 121 (2-3) (2002) 390-394.

[58] J. Wang, Predictive depth of jet penetration models for abrasive waterjet cutting of alumina ceramics, International Journal of Mechanical Sciences, 49 (3) (2007) 306-316.

[59] D.K. Shanmugam, T. Nguyen, J. Wang, A study of delamination on graphite/epoxy composites in abrasive waterjet machining, Composites Part A: Applied Science and Manufacturing, 39 (6) (2008) 923-929.

[60] D.K. Shanmugam, S.H. Masood, An investigation on kerf characteristics in abrasive waterjet cutting of layered composites, Journal of Materials Processing Technology, 209 (8) (2009) 3887-3893.

[61] J. Wang, A new model for predicting the depth of cut in abrasive waterjet contouring of alumina ceramics, Journal of Materials Processing Technology, 209 (5) (2009) 2314-2320.

[62] S. Paul, A.M. Hoogstrate, C.A. van Luttervelt, H.J.J. Kals, Analytical and experimental modelling of the abrasive water jet cutting of ductile materials, Journal of Materials Processing Technology, 73 (1-3) (1998) 189-199.

[63] A.G. Evans, M.E. Gulden, M. Rosenblatt, Impact damage in brittle materials in elastic-plastic response regime, Proceedings of the Royal Society A, 361 (1706) (1978) 343-365.

[64] S.M. Wiederhorn, B.R. Lawn, Erosion of brittle materials by solid particle impact, Journal of the American Ceramic Society, 62 (1979) 66-70.

[65] F.R. Giordano, M.D. Weir, W.P. Fox, A First Course in Mathematical Modeling, Brooks/Cole Publishing Company, Pacific Grove, California, United States, 2003.

[66] M. Ramulu, D. Arola, The influence of abrasive waterjet cutting conditions on the surface quality of graphite-epoxy laminates, International Journal of Machine Tools and Manufacture, 34 (3) (1994) 295-313.

[67] J. Wang, A machinability study of polymer matrix composites using abrasive waterjet cutting technology, Journal of Materials Processing Technology, 94 (1) (1999) 30-35.

[68] J. Wang, W.C.K. Wong, A study of abrasive waterjet cutting of metallic coated sheet steels, International Journal of Machine Tools and Manufacture, 39 (6) (1999) 855-870.

[69] J. Wang, H. Liu, Profile cutting on alumina ceramics by abrasive waterjet. II: cutting performance models, Proceedings of the Institution of Mechanical Engineers Part C: Journal of Mechanical Engineering Science, 220 (5) (2006) 715-725.

[70] T. Nguyen, K.L. Pang, J. Wang, A preliminary study of the erosion process in micro-machining of glasses with a low pressure slurry jet, Key Engineering Materials, 389-390 (2009) 375-380.

[71] H. Nouraei, K. Kowsari, J.K. Spelt, M. Papini, Surface evolution models for abrasive slurry jet micro-machining of channels and holes in glass, Wear, 309 (1-2) (2014) 65-73.

[72] T. Nguyen, D.K. Shanmugam, J. Wang, Effect of liquid properties on the stability of an abrasive waterjet, International Journal of Machine Tools and Manufacture, 48 (10) (2008) 1138-1147.

[73] K.L. Pang, T. Nguyen, J.M. Fan, J. Wang, Machining of micro-channels on brittle glass using an abrasive slurry jet, Key Engineering Materials, 443 (2010) 639-644.

[74] K.L. Pang, T. Nguyen, J.M. Fan, J. Wang, A study of micro-channeling on glasses using an abrasive slurry jet, Machining Science and Technology, 16 (4) (2012) 547-563.

[75] K. Kowsari, H. Nouraei, D.F. James, J.K. Spelt, M. Papini, Abrasive slurry jet micro-machining of holes in brittle and ductile materials, Journal of Materials Processing Technology, 214 (9) (2014) 1909-1920.

[76] K. Kowsari, D.F. James, M. Papini, J.K. Spelt, The effects of dilute polymer solution elasticity and viscosity on abrasive slurry jet micro-machining of glass, Wear, 309 (1-2) (2014) 112-119.

[77] A. Ghobeity, H. Getu, M. Papini, J.K. Spelt, Surface evolution models for abrasive jet micromachining of holes in glass and polymethylmethacrylate (PMMA), Journal of Micromechanics and Microengineering, 17 (11) (2007) 2175-2185.

[78] A. Ghobeity, T. Krajac, I. Burzynski, M. Papini, J.K. Spelt, Surface evolution models in abrasive jet micromachining, Wear, 264 (3-4) (2008) 185-198.

[79] K.H. Zum Gahr, Wear by hard particles, Tribology International, 31 (10) (1998) 587-596.

[80] I. Finnie, D.H. Mcfadden, Velocity dependence of erosion of ductile metals by solid particles at low angles of incidence, Wear, 48 (1) (1978) 181-190.

[81] I. Finnie, Some reflections on the past and future of erosion, Wear, 186 (1) (1995) 1-10.

[82] J.G.A. Bitter, A study of erosion phenomena part II, Wear, 6 (1963) 169-190.

[83] B.R. Lawn, M.V. Swain, Microfracture beneath point indentations in brittle solids, Journal of Materials Science, 10 (1) (1975) 113-122.

[84] H. Wensink, M.C. Elwenspoek, A closer look at the ductile-brittle transition in solid particle erosion, Wear, 253 (9-10) (2002) 1035-1043.

[85] G.L. Sheldon, I. Finnie, Mechanism of material removal in erosive cutting of brittle materials, Journal of Engineering for Industry, 88 (4) (1966) 393-400.

[86] J.E. Ritter, P. Strzepa, K. Jakus, L. Rosenfeld, K.J. Buckman, Erosion damage in glass and alumina, Journal of the American Ceramic Society, 67 (11) (1984) 769-774.

[87] J.E. Ritter, Erosion damage in structural ceramics, Materials Science and Engineering, 71 (1-2) (1985) 195-201.

[88] J.L. Routbort, R.O. Scattergood, E.W. Kay, Erosion of silicon single crystals, Journal of the American Ceramic Society, 63 (11-1) (1980) 635-640.

[89] M. Wakuda, Y. Yamauchi, S. Kanzaki, Material response to particle impact during abrasive jet machining of alumina ceramics, Journal of Materials Processing Technology, 132 (1-3) (2003) 177-183.

[90] Q.L. Li, J. Wang, C.Z. Huang, Erosion mechanisms of monocrystalline silicon under a microparticle laden air jet, Journal of Applied Physics, 104 (3) (2008) 034903.

[91] A.K. Basak, J.M. Fan, J. Wang, P. Mathew, Material removal mechanisms of monocrystalline silicon under the impact of high velocity micro-particles, Wear, 269 (3-4) (2010) 269-277.

[92] F.W. Flocker, L.R. Dharani, Modelling fracture in laminated architectural glass subject to low velocity impact, Journal of Materials Science, 32 (10) (1997) 2587-2594.

[93] R.A. Behr, P.A. Kremer, L.R. Dharani, F.S. Ji, N.D. Kaiser, Dynamic strains in architectural laminated glass subjected to low velocity impacts from small projectiles, Journal of Materials Science, 34 (23) (1999) 5749-5756.

[94] X. Sun, M.A. Khaleel, Modeling of glass fracture damage using continuum damage mechanics-static spherical indentation, International Journal of Damage Mechanics, 13 (3) (2004) 263-285.

[95] X. Sun, M.A. Khaleel, R.W. Davies, Modeling of stone-impact resistance of monolithic glass ply using continuum damage mechanics, International Journal of Damage Mechanics, 14 (2) (2005) 165-178.

[96] J. Ismail, F. Zairi, M. Nait-Abdelaziz, Z. Azari, Computational modelling of static indentation-induced damage in glass, Computational Materials Science, 42 (3) (2008) 407-415.

[97] J. Ismail, F. Zairi, M. Nait-Abdelaziz, S. Bouzid, Z. Azari, Experimental and numerical investigations on erosion damage in glass by impact of small-sized particles, Wear, 271 (5-6) (2011) 817-826.

[98] S. Anwar, D.A. Axinte, A.A. Becker, Finite element modelling of overlapping abrasive waterjet milled footprints, Wear, 303 (1-2) (2013) 426-436.

[99] S. Anwar, D.A. Axinte, A.A. Becker, Finite element modelling of abrasive waterjet milled footprints, Journal of Materials Processing Technology, 213 (2) (2013) 180-193.

[100] P.A. Cundall, O.D.L. Strack, A discrete numerical-model for granular assemblies-reply, Geotechnique, 30 (3) (1980) 335-336.

[101] D.O. Potyondy, P.A. Cundall, A bonded-particle model for rock, International Journal of Rock Mechanics and Mining Sciences, 41 (8) (2004) 1329-1364.

[102] H.Y. Huang, Discrete Element Modeling of Tool-rock Interaction, Ph.D. Thesis, University of Minnesota, Minneapolis, United States, 1999.

[103] S.T. Lei, B.D. Yang, Distinct element simulation of ceramic machining: Material removal mechanism, Transactions of the North American Manufacturing Research Institution of SME, 33 (2005) 485-492.

[104] X. Shen, S. Lei, Distinct element simulation of laser assisted machining of silicon nitride ceramics: suface/subsurface cracks and damage, in ASME 2005 International Mechanical Engineering Congress and Exposition, Orlando, Florida, United States, 2005, pp. 1267-1274.

[105] X.W. Shen, B.D. Yang, S.T. Lei, Microstructural modeling and dynamic process simulation of laser-assisted machining of silicon nitride ceramics with distinct element method, Journal of Manufacturing Science and Engineering-Transactions of the ASME, 134 (2) (2012) 021011.

[106] Y.Q. Tan, S.Q. Jiang, C. Li, D.M. Yang, G.F. Zhang, Y. Sheng, Study on mechanical properties and size effect of Si_3N_4 using discrete element method, Advanced Materials Research, 76-78 (2009) 719-724.

[107] Y.Q. Tan, D.M. Yang, Y. Sheng, Discrete element method (DEM) modeling of fracture and damage in the machining process of polycrystalline SiC, Journal of the European Ceramic Society, 29 (6) (2009) 1029-1037.

[108] H. Toshiyoshi, H. Fujita, T. Ueda, A piezoelectrically operated optical chopper by quartz micromachining, Journal of Microelectromechanical Systems, 4 (1) (1995) 3-9.

[109] P. Kao, S. Doerner, T. Schneider, D. Allara, P. Hauptmann, S. Tadigadapa, A micromachined quartz resonator array for biosensing applications, Journal of Microelectromechanical Systems, 18 (3) (2009) 522-530.

[110] M.J. McCarthy, N.A. Molloy, Review of stability of liquid jets and the influence of nozzle design, The Chemical Engineering Journal, 7 (1) (1974) 1-20.

[111] J. Wang, The effects of the jet impact angle on the cutting performance in AWJ machining of alumina ceramics, Key Engineering Materials, 238-239 (2003) 117-124.

[112] B.R. Lawn, A.G. Evans, D.B. Marshall, Elastic-plastic indentation damage in ceramics-the median-radial crack system, Journal of the American Ceramic Society, 63 (9-10) (1980) 574-581.

[113] D.B. Marshall, S.S. Chiang, A.G. Evans, B.R. Lawn, Elastic-plastic indentation damage in ceramics-the lateral crack system, Journal of the American Ceramic Society, 60 (3) (1981) 384-384.

[114] M.S. Bingley, T. Deng, M.S.A. Bradley, S.R. De Silva, A comparison of the gas-blast and centrifugal-accelerator erosion testers: the influence of particle dynamics, Wear, 265 (7-8) (2008) 945-955.

[115] M. Achtsnick, High Performance Micro Abrasive Blasting, Ph.D. Thesis, Delft University of Technology, Delft, The Netherlands, 2005.

[116] H. Wadell, Volume, shape, and roundness of rock particles, The Journal of Geology, 40 (5) (1932) 443-451.

[117] I.M. Hutchings, Tribology: Friction and Wear of Engineering Materials, Edward Arnold, London, UK, 1992.

[118] A.J. Sparks, I.M. Hutchings, Transitions in the erosive wear behavior of a glass ceramic, Wear, 149 (1-2) (1991) 99-110.

[119] S.V. Margolis, D.H. Krinsley, Processes of formation and environmental occurrence of microfeatures on detrital quartz grains, American Journal of Science, 274 (5) (1974) 449-464.

[120] J.M. Fan, C.Y. Wang, J. Wang, Modelling the erosion rate in micro abrasive air jet machining of glasses, Wear, 266 (9-10) (2009) 968-974.

[121] J. Wang, Depth of cut models for multipass abrasive waterjet cutting of alumina ceramics with nozzle oscillation, Frontiers of Mechanical Engineering in China, 5 (1) (2009) 19-32.

[122] I.M. Hutchings, R.E. Winter, Particle erosion of ductile metals: a mechanism of material removal, Wear, 27 (1974) 121-128.

[123] I.M. Hutchings, D.W.T. Deuchar, A.H. Muhr, Erosion of unfilled elastomers by solid particle impact, Journal of Materials Science, 22 (11) (1987) 4071-4076.

[124] I.M. Hutchings, Ductile brittle transitions and wear maps for the erosion and abrasion of brittle materials, Journal of Physics D: Applied Physics, 25 (1A) (1992) A212-A221.

[125] G.L. Sheldon, A. Kanhere, Investigation of impingement erosion using single particles, Wear, 21 (1) (1972) 195-209.

[126] J.Y. Zeng, T.J. Kim, An erosion model for abrasive waterjet milling of polycrystalline ceramics, Wear, 199 (2) (1996) 275-282.

[127] S.M. Wiederhorn, B.J. Hockey, Effect of material parameters on the erosion resistance of brittle materials, Journal of Materials Science, 18 (3) (1983) 766-780.

[128] I.M. Hutchings, Mechanisms of wear in powder technology-a review, Powder Technology, 76 (1) (1993) 3-13.

[129] H.M. Clark, L.C. Burmeister, The influence of the squeeze film on particle impact velocities in erosion, International Journal of Impact Engineering, 12 (3) (1992) 415-426.

[130] H.M. Clark, A comparison of particle impact in gas-solid and liquid-solid erosion, Wear, 186 (2) (1995) 465-472.

[131] H.M. Clark, K.K. Wong, Impact angle, particle energy and mass-loss in erosion by dilute slurries, Wear, 186 (2) (1995) 454-464.

[132] H.M. Clark, The influence of the squeeze film in slurry erosion, Wear, 256 (9-10) (2004) 918-926.

[133] Particle flow code in 3-Dimensions (PFC3D) manual, Itasca Consulting Group Inc., Minneapolis, Minnesota, United States, 2004.

[134] B.D. Yang, Y. Jiao, S.T. Lei, A study on the effects of microparameters on macroproperties for specimens created by bonded particles, Engineering Computations, 23 (6) (2006) 607-631.

[135] H. Qi, J.M. Fan, J. Wang, Impact erosion of quartz crystals by micro-particles in abrasive waterjet micro-machining, Advanced Materials Research, 797 (2013) 46-51.

[136] A.G. Evans, S.M. Wiederhorn, Crack-propagation and failure prediction in silicon-nitride at elevated-temperatures, Journal of Materials Science, 9 (2) (1974) 270-278.

[137] M.G. Mendiratta, J. Wimmer, I. Bransky, Dynamic K_{Ic} and dynamic flexural strength in HS-130 Si_3N_4, Journal of Materials Science, 12 (1) (1977) 212-214.

[138] M.A. Meyers, K.K. Chawla, Mechanical Behavior of Materials, Cambridge University Press, New York, United States, 2009.

[139] A.F. Bower, Applied Mechanics of Solids, Taylor and Francis Group, Boca Raton, Florida, United States, 2010.

[140] H.J. Gao, T.Y. Zhang, P. Tong, Local and global energy release rates for an electrically yielded crack in a piezoelectric ceramic, Journal of the Mechanics and Physics of Solids, 45 (4) (1997) 491-510.

[141] A.G. Atkins, Y.W. Mai, Residual strain-energy in elastoplastic adhesive and cohesive fracture, International Journal of Fracture, 30 (3) (1986) 203-221.

[142] D.W. Celotta, U.A. Qureshi, E.V. Stepanov, D.P. Goulet, J. Hunter, C.H. Buckberry, R. Hil, S.V. Sherikar, M. Moshrefi-Torbati, R.J.K. Wood, Sand erosion testing of novel compositions of hard ceramics, Wear, 263 (2007) 278-283.

[143] Y.F. Wang, Z.G. Yang, Finite element model of erosive wear on ductile and brittle materials, Wear, 265 (5-6) (2008) 871-878.

[144] M. Takaffoli, M. Papini, Numerical simulation of solid particle impacts on Al6061-T6 part II: materials removal mechanisms for impact of multiple angular particles, Wear, 296 (1-2) (2012) 648-655.

[145] A. Momber, Blast Cleaning Technology, Springer-Verlag Berlin, Heidlberg, 2008.

Appendix A

Data for abrasive slurry jet micro-channelling tests

Table A-1. Experimental data for model development.

NO.	d_p	C_p	P	α_j	u	h	w_t	θ	MRR	R_a
	μm	% by mass	MPa	deg	mm/s	μm	μm	deg	$\times10^{-3}$mm^3/s	μm
1	18	15	8	90	0.1	38.46	370.18	57.39	1.21	1.33
2	18	15	8	90	0.2	19.06	344.12	72.62	0.99	0.48
3	18	15	8	90	0.3	8.52	341.03	83.89	0.69	0.70
4	18	15	8	90	0.4	7.76	306.30	84.34	0.67	0.58
5	18	20	12	75	0.1	64.16	378.56	65.31	1.64	1.50
6	18	20	12	75	0.2	40.95	368.41	68.66	2.06	1.00
7	18	20	12	75	0.3	15.28	345.60	83.12	0.94	0.95
8	18	20	12	75	0.4	11.09	324.80	85.08	0.85	0.93
9	18	25	16	60	0.1	277.16	448.83	29.00	8.11	3.75
10	18	25	16	60	0.2	129.58	412.71	57.20	5.47	1.75
11	18	25	16	60	0.3	61.52	411.94	61.10	5.65	1.05
12	18	25	16	60	0.4	37.30	405.53	66.00	4.78	1.00
13	18	30	20	45	0.1	143.84	413.72	48.20	3.76	1.80
14	18	30	20	45	0.2	81.80	392.21	64.98	3.65	1.18
15	18	30	20	45	0.3	48.89	367.20	69.88	3.52	0.90
16	18	30	20	45	0.4	28.79	345.76	75.78	2.65	0.93
17	15	15	16	45	0.1	86.22	434.98	62.10	2.38	1.08
18	15	15	16	45	0.2	50.68	396.88	72.14	2.19	0.68

19	15	15	16	45	0.3	24.72	364.80	79.07	1.73	0.68
20	15	15	16	45	0.4	14.69	329.60	82.49	1.25	0.60
21	15	20	20	60	0.1	244.76	427.00	33.50	6.55	3.25
22	15	20	20	60	0.2	116.84	413.27	50.86	6.40	2.33
23	15	20	20	60	0.3	76.56	398.82	60.42	6.19	1.38
24	15	20	20	60	0.4	49.20	387.17	63.00	5.86	0.80
25	15	25	8	75	0.1	111.72	416.88	54.20	3.00	1.98
26	15	25	8	75	0.2	62.96	407.48	69.09	2.99	1.73
27	15	25	8	75	0.3	40.33	379.64	72.05	3.01	0.83
28	15	25	8	75	0.4	30.47	358.38	77.04	2.78	0.58
29	15	30	12	90	0.1	121.83	414.85	48.18	3.33	3.73
30	15	30	12	90	0.2	46.76	407.81	68.26	2.83	1.63
31	15	30	12	90	0.3	21.20	397.88	77.69	1.89	0.75
32	15	30	12	90	0.4	14.80	359.98	78.99	1.60	0.83
33	12	15	12	60	0.1	41.02	413.48	70.10	1.22	0.88
34	12	15	12	60	0.2	16.44	386.03	80.40	0.98	0.78
35	12	15	12	60	0.3	9.91	358.08	86.75	0.55	0.53
36	12	15	12	60	0.4	7.27	317.02	87.13	0.54	0.43
37	12	20	8	45	0.1	11.35	436.07	83.98	0.37	0.40
38	12	20	8	45	0.2	6.86	419.00	87.46	0.36	0.35
39	12	20	8	45	0.3	4.73	379.60	87.97	0.37	0.28
40	12	20	8	45	0.4	3.13	367.18	88.20	0.35	0.23
41	12	25	20	90	0.1	169.83	463.10	43.89	5.09	3.33
42	12	25	20	90	0.2	88.03	428.57	58.89	4.84	1.05
43	12	25	20	90	0.3	61.66	397.86	66.49	4.73	0.88
44	12	25	20	90	0.4	36.56	377.46	70.19	4.10	0.93
45	12	30	16	75	0.1	165.93	429.57	44.54	4.44	3.30
46	12	30	16	75	0.2	113.46	415.48	64.08	4.26	1.63
47	12	30	16	75	0.3	50.63	403.46	71.30	3.85	0.80
48	12	30	16	75	0.4	31.51	385.85	74.01	3.41	0.68
49	10	15	20	75	0.1	64.23	469.73	58.82	2.42	1.73
50	10	15	20	75	0.2	40.80	427.48	76.11	2.14	1.35
51	10	15	20	75	0.3	13.21	420.21	85.88	1.10	0.75
52	10	15	20	75	0.4	8.37	406.45	85.86	0.97	0.70

53	10	20	16	90	0.1	50.48	428.53	71.32	1.41	0.83
54	10	20	16	90	0.2	24.50	410.32	80.41	1.29	0.80
55	10	20	16	90	0.3	19.44	394.71	82.47	1.43	0.58
56	10	20	16	90	0.4	12.17	379.09	84.33	1.21	0.40
57	10	25	12	45	0.1	10.62	424.79	86.53	0.26	0.33
58	10	25	12	45	0.2	6.83	409.32	87.59	0.33	0.33
59	10	25	12	45	0.3	4.90	400.52	88.31	0.34	0.33
60	10	25	12	45	0.4	3.55	377.75	88.40	0.37	0.23
61	10	30	8	60	0.1	7.86	419.12	86.41	0.24	0.45
62	10	30	8	60	0.2	4.18	402.79	87.93	0.24	0.40
63	10	30	8	60	0.3	3.14	386.96	88.33	0.27	0.40
64	10	30	8	60	0.4	2.32	378.53	88.81	0.26	0.40
65	18	15	16	90	0.2	120.31	382.35	57.10	4.85	1.98
66	18	15	16	75	0.2	96.53	385.29	58.60	4.29	1.48
67	18	15	16	60	0.2	83.55	384.05	62.30	3.52	1.40
68	18	15	16	45	0.2	55.90	388.05	63.70	3.04	1.20
69	18	15	12	90	0.2	45.04	363.10	64.10	2.48	0.60
70	18	15	20	90	0.2	171.41	409.40	50.10	8.28	4.00
71	18	20	16	60	0.2	102.78	396.41	59.40	4.45	1.60
72	18	30	16	60	0.2	150.38	413.44	54.10	6.07	2.13
73	15	15	16	90	0.2	92.44	390.82	64.50	3.69	1.68
74	15	15	16	75	0.2	73.16	392.48	67.10	3.08	1.68
75	15	15	16	60	0.2	62.13	389.42	67.60	2.59	1.28
76	15	15	20	45	0.2	71.93	416.45	68.10	2.85	1.98
77	15	15	8	45	0.2	12.80	380.95	84.00	0.74	0.28
78	15	15	12	45	0.2	16.86	386.82	76.90	0.97	0.38
79	12	15	16	90	0.2	82.45	398.27	71.10	2.59	1.38
80	12	15	16	75	0.2	61.75	397.95	72.00	2.53	1.08
81	12	15	16	60	0.2	50.62	401.35	74.80	2.16	0.88
82	12	15	16	45	0.2	37.91	414.49	78.90	1.80	0.68
83	12	15	8	60	0.2	12.58	384.52	86.70	0.38	0.18
84	12	15	20	60	0.2	99.65	410.78	71.20	2.57	2.20
85	12	20	16	75	0.2	81.85	407.51	71.00	2.81	1.10
86	12	25	16	75	0.2	109.29	414.99	66.10	3.67	1.33

87	10	15	16	90	0.2	34.86	411.22	77.25	1.71	0.35
88	10	15	16	75	0.2	24.41	417.42	78.13	1.43	0.28
89	10	15	16	60	0.2	16.91	429.30	82.25	1.01	0.20
90	10	15	16	45	0.2	10.40	445.17	86.75	0.50	0.20
91	10	15	8	75	0.2	2.80	407.23	88.00	0.16	0.13
92	10	15	12	75	0.2	8.10	415.38	86.00	0.46	0.20

Table A-2. Experimental data for model verification.

NO.	d_p	C_p	P	α_j	u	h	w_t	θ	MRR
	μm	% by mass	MPa	deg	mm/s	μm	μm	degree	$\times 10^{-3}mm^3/s$
1	15	20	8	90	0.1	59.24	408.23	66.63	1.33
2	15	20	8	90	0.2	18.67	401.58	76.25	0.72
3	15	20	12	90	0.1	124.98	421.08	53.00	3.12
4	15	20	12	90	0.2	69.08	408.58	64.25	2.05
5	15	20	16	90	0.1	192.91	452.03	53.50	5.66
6	15	20	16	90	0.2	101.44	413.29	57.13	4.66
7	15	20	16	90	0.3	67.25	392.87	64.63	4.33
8	15	20	16	90	0.4	46.94	379.15	69.75	4.39
9	15	20	20	90	0.1	316.05	429.97	44.13	8.30
10	15	20	20	90	0.2	197.76	422.16	49.63	7.20
11	15	20	20	90	0.3	113.93	400.89	55.75	6.93
12	15	20	20	90	0.4	52.86	395.80	66.63	5.05
13	15	20	16	75	0.1	181.81	434.23	51.00	4.32
14	15	20	16	75	0.2	90.71	418.70	58.88	3.86
15	15	20	16	60	0.1	140.67	430.91	53.13	3.37
16	15	20	16	60	0.2	75.63	424.65	63.00	3.33
17	15	15	16	75	0.1	148.58	406.35	57.50	3.47
18	15	15	16	75	0.2	74.78	384.42	62.50	3.10
19	15	25	16	75	0.1	217.96	419.58	46.63	5.32
20	15	25	16	75	0.2	140.00	405.84	56.50	4.49
21	15	30	16	75	0.1	233.26	434.52	43.13	5.93
22	15	30	16	75	0.2	146.13	414.51	54.25	5.00
23	10	20	16	90	0.1	69.19	427.78	65.88	1.63

24	10	20	16	90	0.2	29.30	415.51	77.75	1.35
25	12	20	16	90	0.1	140.36	422.26	55.63	3.39
26	12	20	16	90	0.2	50.53	407.72	64.38	3.26
27	18	20	16	90	0.1	282.93	417.00	41.38	8.01
28	18	20	16	90	0.2	138.00	402.69	54.25	7.01
29	15	20	16	45	0.1	84.73	423.32	59.38	2.18
30	15	20	16	45	0.2	56.16	413.00	66.00	2.34

Appendix B

Data for single particle impact tests

NO.	d_p	v_p	α_p	Average crater volume
	μm	m/s	deg	μm^3
1	27	164	90	410.93
2	27	150	90	282.06
3	27	130	90	176.79
4	27	100	90	116.67
5	27	164	70	317.98
6	27	150	70	223.72
7	27	130	70	151.78
8	27	100	70	102.54
9	27	164	50	183.02
10	27	150	50	120.50
11	27	130	50	88.97
12	27	100	50	71.03
13	27	164	30	161.10
14	27	150	30	109.63
15	27	130	30	64.70
16	27	100	30	55.16

Appendix C

Data for abrasive jet micro-channel machining tests

NO.	d_p	m_a	P_a	α_j	u	h	w_t	Material erosion rate
	μm	mg/s	MPa	deg	mm/s	μm	μm	10^{-2} g/g
1	27	5	0.66	90	15	18.83	281.50	20.29
2	27	5	0.66	90	20	15.35	262.83	21.26
3	27	5	0.66	90	25	8.75	269.48	20.13
4	27	5	0.66	60	15	16.98	277.03	18.43
5	27	5	0.66	60	20	12.15	248.00	18.22
6	27	5	0.66	60	25	8.33	246.38	18.98
7	27	5	0.66	30	15	6.98	303.50	9.99
8	27	5	0.66	30	20	6.35	279.00	11.09
9	27	5	0.66	30	25	3.95	272.30	10.99

Appendix D

List of publications

[1] H. Qi, J.M. Fan, J. Wang, An experimental study of the abrasive water jet micro-machining process for quartz crystals, Advanced Materials Research, 565 (2012) 339-344.

[2] H. Qi, J.M. Fan, J. Wang, Impact erosion of quartz crystals by micro-particles in abrasive waterjet micro-machining, Advanced Materials Research, 797 (2013) 46-51.

[3] H. Qi, J.M. Fan, J. Wang, A study of the micro-machining process on quartz crystals using an abrasive slurry jet, Proceedings of the Institution of Mechanical Engineers, Part B: Journal of Engineering Manufacture, DOI: 10.1177/0954405414528167.

[4] H. Qi, J.M. Fan, J. Wang, H.Z. Li, Impact erosion by high velocity micro-particles on a quartz crystal, Tribology International, DOI: 10.1016/j.triboint.2014.10.016.